Simulation of plasmonic nanoparticles situated on substrates

Doctoral Thesis

to be awarded the degree of
Doctor rerum naturalium (Dr. rer. nat.)
at the University of Graz

submitted by

Jürgen Alexander Waxenegger

at the Intstitute of Physics

Supervisor: Ao. Univ. Prof. Mag. Dr.rer.nat. Ulrich Hohenester

2016

Kurzzusammenfassung / Abstract

Simulation plasmonischer Nanopartikel auf Substraten

Die Plasmonik untersucht die Wechselwirkung zwischen elektromagnetischen Feldern und den freien Elektronen eines Metalls. Die plasmonischen Anregungen von metallischen Nanopartikeln werden Partikelplasmonen genannt. Eine Simulationsmethode welche gut geeignet ist, um die optischen Eigenschaften von plasmonischen Nanoteilchen zu beschreiben, ist die Randelementmethode. Bei der Randelementmethode werden linerare partielle Differentialgleichungen in Integralgleichungen umgeschrieben und dann mit Hilfe von Green-Funktionen gelöst. In dieser Arbeit zeigen wir, wie Substrateffekte in der Randelementmethode berücksichtigt werden können. Auf diese Weise ist es möglich, metallische Nanopartikel, welche sich auf Substraten befinden zu simulieren. Eine wichtige Rolle spielen dabei die sogenannten reflektierten Green-Funktionen, welche die Wechselwirkung mit dem Substrat beschreiben. Wir untersuchen unterschiedliche Substrate und Partikelgeometrien, machen Konvergenzuntersuchungen und vergleichen die Ergebnisse mit Ergebnissen, welche mit der Discrete Dipole Approximation Methode erhalten werden.

Simulation of plasmonic nanoparticles situated on substrates

Plasmonics studies the interaction between electromagnetic fields and the free electrons in a metal. The plasmonic excitations of metallic nanoparticles are called localized surface plasmon resonances. A simulation method well suited for studying the optical properties of plasmonic nanoparticles is the boundary element method. In the boundary element method linear partial differential equations which have been formulated as integral equations are solved with the use of Green functions. In this thesis we show how to include substrate effects in the boundary element method. In this way, the simulation of metallic nanoparticles situated on substrates becomes feasible. An important part play the so-called reflected Green functions which describe the substrate interaction. We study different substrates and particle geometries, study the convergence of the simulations, and compare the results to results obtained with the discrete dipole approximation method.

Contents

To my parents and my brother

1. Introduction and Structure of Thesis

1.1. Introduction

Plasmonics studies the interaction between electromagnetic fields and the free electrons in a metal [2,4,57,68–70,78,86]. The plasmonic excitations of metallic nanoparticles are called localized surface plasmon resonances. A simulation method well suited for studying the optical properties of plasmonic nanoparticles is the boundary element method [25, 26, 33, 35, 86, 95]. In this thesis we show how the boundary element method can be modified to allow simulations of plasmonic nanoparticles situated on substrates or in layer structures [93].

1.2. Structure of Thesis

This thesis is divided into four parts. The first part gives an introduction to plasmonics. We start with the derivation of surface plasmon polaritons. Then we discuss localized surface plasmon resonances on metallic nanoparticles. In the end of part one we study the effect of a substrate on the plasmon resonances using a simple image charge model.

The second part describes simulation methods for plasmonic nanoparticles in free space. We start with the boundary element method for the solution of the full Maxwell's equations. Then we discuss the boundary element method in the quasistatic limit. In the end of part two another method, the discrete dipole approximation, is presented.

The third part describes the modification of these methods to allow the description of metallic nanoparticles situated on substrates. We start with the extension of the

boundary element method. In this main part of the thesis the calculation of the reflected Green functions plays an important role. In the end of part three a modification of the discrete dipole approximation, done by Loke et al [52], is presented.

The last part describes some elements of the implementation in the MNPBEM Toolbox and we show simulation results which compare the boundary element method to the discrete dipole approximation method, and present optical cross sections and field enhancements for different particle geometries and substrates.

2. Plasmonics

The two main ingridients of plasmonics [57, 60, 69, 72, 83, 86] are surface plasmon polaritons and localized surface plasmon resonances.

Mathematically surface plasmon polaritons where already described in the beginning of the last century [56, 84, 101]. The intensity drop at optical metallic diffraction gratings [94] and the loss phenomena at thin metallic foils was later interpretated as resulting from these surface waves [19, 48, 78, 79].

The mathematical description of localized surface plasmon resonances was also established around the beginning of the last century [18, 63, 104].

2.1. Surface plasmons

In this section, mainly based on [57], SI units are used. Surface plasmons are solutions of the Maxwell's equations which describe a propagating wave at the interface between a dielectric and a metal. The fields away from the surface are decaying evanescently. To describe this surface waves we first look for the wave equation which can be obtained from the Maxwell's equations.

In an isotropic and linear medium the macroscopic Maxwell's equations have the following form [40] [92]:

$$\nabla \times \mathbf{E}(\mathbf{r}, t) = -\frac{\partial \mathbf{B}(\mathbf{r}, t)}{\partial t}, \tag{2.1}$$

$$\nabla \times \mathbf{H}(\mathbf{r},t) = \frac{\partial \mathbf{D}(\mathbf{r},t)}{\partial t} + \mathbf{j}(\mathbf{r},t), \tag{2.2}$$

$$\nabla \cdot \mathbf{D}(\mathbf{r},t) = \rho(\mathbf{r},t), \tag{2.3}$$

$$\nabla \cdot \mathbf{B}(\mathbf{r},t) = 0. \tag{2.4}$$

Here $\mathbf{E}(\mathbf{r},t)$ is the electric field, $\mathbf{H}(\mathbf{r},t)$ the magnetic field, $\mathbf{D}(\mathbf{r},t) = \epsilon_0\epsilon\mathbf{E}(\mathbf{r},t)$ the electric displacement, $\mathbf{B}(\mathbf{r},t) = \mu_0\mu\mathbf{H}(\mathbf{r},t)$ the magnetic induction, $\mathbf{j}(\mathbf{r},t)$ the current density, $\rho(r,t)$ the charge density, ϵ is the dielectric constant or relative permittivity, μ the relative permeability, ϵ_0 is the electric permittivity and μ_0 the magnetic permeability of the vacuum.

If no external sources

$$\nabla \cdot \mathbf{D}(\mathbf{r},t) = 0 \tag{2.5}$$

and currents

$$\mathbf{j}(\mathbf{r},t) = 0 \tag{2.6}$$

are present, the curl equations (2.1, 2.2) can be combined

$$\nabla \times \nabla \times \mathbf{E} = -\mu_0 \frac{\partial^2 \mathbf{D}}{\partial t^2}, \tag{2.7}$$

which for a negligible variation of the dielectric function and using

$$\nabla \times \nabla \times \mathbf{E} = \nabla(\nabla \cdot \mathbf{E}) - \nabla^2 \mathbf{E} \tag{2.8}$$

and

$$\nabla \cdot (\epsilon \mathbf{E}) = \mathbf{E}\nabla\epsilon + \epsilon\nabla \cdot \mathbf{E} \tag{2.9}$$

reduces to the wave equation

$$\nabla^2 \mathbf{E} - \frac{\epsilon}{c^2}\frac{\partial^2 \mathbf{E}}{\partial t^2} = 0. \tag{2.10}$$

Asuming a harmonic time dependence

$$\mathbf{E}(\mathbf{r},t) = \mathbf{E}(\mathbf{r})e^{-i\omega t}, \tag{2.11}$$

we find the

Helmholtz equation [57]

$$\nabla^2\mathbf{E} + k_0^2\epsilon\mathbf{E} = 0. \tag{2.12}$$

Here $k_0 = \frac{\omega}{c}$ is the wave number of the propagating wave in vacuum.

For a one-dimensional problem [57] [92]

$$\mathbf{E}(x,y,z) = \mathbf{E}(z)e^{i\beta x}, \tag{2.13}$$

with the propagation constant $\beta = k_x$ we get

$$\frac{\partial^2\mathbf{E}(z)}{\partial z^2} + (k_0^2\epsilon - \beta^2)\mathbf{E} = 0. \tag{2.14}$$

For a harmonic time dependence, homogenity in the y-direction and propagation in x-direction, the explicit field components obtained from the curl equations are

$$\frac{\partial E_y}{\partial z} = -i\omega\mu_0 H_x, \tag{2.15}$$

$$\frac{\partial E_x}{\partial z} - i\beta E_z = i\omega\mu_0 H_y, \tag{2.16}$$

$$i\beta E_y = i\omega\mu_0 H_z, \tag{2.17}$$

$$\frac{\partial H_y}{\partial z} = i\omega\epsilon_0\epsilon_0 E_x, \tag{2.18}$$

$$\frac{\partial H_x}{\partial z} - i\beta H_z = -i\omega\epsilon_0\epsilon_0 E_y, \tag{2.19}$$

$$i\beta H_y = -i\omega\epsilon_0\epsilon_0 E_z. \tag{2.20}$$

There are two sets of self-consistent solutions [57]. Transverse magnetic modes

$$E_x = -i\frac{1}{\omega\epsilon_0\epsilon}\frac{\partial H_y}{\partial z}, \tag{2.21}$$

$$E_z = -\frac{\beta}{\omega\epsilon_0\epsilon}H_y, \tag{2.22}$$

$$\frac{\partial^2 H_y}{\partial z^2} + (k_0^2\epsilon - \beta^2)H_y = 0, \tag{2.23}$$

and transverse electric modes

$$H_x = i\frac{1}{\omega\mu_0}\frac{\partial E_y}{\partial z}, \tag{2.24}$$

$$H_z = \frac{\beta}{\omega\mu_0}E_z, \tag{2.25}$$

$$\frac{\partial^2 E_y}{\partial z^2} + (k_0^2\epsilon - \beta)E_y = 0. \tag{2.26}$$

The simplest geometry where surface plasmon polaritons can exist is a single flat interface between a dielectric with ϵ_2 and a metal with $\epsilon_1(\omega)$ [57]. So for $z > 0$

$$H_y(z) = A_2 e^{i\beta x}e^{-k_2 z}, \tag{2.27}$$

$$E_x(z) = iA_2\frac{1}{\omega\epsilon_0\epsilon_2}k_2 e^{i\beta x}e^{-k_2 z}, \tag{2.28}$$

$$E_z(z) = -A_2\frac{\beta}{\omega\epsilon_0\epsilon_2}e^{i\beta x}e^{-k_2 z}, \tag{2.29}$$

and

$$H_y(z) = A_1 e^{i\beta x}e^{k_1 z}, \tag{2.30}$$

$$E_x(z) = -iA_1 \frac{1}{\omega\epsilon_0\epsilon_1} k_1 e^{i\beta x} e^{k_1 z}, \tag{2.31}$$

$$E_z(z) = -A_1 \frac{\beta}{\omega\epsilon_0\epsilon_1} e^{i\beta x} e^{k_1 z}. \tag{2.32}$$

for $z < 0$. Here k_i is the component of the wave vector perpendicular to the interface and $1/|k_z|$ is the evanescent decay length. Now the boundary conditions at the interface, which are discussed in the Appendix A.1 (A.5-8), are used. They state that H_y and $\epsilon_i E_z$ in our one dimensional problem have to be continuous, which leads to [57]

$$A_1 = A_2, \tag{2.33}$$

and

$$\frac{k_2}{k_1} = -\frac{\epsilon_2}{\epsilon_1}. \tag{2.34}$$

H_y also has to obey the wave equation:

$$k_1^2 = \beta^2 - k_0^2\epsilon_1, \tag{2.35}$$

$$k_2^2 = \beta^2 - k_0^2\epsilon_2. \tag{2.36}$$

Hence the dispersion relations of surface plasmon polaritons which propagate at the interface are [69]

$$\beta = k_x = k_0\sqrt{\frac{\epsilon_1\epsilon_2}{\epsilon_1+\epsilon_2}}, \tag{2.37}$$

$$k_1 = k_0\sqrt{\frac{\epsilon_1^2}{\epsilon_1+\epsilon_2}}, \tag{2.38}$$

and

$$k_2 = k_0\sqrt{\frac{\epsilon_2^2}{\epsilon_1+\epsilon_2}}. \tag{2.39}$$

Transverse electric surface modes are not possible [57] because for this set

$$E_y(z) = A_2 e^{i\beta x} e^{-k_2 z}, \tag{2.40}$$

$$H_x(z) = -iA_2 \frac{1}{\omega\mu_0} k_2 e^{i\beta x} e^{-k_2 z}, \tag{2.41}$$

$$H_z(z) = A_2 \frac{\beta}{\omega\mu_0} e^{i\beta x} e^{-k_2 z}, \tag{2.42}$$

for $z > 0$, and

$$E_y(z) = A_1 e^{i\beta x} e^{k_1 z}, \tag{2.43}$$

$$H_x(z) = iA_1 \frac{1}{\omega\mu_0} k_1 e^{i\beta x} e^{k_1 z}, \tag{2.44}$$

$$H_z(z) = A_1 \frac{\beta}{\omega\mu_0} e^{i\beta x} e^{k_1 z}, \tag{2.45}$$

for $z < 0$, and the boundary conditions of continuity of E_y and H_x lead to:

$$A_1(k_1 + k_2) = 0. \tag{2.46}$$

Because $Re[k_1] > 0$ and $Re[k_2] > 0$, A_1 and then also $A_2 = A_1$ have to be zero, which means that no transverse electric modes exist. Therefore the only possible solutions are transverse magnetic modes at an interface which obey the following conditions [69]:

$$\epsilon_1 \cdot \epsilon_2 < 0, \tag{2.47}$$

$$\epsilon_1 + \epsilon_2 < 0. \tag{2.48}$$

This means that the real part of one of the dielectric functions, say ϵ_1, must be

negative with the absolute value of ϵ_1 exceeding that of ϵ_2. This conditon holds at an interface between a dielectric and a metal.

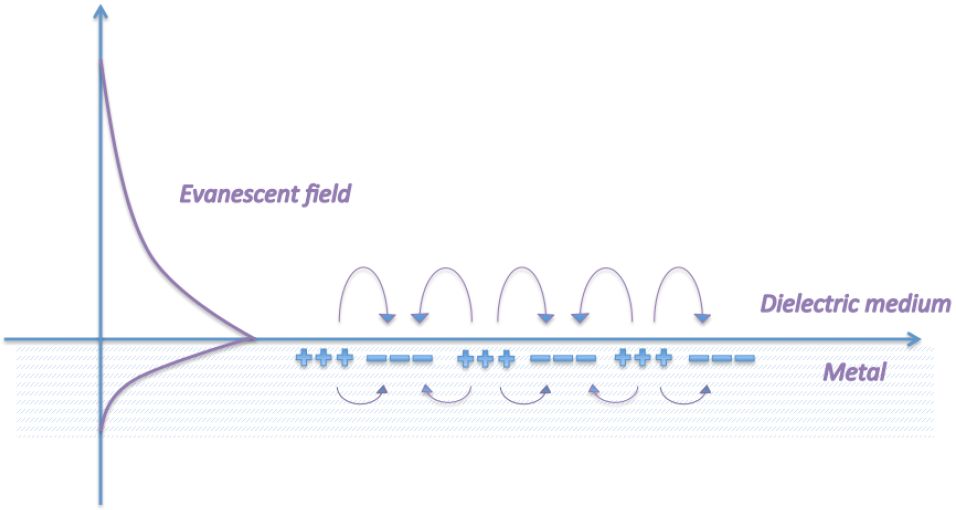

Figure 2.1.: Schematic representation of a surface plasmon polariton which is an electron density wave propagating at the interface between a dielectric and a metal and is confined in perpendicular direction (The fields away from the surface are decaying evanescently).

To obtain the surface plasmon wavelength and its propagation length one uses the dispersion relation along the interface for $\beta = k_x' + ik_x''$ [76]

$$(k_x') + ik_x'' = \sqrt{\frac{(\epsilon_1' + i\epsilon_1'')\epsilon_2}{\epsilon_1' + i\epsilon_1'' + \epsilon_2}}, \tag{2.49}$$

which can be cast to

$$(k_x') + ik_x'' = \frac{\sqrt{\epsilon_1'\epsilon_2\left(1 + i\frac{\epsilon_1''\epsilon_2}{\epsilon_1'\epsilon_2}\right)}}{\sqrt{(\epsilon_1' + \epsilon_2)\left(1 + i\frac{\epsilon_1''}{\epsilon_1' + \epsilon_2}\right)}}, \tag{2.50}$$

and expands the square root under the assumption that $|\epsilon_1''| \ll |\epsilon_1'|$

$$(k_x') + ik_x'' = \sqrt{\frac{\epsilon_1'\epsilon_2}{\epsilon_1'+\epsilon_2}} \frac{1+\frac{1}{2}i\frac{\epsilon_1''}{\epsilon_1'}}{1+\frac{1}{2}i\frac{\epsilon_1''}{\epsilon_1'+\epsilon_2}} = \sqrt{\frac{\epsilon_1'\epsilon_2}{\epsilon_1'+\epsilon_2}} \left(1+\frac{1}{2}i\frac{-\epsilon_1''}{\epsilon_1'+\epsilon_2}+\frac{\epsilon_1''}{\epsilon_1'}\right). \tag{2.51}$$

This leads to the

surface plasmon wavelength and propagation length [76]

$$k_x' \approx \frac{\omega}{c}\left(\frac{\epsilon_1'\epsilon_2}{\epsilon_1'+\epsilon_2}\right)^{1/2}, \tag{2.52}$$

$$\lambda_{ssp} \approx \frac{2\pi}{k_x'}\sqrt{\frac{\epsilon_1'+\epsilon_2}{\epsilon_1'\epsilon_2}}\lambda, \tag{2.53}$$

$$k_x'' \approx \frac{\omega}{c}\left(\frac{\epsilon_1'\epsilon_2}{\epsilon_1'+\epsilon_2}\right)^{3/2}\frac{\epsilon_1''}{2(\epsilon_1')^2}. \tag{2.54}$$

The decay length of the surface plasmon fields are found from the dispersion relation related to the normal wave vector [69].

$$k_{1,z} \approx \frac{\omega}{c}\sqrt{\frac{\epsilon_1'^2}{\epsilon_1'+\epsilon_2}}\left[1+i\frac{\epsilon_1''}{2\epsilon_1'}\right], \tag{2.55}$$

$$k_{2,z} \approx \frac{\omega}{c}\sqrt{\frac{\epsilon_2'^2}{\epsilon_1'+\epsilon_2}}\left[1-i\frac{\epsilon_1''}{2(\epsilon_1'+\epsilon_2)}\right]. \tag{2.56}$$

2.2. Localized surface plasmon resonances

There also exist localized surface plasmon resonances on metallic nanoparticles [86] [57] [69]. To find the fundamental localized surface plasmon resonance of a sphere we first employ the quasistatic approximation. This approximaten states that if a particle is much smaller than the wavelength of light the phase of the harmonically oscillating electromagnetic field can be seen as constant over the particle volume. So we assume an uniform electrostatic field $\mathbf{E} = E_0\mathbf{z}$ and look for a solution of the Laplace equation (see Appendix A.4). The solutions of the Laplace equation for the potential inside and outside the sphere have the following form [40]

$$\phi_{in}(r,\theta) = \sum_{l=0}^{\infty}[A_l r^l]P_l(\cos\theta), \tag{2.57}$$

$$\phi_{out}(r,\theta) = \sum_{l=0}^{\infty}[B_l r^l + C_l r^{-(l+1)}]P_l(\cos\theta). \tag{2.58}$$

To determine the coefficients the boundary conditions are used:

$$-\frac{1}{a}\frac{\partial\phi_{in}}{\partial\theta}\Big|_{r=a} = -\frac{1}{a}\frac{\partial\phi_{out}}{\partial\theta}\Big|_{r=a}, \tag{2.59}$$

$$-\epsilon_0\epsilon\frac{\partial\phi_{in}}{\partial r}\Big|_{r=a} = -\epsilon_0\epsilon_m\frac{\partial\phi_{out}}{\partial r}\Big|_{r=a}, \tag{2.60}$$

$$\phi_{out} = -E_0 z \qquad r\to\infty. \tag{2.61}$$

This leads to the following equations

$$A_1 = -E_0 + \frac{C_1}{a^3}, \tag{2.62}$$

$$A_l = \frac{C_l}{a^{2l+1}} \qquad \text{for } l\neq 1, \tag{2.63}$$

$$\frac{\epsilon}{\epsilon_m}A_1 = -E_0 - 2\frac{C_1}{a^3}, \tag{2.64}$$

$$\frac{\epsilon}{\epsilon_m} l A_l = -(l+1)\frac{C_l}{a^{2l+1}} \quad \text{for } l \neq 1, \tag{2.65}$$

which are solved with [40]

$$A_1 = -\left(\frac{3}{2+\epsilon/\epsilon_m}\right) E_0, \tag{2.66}$$

and

$$C_1 = \left(\frac{\epsilon/\epsilon_m - 1}{\epsilon/\epsilon_m + 2}\right) a^3 E_0. \tag{2.67}$$

Therfore we obtain [57]

$$\phi_{in} = \frac{-3\epsilon_m}{\epsilon + 2\epsilon_m} E_0 r \cos\theta, \tag{2.68}$$

$$\phi_{out} = -E_0 r \cos\theta + \frac{\epsilon - \epsilon_m}{\epsilon + 2\epsilon_m} E_0 a^3 \frac{\cos\theta}{r^2}. \tag{2.69}$$

Inside the sphere we find a constant electric field parallel to the applied field and the potential outside the sphere is a superposition of a dipole located at the particle center and the applied field and therefore can be written with the dipole moment $\mathbf{p}$ as [57]:

$$\phi_{out} = -E_0 r \cos\theta + \frac{\mathbf{p}\cdot\mathbf{r}}{4\pi\epsilon_0\epsilon_m r^3}, \tag{2.70}$$

$$\mathbf{p} = 4\pi\epsilon_0\epsilon_m a^3 \frac{\epsilon - \epsilon_m}{\epsilon + 2\epsilon_m}\mathbf{E}_0. \tag{2.71}$$

This can be seen by evaluating the electric fields from the potentials

$$\mathbf{E} = -\nabla\phi, \tag{2.72}$$

$$\mathbf{E}_{in} = \frac{3\epsilon_m}{\epsilon + 2\epsilon_m}\mathbf{E}_0, \tag{2.73}$$

$$\mathbf{E}_{out} = \mathbf{E}_0 + \frac{3\mathbf{n}(\mathbf{n}\cdot\mathbf{p}) - \mathbf{p}}{4\pi\epsilon_m\epsilon_0}\frac{1}{r^3}, \tag{2.74}$$

and comparing the scattered field to the electric field of a dipole:

$$\mathbf{E} = \frac{1}{4\pi\epsilon_0\epsilon_m}\left(k^2(\mathbf{n}\times\mathbf{p})\times\mathbf{n}\frac{e^{ikr}}{r} + [3\mathbf{n}(\mathbf{n}\cdot\mathbf{p}) - \mathbf{p}]\left(\frac{1}{r^3} - \frac{ik}{r^2}\right)e^{ikr}\right), \tag{2.75}$$

$$\mathbf{E} = \frac{3\mathbf{n}(\mathbf{n}\cdot\mathbf{p}) - \mathbf{p}}{4\pi\epsilon_0\epsilon_m}\frac{1}{r^3} \qquad kr \ll 1, \tag{2.76}$$

where $k = 2\pi/\lambda$ and $\mathbf{n}$ is the unit vector from the dipole position to the observation point. An illumination with a plane wave

$$\mathbf{E}(\mathbf{r}, t) = \mathbf{E}_0 e^{-i\omega t}, \tag{2.77}$$

induces a radiating oscillating dipole

$$\mathbf{p} = \epsilon_0\epsilon_m\alpha\mathbf{E}_0 e^{-i\omega t}, \tag{2.78}$$

which leads to a scattering of the plane wave. The polarizability

$$\alpha = 4\pi a^3\frac{\epsilon - \epsilon_m}{\epsilon + 2\epsilon_m}, \tag{2.79}$$

$$\mathbf{p} = \epsilon_m\epsilon_0\alpha\mathbf{E}_0, \tag{2.80}$$

experiences a resonance under the condition that $|\epsilon + 2\epsilon_m|$ is a minimum, which, for a small or slowly-varying $\Im m[\epsilon]$ around the resonance simplifies to

$$Re[\epsilon(\omega)] = -2\epsilon_m. \tag{2.81}$$

This is called the Fröhlich condition [57]. The associated mode is the dipole surface plasmon of a spherical nanoparticle.

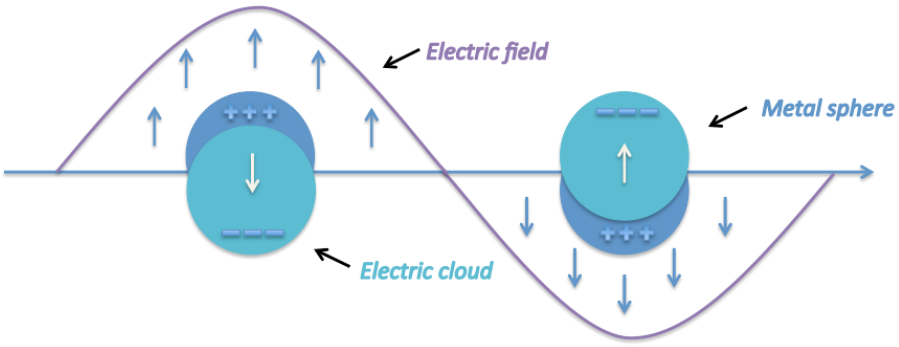

Figure 2.2.: Schematic representation of a localized surface plasmon resonance in a metallic nanoparticle of the size comparable to or smaller than the wavelength of light. The impinging electromagnetic wave polarizes the electrons of the metal and the restoring force leads to the plasmonic oscillation.

The scattering and absorption cross sections are given by [89]

$$C_{sca} = \frac{8\pi}{3} k^4 a^6 \left| \frac{\epsilon - \epsilon_m}{\epsilon + 2\epsilon_m} \right|^2, \tag{2.82}$$

and

$$C_{abs} = 4\pi k a^3 \Im m \left[\frac{\epsilon - \epsilon_m}{\epsilon + 2\epsilon_m} \right]. \tag{2.83}$$

The sum of scattering and absorption efficiency is the extinction:

$$C_{ext} = C_{sca} + C_{abs}. \tag{2.84}$$

2.3. Substrate effects

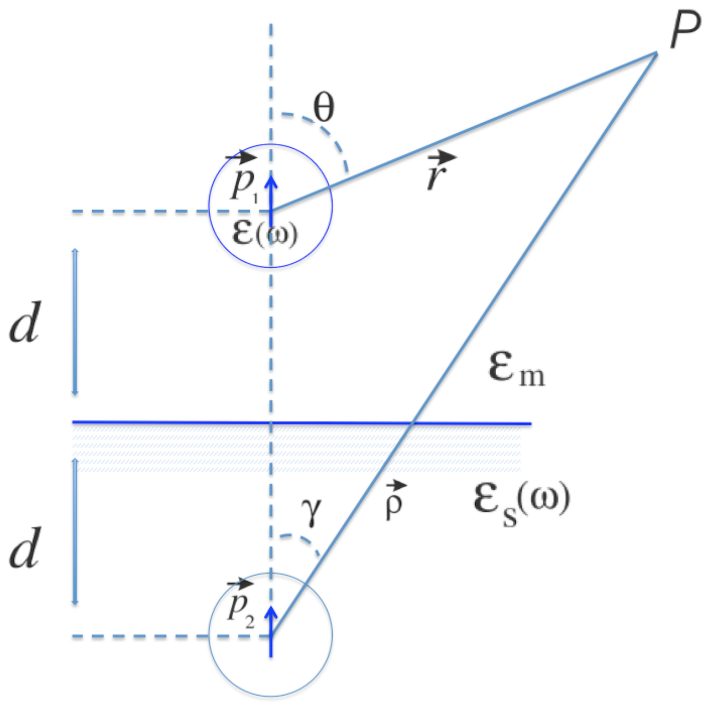

Figure 2.3.: Image charge model of a conducting sphere near a substrate [73].

The influence of a substrate on the plasmon resonance can be studied in the quasistatic regime with the well known image charge model [1,40,46,69,73,88]. Therefore we consider a spherical metallic nanoparticle near a substrate which is illuminated by an electromagetic wave. By using the quasistatic approximation and neglecting higher order multipole moments the induced charges can be represented as a dipole $\mathbf{p}_1 = \mathbf{l}q$. To account for the influence of the substrate we then use the image charge model.

In this image charge model a potential of a charge near a substrate is given as the sum of the potential of the charge and of its image charge [73]

$$\phi = \frac{1}{4\pi\epsilon_0\epsilon_m}\left(\frac{q}{r} + \frac{q'}{\rho}\right), \tag{2.85}$$

with

$$q' = q\frac{\epsilon_m - \epsilon_s}{\epsilon_m + \epsilon_s}, \tag{2.86}$$

beeing the image point charge.

Here ϵ_0 is the permittivity of vacuum, ϵ_m is the permittivity of the background, ϵ_s is the permittivity of the substrate and r and ρ are the distances from the charges q and q' to the point of observation. In the case of the sphere near the substrate excited by an electric field perpendicular to the substrate this leads to the following potential [73]:

$$\phi_\perp(P) = -E_\perp^0 r\cos\theta - \frac{p_1\cos\Theta}{4\pi\epsilon_0\epsilon_m r^2} - \frac{p_2\cos\gamma}{4\pi\epsilon_0\epsilon_m\rho^2}. \tag{2.87}$$

Here θ and γ are angles between the axis perpendicular to the substrate and the vectors r and ρ (see Fig. 2.3). With the image dipole

$$\mathbf{p}_2 = \mathbf{p}_1\frac{\epsilon_s - \epsilon_m}{\epsilon_s + \epsilon_m}, \tag{2.88}$$

we obtain

$$\phi_\perp(P) = -E_\perp^0 r\cos\theta - \frac{p_1}{4\pi\epsilon_0\epsilon_m}\left(\frac{\cos\theta}{r^2} + \frac{\cos\gamma}{\rho^2}\left(\frac{\epsilon_s(\omega) - \epsilon_m}{\epsilon_s(\omega) + \epsilon_m}\right)\right), \tag{2.89}$$

from which the local electric field at the sphere can be calculated:

$$\mathbf{E}_\perp = \mathbf{E}_\perp^0 + \frac{\mathbf{p}_1}{2\pi\epsilon_0\epsilon_m r^3}\left(\frac{\epsilon_s - \epsilon_m}{\epsilon_s + \epsilon_m}\right). \tag{2.90}$$

This can also be written with the polarizability of the sphere

$$\mathbf{p}_1 = \epsilon_0 \epsilon_m \alpha \mathbf{E}_\perp, \tag{2.91}$$

$$\mathbf{E}_\perp = \mathbf{E}_\perp^0 \left(1 - \frac{\alpha}{16\pi d^3} \frac{\epsilon_s - \epsilon_m}{\epsilon_s + \epsilon_m}\right)^{-1}. \tag{2.92}$$

Here d is the distance from the center of the sphere to the substrate surface. From this we can calculate the perpendicular component the effective polarizability

$$\alpha_\perp^{eff} = \frac{\alpha}{(1 - \frac{\alpha}{16\pi d^3}(\frac{\epsilon_s - \epsilon_m}{\epsilon_s + \epsilon_m}))}, \tag{2.93}$$

which can also be written with the depolarization factor

$$\alpha_\perp^{eff} = \frac{V(\epsilon(\omega) - \epsilon_m)}{\epsilon_m + L_\perp(\epsilon(\omega) - \epsilon_m)}, \tag{2.94}$$

$$L_\perp = \frac{1}{3}\left[1 - \frac{1}{4}\left(\frac{R}{d}\right)^3 \left(\frac{\epsilon_s(\omega) - \epsilon_m}{\epsilon_s(\omega) + \epsilon_m}\right)\right], \tag{2.95}$$

where

$$V = \frac{4\pi R^3}{3}, \tag{2.96}$$

is the volume of the sphere. For the system consisting of a dipole and its image dipole the polarizatbility is then given by [73]

$$\alpha_\perp^{eff} = \left[\frac{V(\epsilon(\omega) - \epsilon_m)}{\epsilon_m + L_\perp(\epsilon(\omega) - \epsilon_m)}\right] \frac{2\epsilon_s(\omega)}{(\epsilon_s(\omega) + \epsilon_m)}. \tag{2.97}$$

If a parallel field is applied, the local electric field can again be obtained from the potential:

$$\mathbf{E}_\parallel = \mathbf{E}_\parallel^0 \left(1 - \frac{\alpha}{32\pi d^3} \frac{\epsilon_s - \epsilon_m}{\epsilon_s + \epsilon_m}\right)^{-1}. \tag{2.98}$$

For the parallel component of the effective polarizabilty one obtains

$$\alpha_{\parallel}^{eff} = \frac{V(\epsilon(\omega) - \epsilon_m)}{\epsilon_m + L_{\parallel}(\epsilon(\omega) + \epsilon_m)}, \tag{2.99}$$

with

$$L_{\parallel} = \frac{1}{3}\left[1 - \frac{1}{8}\left(\frac{R}{d}\right)^3 \left(\frac{\epsilon_s(\omega) - \epsilon_m}{\epsilon_s(\omega) + \epsilon_m}\right)\right], \tag{2.100}$$

the depolarizing factor. For the system consisting of a dipole and its image dipole the polarizatbility is then given by [73]

$$\alpha_{\parallel}^{eff} = \left[\frac{V(\epsilon(\omega) - \epsilon_m)}{\epsilon_m + L_{\parallel}(\epsilon(\omega) - \epsilon_m)}\right] \frac{2\epsilon_s(\omega)}{(\epsilon_s(\omega) + \epsilon_m)}. \tag{2.101}$$

By using these polarizabilities in the optical cross sections (given in section 2.2) the influence of the substrate can be studied [73]. In the next section we show simulation results for both cases.

Results

Applied electric field perpendicular to the substrate

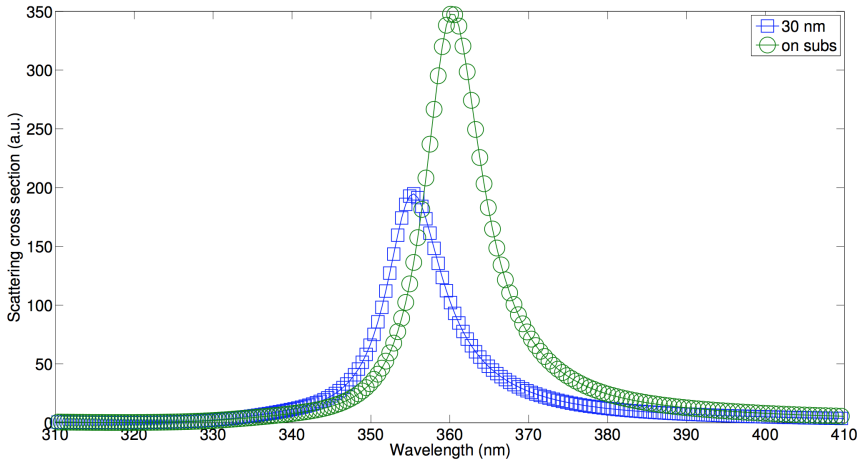

Figure 2.4.: Comparison of scattering cross sections of a silver sphere with a radius of 10 nm situated on a glass substrate with a refractive index of 1.51 and located 30 nm away from the substrate which is illuminated with an electric field perpendicular to the substrate (computed by using the formulas 2.82 and 2.97). For the closer distance to the substrate a red shift of the plasmon resonance is observed. This red shift can be understood with the simple image charge model. The electric field of the image dipole works against the restoring force of the electrons resulting in the red shift [67].

In Fig. 2.4 we present simulation results for the scattering cross section of a silver sphere with a radius of 10 nm approaching a glass substrate with a refractive index of 1.51 which is illuminated by an electric field which is perpendicular to the substrate (obtained by using the formulas 2.82 and 2.97). For closer distances to the glass substrate the resonance of the scattering cross section shifts to lower photon energies. This red shift can be understood with the simple image charge model. The electric field of the image dipole works against the restoring force of the electrons resulting in the red shift [67].

Applied electric field parallel to the substrate

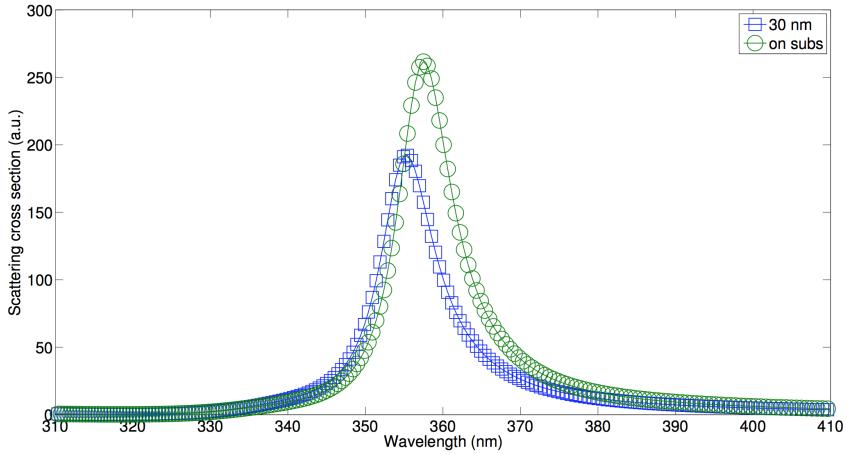

Figure 2.5.: Comparison of scattering cross sections of a silver sphere with a radius of 10 nm situated on a glass substrate with a refractive index of 1.51 and located 30 nm away from the substrate which is illuminated with an electric field parallel to the substrate (computed by using the formulas 2.82 and 2.101). For the closer distance to the substrate a red shift of the plasmon resonance is observed. This red shift can be understood with the simple image charge model. The electric field of the image dipole works against the restoring force of the electrons resulting in the red shift [67].

In Fig. 2.5 we present simulation results for the scattering cross section of a silver sphere with a radius of 10 nm approaching a glass substrate with a refractive index of 1.51 which is illuminated by an electric field which is parallel to the substrate (obtained by using the formulas 2.82 and 2.101). For closer distances to the glass substrate the resonance of the scattering cross section shifts to lower photon energies. This red shift can be understood with the simple image charge model. The electric field of the image dipole works against the restoring force of the electrons resulting in the red shift [67]. The substrate effect is stronger if the applied field is perpendicular to the substrate because of the larger incuded dipole field.

For a quantitative description beyond the image-charge framework one needs to in-

clude the multipole character of the induced charges [73] and the inhomogeneous character of the electric field [69, 73]. In the next chapter we will present numerical methods which allow the solutions of the full Maxwell equations.

3. Simulation of plasmonic nanoparticles

The simulation of optical properties of plasmonic nanoparticles relies on the solution of Maxwell's equations [22, 57]. An analytic solution is only possible for certain geometries. The Mie solution [6, 47, 63] describes the scattering of a plane wave by a homogeneous sphere. The solution takes the form of an infinite series of spherical multipole partial waves. There also exists the Mie-Gans-solution [23] which is an extension for oblate and prolate spheroidal particles. For particles with abritary shape no analytic solutions are possible and numerical methods need to be employed.

There are two main catagories of numerical methods. Differential methods which solve Maxwell's equations in their differential form, and integral methods which transform them to integral form [22]. Popular differential methods are the finite difference time domain method [30, 90, 100], the finite elements method [11, 38, 77] and the discontinous Galerkin time-domain method [85]. Popular integral methods are the volume integral equations [59], the discrete dipole approximation [12–14, 74], the surface integral equations [43, 58], and the potential based boundary element method [24–26, 33, 35].

Other approaches used in plasmonics are the T-matrix method [44] and the rigorous coupled wave analysis method [51]. Alternativly one can also use time-dependent density functional theory to simulate the optical properties of small metal clusters [49, 102]. For Gap plasmonics quantum corrected models are available as well [17, 32, 45].

3.1. Boundary Element Method for full Maxwell equations

The boundary element method is a computational scheme which allows to solve Maxwell's equations for a system consisting of dielectric regions which are described by homogeneous and isotropic dielectric functions, and are separated by a sharp boundary [25, 26, 33, 35]. By using the Helmholtz theorem [28] one can relate the electromagnetic fields $\mathbf{E}$ and $\mathbf{B}$ to the scalar and vector potentials ϕ and $\mathbf{A}$ via

$$\mathbf{E} = ik\mathbf{A} - \nabla\phi, \tag{3.1}$$

$$\mathbf{B} = \nabla \times \mathbf{A}, \tag{3.2}$$

With the Lorentz gauge condition [40]

$$\nabla \cdot \mathbf{A} = ik\epsilon\phi, \tag{3.3}$$

the Maxwell equations (in this section Gauss units are used) can then be rewritten in the following [26] [35]

Helmholtz equations:

$$\nabla^2\phi + k^2\epsilon\phi = -4\pi\rho, \tag{3.4}$$

$$\nabla^2\mathbf{A} + k^2\epsilon\mathbf{A} = -\frac{4\pi}{c}\mathbf{j}. \tag{3.5}$$

Here k is the wavenumber in vacuum, ϵ is the permittivity, ρ is the charge density, $\mathbf{j}$ is the current density and c is the speed of light.

They can be solved on both sides of the boundary with the

Green functions of the media [10]

$$G_j(\mathbf{r},\mathbf{r}') = \frac{e^{(ik_j|\mathbf{r}-\mathbf{r}'|)}}{|\mathbf{r}-\mathbf{r}'|}, \tag{3.6}$$

obtained from

$$(\nabla^2 + k_j^2)G_j(\mathbf{r},\mathbf{r}') = -4\pi\delta(\mathbf{r}-\mathbf{r}'), \tag{3.7}$$

and appropriate boundary conditions of outgoing waves at infinity. Therefore the square root of $k_j = \sqrt{\epsilon_j\mu_j}k$ is understood to yield a positive imaginary part.

Because of the discontinuity [26] [35] of the fields and potentials at the sharp boundary additional surface charge and surface current distributions are introduced. The solutions which are valid in whole space then look the following way [26]:

$$\phi(\mathbf{r}) = \int_{\partial S_j} G_j(\mathbf{r},\mathbf{s}')\sigma_j(\mathbf{s}')ds' + \phi^e(\mathbf{r}), \tag{3.8}$$

$$\mathbf{A}(\mathbf{r}) = \int_{\partial S_j} G_j(\mathbf{r},\mathbf{s}')\mathbf{h}_j(\mathbf{s}')ds' + \mathbf{A}^e(\mathbf{r}), \tag{3.9}$$

with

$$\phi^e(\mathbf{r}) = \frac{1}{\epsilon_j}\int G_j(\mathbf{r},\mathbf{r}')\rho(\mathbf{r}')dr', \tag{3.10}$$

$$\mathbf{A}^e(\mathbf{r}) = \frac{\mu_j}{c}\int G_j(\mathbf{r},\mathbf{r}')\mathbf{j}(\mathbf{r}')dr', \tag{3.11}$$

describing the external pertubation. For a numerical implementation one changes from boundary integrals to boundary elements (see Fig. 3.1). This reduces the spatial dependence of each quantity to a discrete number of representative points:

$$\int_{S_j} G_j(\mathbf{s}_l - \mathbf{s}')\sigma_j(\mathbf{s}')d\mathbf{s}' = \sum_{l'} G_{j,ll'}\sigma_j(\mathbf{s}_{l'})\Delta S_{l'}. \tag{3.12}$$

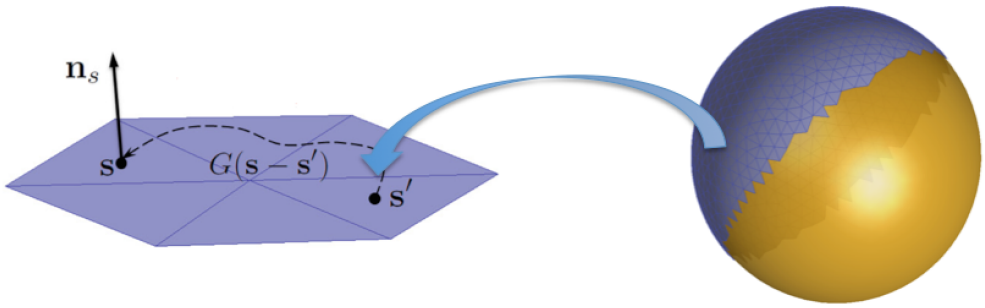

Figure 3.1.: In the boundary element method the surface of a metallic nanoparticle gets discretized in small boundary elements. The spatial dependence of each quantity is reduced to a discrete number of representative points and the Green functions describe the interactions between them [26] [35].

We will further adopt a compact matrix notation (where the summation is meant to be included in products such as $G_j\sigma_j$) and calculate the unkown surface currents and surface charges with the use of the boundary conditions of Maxwell's theory. The continuity of the tangential electric field leads to the continuity of the scalar potential

$$G_1\sigma_1 = G_2\sigma_2 + \varphi, \tag{3.13}$$

with

$$\varphi = \phi_2^e - \phi_1^e, \tag{3.14}$$

and

$$G_1 = G_{11} - G_{21}, \tag{3.15}$$

$$G_2 = G_{22} - G_{12}. \tag{3.16}$$

Here G_{11} connects points on the inner boundary, G_{22} connects points on the outer boundary, and G_{12} and G_{21} connect points from the inner to the outer boundary and vice versa. [26] [35]. A field induced within a medium is produced exclusively by the interface charges lying on the side of the boundary facing this medium. This allows

a generalization to an arbitrary number of media (see Fig. 3.2). The continuity of the normal magnetic induction leads to the continuity of the vector potential

$$G_1\mathbf{h}_1 = G_2\mathbf{h}_2 + \mathbf{a}, \tag{3.17}$$

with

$$\mathbf{a} = \mathbf{A_2^e} - \mathbf{A_1^e}. \tag{3.18}$$

From the continuity of the normal electric displacement one obtains

$$H_1\epsilon_1\sigma_1 - H_2\epsilon_2\sigma_2 - ik\mathbf{n}(G_1\epsilon_1\mathbf{h_1} - G_2\epsilon_2\mathbf{h_2}) = D^{e\prime}, \tag{3.19}$$

with

$$D^{e\prime} = \epsilon_1(ik\mathbf{na_1} - \phi_1^{e\prime}) - \epsilon_2(ik\mathbf{na_2} - \phi_2^{e\prime}), \tag{3.20}$$

where $\mathbf{n}$ is the outer surface vector of the boundary. In addition,

$$H_{1,2} = F \pm 2\pi, \tag{3.21}$$

with F beeing the surface derivative of the Green function.

One has to be careful about a singular contribution originating from the limit $\mathbf{r} \to \mathbf{s}$. This can be seen by studying the effect on the quasistatic ($kr \ll 1$) Green function [34] [26] [35]

$$G(\mathbf{r} - \mathbf{r}') = \frac{1}{(|\mathbf{r} - \mathbf{r}'|)}. \tag{3.22}$$

We consider the limit

$$\lim_{\mathbf{r}\to\mathbf{s}} \hat{\mathbf{n}} \cdot \nabla \int G(\mathbf{r}, \mathbf{s})\sigma(\mathbf{s}')ds', \tag{3.23}$$

for the following coordinate system

$$\hat{\mathbf{n}} = \hat{\mathbf{e}}_\mathbf{z}, \tag{3.24}$$

$$\mathbf{r} = (0, 0, z), \tag{3.25}$$

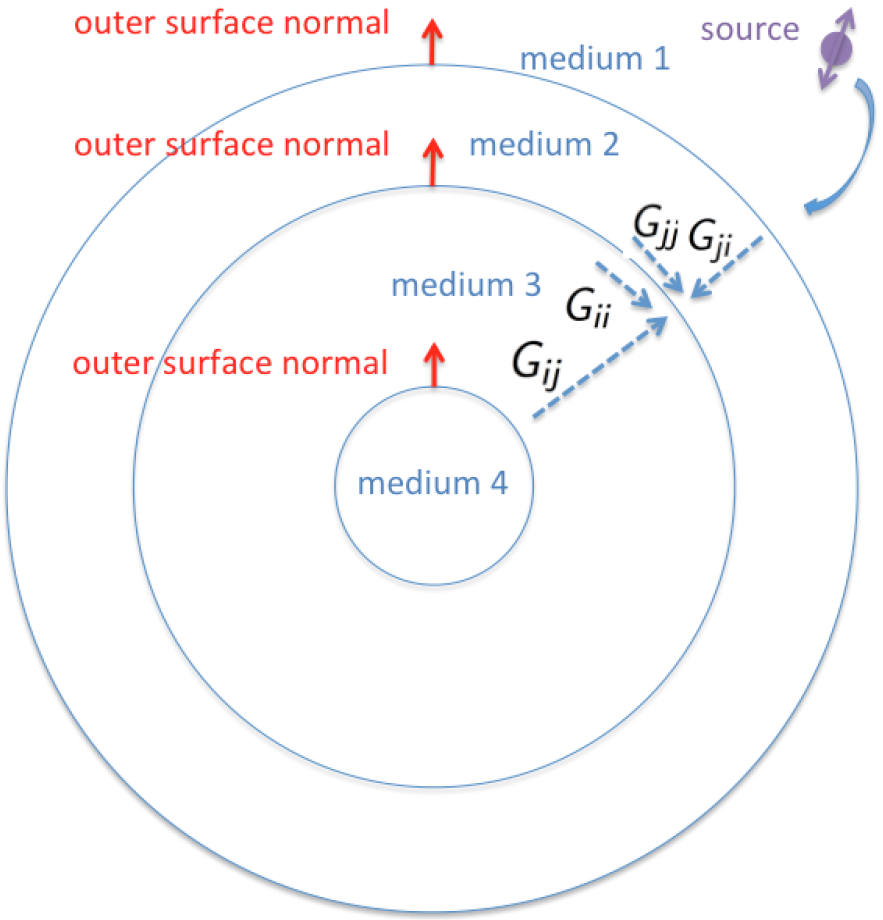

Figure 3.2.: Its also possible to generalize to an arbitary number of media. Charges (and currents) that cannot be connected without crossing any interface are blind to each other. A source in medium 1 can only excite the outer boundary of medium 2, but neither the inner boundary of medium 2 nor the boundaries of medium 3 and 4. G_{ii} connects points on the inner boundary, G_{jj} connects points on the outer boundary, and G_{ij} and G_{ji} connect points from the inner to the outer boundary and vice versa [26] [35].

$$\mathbf{s}' = \rho(\cos\phi, \sin\phi, 0), \tag{3.26}$$

and find

$$\lim_{z\to 0} \hat{\mathbf{n}} \cdot \int \frac{\mathbf{r}-\mathbf{s}'}{|\mathbf{r}-\mathbf{s}'|^3} ds' \to \lim_{z\to 0} 2\pi z \int_0^R \rho d\rho (\rho^2 + z^2)^{-\frac{3}{2}} = 2\pi. \tag{3.27}$$

Finally, the continuity of the tangential magnetic field translates to

$$H_1\mathbf{h}_1 - H_2\mathbf{h}_2 - ik\mathbf{n}(G_1\epsilon_1\sigma_1 - G_2\epsilon_2\sigma_2) = \boldsymbol{\alpha}, \tag{3.28}$$

with

$$\boldsymbol{\alpha} = \mathbf{a}' + ik\mathbf{n}(\epsilon_1\phi_1^e - \epsilon_2\phi_2^e). \tag{3.29}$$

Here

$$\mathbf{n} \times (\mathbf{B}_2 - \mathbf{B}_1) = \mathbf{n} \times (\nabla \times \delta\mathbf{A}) = \nabla(\mathbf{n} \cdot \delta\mathbf{A}) - (\mathbf{n} \cdot \nabla)\delta\mathbf{A} = 0, \tag{3.30}$$

and

$$\nabla(\mathbf{n} \cdot \delta\mathbf{A}) = \mathbf{n}(\nabla \cdot \delta\mathbf{A}), \tag{3.31}$$

was used. These equations can now be recast in order to determine the surface charges and surface currents. From the continuity of the potentials the surface charges and currents on the two sides of the boundary can be related to each other:

$$\sigma_1 = G_1^{-1}(G_2\sigma_2 + \varphi), \tag{3.32}$$

$$\mathbf{h}_1 = G_1^{-1}(G_2\mathbf{h}_2 + \mathbf{a}). \tag{3.33}$$

By inserting these expressions in the other two equations and using

$$H_1\mathbf{h_1} = H_1G_1^{-1}(G_2\mathbf{h_2} + \mathbf{a}) = \Sigma_1(G_2\mathbf{h_2} + \mathbf{a}), \tag{3.34}$$

$$H_2\mathbf{h_2} = \Sigma_2 G_2 \mathbf{h_2}, \tag{3.35}$$

with

$$\Sigma_{1,2} = H_{1,2} G_{1,2}^{-1}, \tag{3.36}$$

and

$$H_1 \epsilon_1 \sigma_1 = \Sigma_1 L_1 G_1 \sigma_1, \tag{3.37}$$

$$L_{1,2} = G_{1,2} \epsilon_{1,2} G_{1,2}^{-1}, \tag{3.38}$$

we get

$$(\Sigma_1 - \Sigma_2) G_2 h_2 - ik\mathbf{n}(L_1 - L_2) G_2 \sigma_2 = \mathbf{a}' + ik\mathbf{n}(\epsilon_1 \phi_1^e - \epsilon_2 \phi_2^e) - \Sigma_1 \mathbf{a} + ik\mathbf{n} L_1 \varphi, \tag{3.39}$$

$$(\Sigma_1 L_1 - \Sigma_2 L_2) G_2 \sigma_2 - ik\mathbf{n}(L_1 - L_2) G_2 \mathbf{h}_2 = D^{e\prime} - \Sigma_1 L_1 \varphi + ik\mathbf{n} L_1 \mathbf{a}. \tag{3.40}$$

In this way the surface charges and currents on the outer side of the interface can be computed

$$\sigma_2 = G_2^{-1} \Sigma^{-1} [D^e + ik\mathbf{n}(L_1 - L_2)(\Sigma_1 - \Sigma_2)^{-1} \boldsymbol{\alpha}], \tag{3.41}$$

$$\mathbf{h}_2 = G_2^{-1} (\Sigma_1 - \Sigma_2)^{-1} [ik\mathbf{n}(L_1 - L_2) G_2 \sigma_2 + \alpha], \tag{3.42}$$

with

$$D^e = \epsilon_1 (ik\mathbf{n}\mathbf{A}_1^e - \phi_1^{e\prime}) - \epsilon_2 (ik\mathbf{n}\mathbf{A}_2^e - \phi_2^{e\prime}) - \Sigma_1 L_1 \varphi + ik\mathbf{n} L_1 \mathbf{a}, \tag{3.43}$$

$$\boldsymbol{\alpha} = \mathbf{a}' + ik\mathbf{n}(\epsilon_1 \phi_1^e - \epsilon_2 \phi_2^e) - \Sigma_1 \mathbf{a} + ik\mathbf{n} L_1 \varphi, \tag{3.44}$$

and

$$\Sigma = \Sigma_1 L_1 - \Sigma_2 L_2 + k^2 \mathbf{n}(L_1 - L_2)(\Sigma_1 - \Sigma_2)^{-1}\mathbf{n}(L_1 - L_2). \tag{3.45}$$

With the scalar and vector potentials the electromagnetic fields **E**, **B** and with the use of the Poynting vector one can compute the

optical cross sections [40] :

$$P_{sca} = n_b \oint Re(\mathbf{n}(\mathbf{E} \times \mathbf{B}^*))da, \tag{3.46}$$

$$P_{ext} = -\frac{1}{n_b} \oint Re(\mathbf{n}(\mathbf{E} \times \mathbf{B}^*_{inc} + \mathbf{E}^*_{inc} \times \mathbf{B}))da, \tag{3.47}$$

$$P_{abs} = P_{ext} - P_{sca}. \tag{3.48}$$

Here n_b is the refractive index of the dielectric background and $\mathbf{S} = \mathbf{E} \times \mathbf{B}$ is the Poynting vector. $\mathbf{E}_{inc}$ and $\mathbf{B}_{inc}$ are the vector fields of the incident wave and **E** and **B** are the total fields.

3.2. Boundary Element Method for quasistatic approximation

For very small particles ($d \ll \lambda$) [65] the electromagnetic interaction between different points is almost instantaneous and the terms connecting the electric and magnetic fields in the Maxwell equations disappear ($k \to 0$). The Helmholz equation then reduces to the Poisson equation which can be solved with the

quasistatic Green function [34] [26] [35]

$$G(\mathbf{r}, \mathbf{r}') = \frac{1}{|\mathbf{r} - \mathbf{r}'|}, \tag{3.49}$$

obtained from

$$\nabla^2 G(\mathbf{r}, \mathbf{r}') = -4\pi\delta(\mathbf{r} - \mathbf{r}'), \tag{3.50}$$

and appropriate boundary conditions.

In this way we can write down the solution of the Poisson equation with the quasistatic Green function

$$\phi(r) = \int_{\partial S} G(\mathbf{r}, \mathbf{s}')\sigma(\mathbf{s}')ds' + \phi^e(\mathbf{r}), \tag{3.51}$$

where we again additionaly introduced a surface charge which is found by the use of the boundary conditions of Maxwell theory. To use the boundary condition related to the electric displacement we need to evaluate the surface derivative of the potential

$$\lim_{\mathbf{r}\to\mathbf{s}} \mathbf{n} \cdot \nabla\phi(\mathbf{r}) = \lim_{\mathbf{r}\to\mathbf{s}} \frac{\partial\phi(\mathbf{r})}{\partial n} = \lim_{\mathbf{r}\to\mathbf{s}} \int_{\partial V} \frac{\partial G(\mathbf{r}, \mathbf{s}')}{\partial n}\sigma(\mathbf{s}')ds' + \frac{\partial\phi^e(\mathbf{r})}{\partial n}, \tag{3.52}$$

where some care has to be taken about the limit $\mathbf{r}$ to $\mathbf{s}$ [34]:

$$\lim_{z\to\pm 0} \mathbf{n} \cdot \int \frac{\mathbf{r} - \mathbf{s}}{|\mathbf{r} - \mathbf{s}|^3} ds' = \lim_{z\to\pm 0} 2\pi z \int_0^R \frac{\rho d\rho}{(\rho^2 + z^2)^{3/2}} = \pm 2\pi. \tag{3.53}$$

With this singular contribution we obtain

$$\frac{\partial\phi(\mathbf{s})}{\partial n} = \pm 2\pi\sigma(\mathbf{r}) + \int_{\partial V} F(\mathbf{s},\mathbf{s}')\sigma(\mathbf{s}')ds' + \frac{\partial\phi^e(\mathbf{s})}{\partial n}, \tag{3.54}$$

with the surface derivative of the Green function

$$F(\mathbf{s},\mathbf{s}') = \frac{\partial G(\mathbf{s},\mathbf{s}')}{\partial n}, \tag{3.55}$$

which fulfills the sum rule [21]

$$\oint_{\partial V} F(\mathbf{s},\mathbf{s}')ds' = 2\pi. \tag{3.56}$$

For a numerical implementation one changes from boundary integrals to boundary elements [26] [35] and calculates the surface charge with the use of the boundary conditions of Maxwell's theory. From the continuity of the tangential electric field one sees that surface charges on both sides of the boundary are the same, and the boundary condition related to the electric displacement leads to

$$\epsilon_2\left(2\pi\sigma + F\sigma + \frac{\partial\phi^e}{\partial n}\right) = \epsilon_1\left(-2\pi\sigma + F\sigma + \frac{\partial\phi^e}{\partial n}\right), \tag{3.57}$$

or

$$(\Lambda + F)\sigma = -\frac{\partial\phi^e}{\partial n} \tag{3.58}$$

with

$$\Lambda = 2\pi\frac{\epsilon_2 + \epsilon_1}{\epsilon_2 - \epsilon_1}, \tag{3.59}$$

from which the surface charge can be calculated

$$\sigma = -(\Lambda + F)^{-1}\frac{\partial\phi^e}{\partial n}. \tag{3.60}$$

Here again a compact matrix notation was used. With the surface charge one can find the dipole moment and the

quasti static optical cross sections [40] [86]:

$$P_{sca} = \frac{8\pi}{3} k^4 |\mathbf{d}_\lambda|^2, \tag{3.61}$$

$$P_{abs} = 4\pi k \Im m(\hat{\mathbf{e}}_\lambda \cdot \mathbf{d}_\lambda), \tag{3.62}$$

$$P_{ext} = P_{sca} + P_{abs}. \tag{3.63}$$

3.3. Discrete Dipole Approximation

The discrete dipole approximation is another numerical method to calculate the optical cross sections. In this method the scatterer gets represented by dipoles [12].

The lattice spacing d between these dipoles has to be sufficiently small compared to the wavelength of the incident wave and sufficiently small to represent the scatterer [13]:

$$d \leq \frac{1}{k|m|}. \tag{3.64}$$

Here k is the wavenumber and m is the refractive index.

Every dipole then has a dipole moment

$$\mathbf{P}_j = \alpha_j \mathbf{E}_j, \tag{3.65}$$

where α_j is the polarizability and E_j is the electric field, consisting of the incident field and the contributions from the other dipoles

$$\mathbf{E}_j = \mathbf{E}_{inc,j} - \sum_{k \neq j} \mathbf{A}_{jk} \mathbf{P}_k, \tag{3.66}$$

with the interaction matrix

$$\mathbf{A}_{jk} = \frac{e^{ikr_{jk}}}{r_{jk}} \left[k^2 (\hat{r}_{jk} \hat{r}_{jk} - \mathbf{1}_3) + \frac{ikr_{jk} - 1}{r_{jk}^2} (3\hat{r}_{jk} \hat{r}_{jk} - \mathbf{1}_3) \right]. \tag{3.67}$$

By defining the diagonal elements of the interaction matrix as

$$\mathbf{A}_{jj} = \alpha_j^{-1}, \tag{3.68}$$

a system, of $3N$ linear equations can be constructed:

$$\mathbf{E}_{inc,j} = \mathbf{A}_{jj}\mathbf{P}_j + \sum_{k\neq j} \mathbf{A}_{jk}\mathbf{P}_k, \tag{3.69}$$

$$\sum_{k=1}^{N} A_{jk}\mathbf{P}_k = \mathbf{E}_{inc,j}. \tag{3.70}$$

In the original implementation of the method [12] the Clausius Mossotti polarizability [40] was used:

$$\alpha_j^{CM} = \frac{3d^3}{4\pi}\left(\frac{m_j^2-1}{m_j^2+2}\right) = \frac{3d^3}{4\pi}\left(\frac{\epsilon_j-1}{\epsilon_j+2}\right). \tag{3.71}$$

However this polarizability is only valid for inifinite wavelength. Otherwise one has to include a radiative-reaction correction. One polarizability which includes this correction is the so called lattice dispersion polarizability which can be calculated from electromagnetic wave propagation on an infinite lattice [14]:

$$\alpha_j^{LDR} = \frac{\alpha_j^{CM}}{1+\frac{\alpha_j^{CM}}{d^3}\left[(b_1+m^2b_2+m^2b_3S)(kd)^2-\frac{2}{3}i(kd)^3\right]}. \tag{3.72}$$

Here $b_1 = -1.891531$, $b_2 = 0.1648469$, $b_3 = -1.7700004$, and

$$S = \sum_{j=1}^{3}(\hat{a}_j \cdot \hat{e}_j)^2, \tag{3.73}$$

is a function of the propagation direction $\hat{a}$ and polarization $\hat{e}$ of the incident wave.

After solving the system of equations for the dipole moments one can calcuate the

DDA optical cross sections [13] [12]:

$$C_{ext} = \frac{4\pi k}{|\mathbf{E}_0|^2} \sum_{j=0}^{N} \Im m \left(\mathbf{E}^*_{inc,j} \mathbf{P}_j \right), \tag{3.74}$$

$$C_{abs} = \frac{4\pi k}{|\mathbf{E}_0|^2} \sum_{j=0}^{N} \left[\Im m \left(\mathbf{P}_j (\alpha_j^{-1})^* \mathbf{P}_j^* \right) - \frac{2}{3} k^3 \left| \mathbf{P}_j \right|^2 \right], \tag{3.75}$$

$$C_{sca} = C_{ext} - C_{abs}, \tag{3.76}$$

by using the optical theorem.
In the next section we present simulation results done with the MNPBEM Toolbox. We start with a comparison between the boundary element method and Mie theory. Then we compare the simulation method using the full Maxwell equations to the one using the quasistatic approximation. We also compare the boundary element method implementation to the discrete dipole approximation and show electric field maps for a sphere which is illuminated by a plane wave.

Results

Comparison with Mie theory

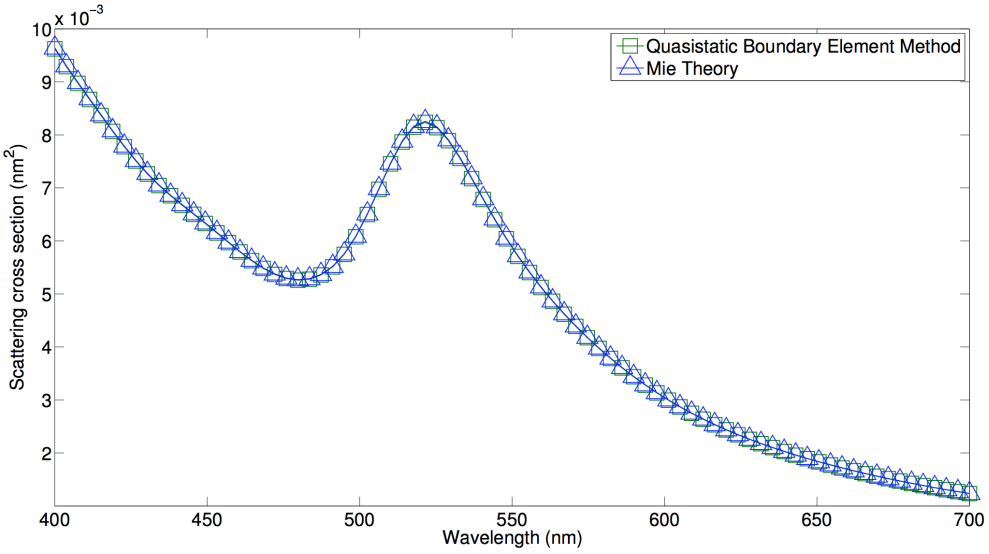

Figure 3.3.: Comparison of scattering cross sections of a gold sphere with a diameter of 10 nm located in free space which is illuminated by a plane wave with z polarization obtained by the quasistatic boundary element method and by Mie theory. For the simulation 144 boundary elements where used.

In Fig. 3.3 we compare simulation results of a scattering cross section of a gold sphere with a diameter of 10 nm located in free space which is illuminated by a plane wave obtained with the quasistatic boundary element method to results obtained with Mie theory. For the surface discretization 144 boundary elements where used.

Comparison with quasistatic simulations

In Fig. 3.4 we present simulation results of a scattering cross section of a gold ellipsoid with a diameter of 10 nm and a height of 20 nm located in free space which

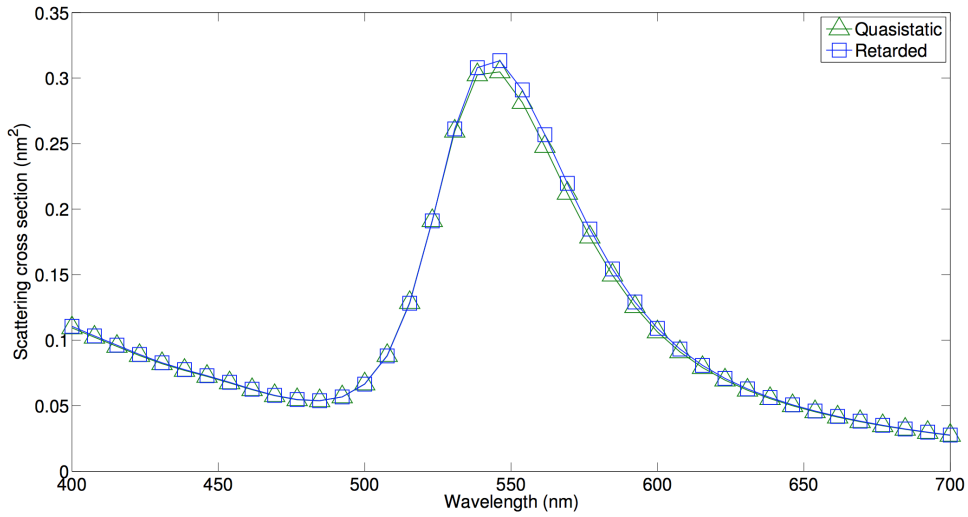

Figure 3.4.: Comparison of scattering cross sections of a gold ellipsoid with a diameter of 10 nm and a height of 20 nm located in free space which is illuminated by a plane wave with z polarization obtained by the quasistatic and retarded boundary element method. For the simulation 2884 boundary elements where used.

is illuminated by a plane wave with z polarization. We compare simulation results of the quasistatic and the retarded boundary element method approach finding good agreement throughout the whole wavelength regime. For the surface discretization 1444 boundary elements where used.

Comparison with discrete dipole approximation simulations

In Fig. 3.5 we present simulation results of a scattering cross section of a gold sphere with a diameter of 50 nm located in free space which is illuminated by a plane wave. We compare simulation results of the boundary element method and the dicrete dipole approximation again finding good agreement throughout the whole wavelength regime. For the boundary element method simulation a surface discretization with 1444 boundary elements was used. For the discrete dipole approximation simulation

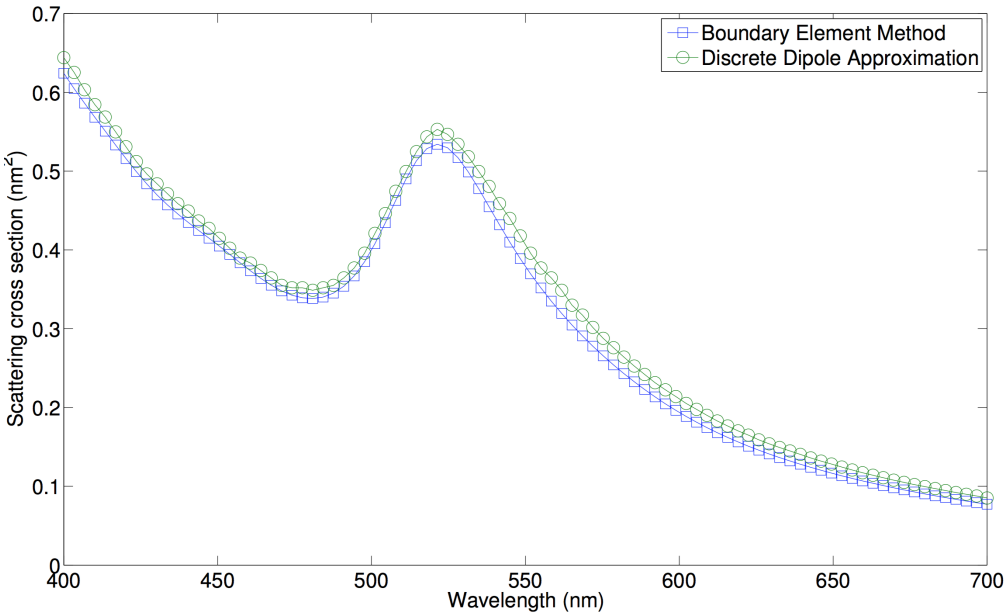

Figure 3.5.: Comparison of scattering cross sections of a gold nanopshere with a diameter of 20 nm located in free space which is illuminated by a plane wave obtained by the boundary element method and the discrete dipole approximation. For the boundary element method simulation a surface discretization with 1444 boundary elements was used. For the discrete dipole approximation simulation a discretization with 33552 point dipoles was used.

a discretization with 33552 point dipoles was used.

Simulation of the electric field enhancement

In Fig. 3.6 we present simulation results of the electric field enhancement of gold sphere with a diameter of 20 nm located in free space which is illuminated by a plane wave. For the simulation of the induced electric field the resonance energy of 523.1 nm was used.

In the next chapter we will show how the boundary element method can be modified

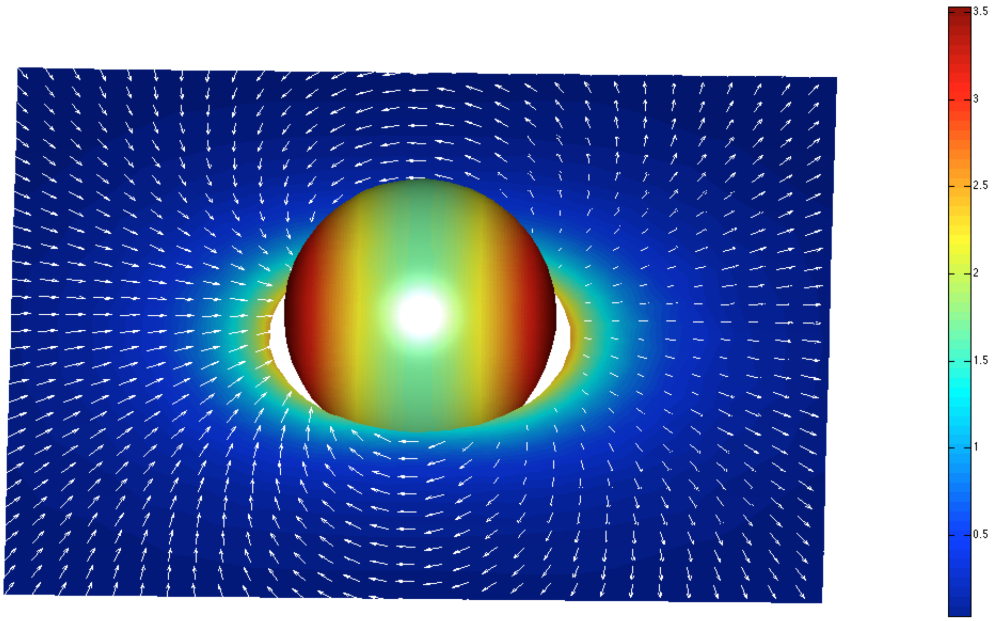

Figure 3.6.: Field enhancement of a gold nanosphere with a diameter of 20 nm located in free space which is illuminated by a plane wave with x-polarization obtained by the boundary element method. For the simulation of the induced electric field the resonance energy of 523.1 nm was used.

to allow simulations for particles situated on substrates and embedded in layerstructures.

4. Simulation of plasmonic nanoparticles situated on substrates

There exist various possible applications [3, 75, 97] which use plasmonic nanoparticles situated on substrates or embedded in layer structures.

It is possible to include substrate effects in finite difference time domain method [8, 22, 82, 96, 98, 99] and finite elements [39, 103] simulations where in most cases the volume of the nanoparticle, parts of the substrate, and the background medium get discretized and perfectly matched layers are used [22]. In the integral methods, which are formulated with the use of Green functions [59], one can instead use special Green functions [27, 71, 93] to describe the presence of an inhomogenous dielectric environment. The calculation of these Green functions usually includes the evaluation of Sommerfeld integrals [9, 16, 20, 52, 59, 61, 62, 64].

Until now no formulation of the potential based boundary element method which includes substrate effects was known [26]. In this main part of the thesis we now present a methodology for boundary element method simulations which also include substrate interactions [93]. We start with deriving the boundary element working equations which include substrate interactions. Then we show how to calculate the additional reflected Green functions. This is a three step process. First one expands the scalar and vector potential originating from the source points in cylindrical waves. In the second step the boundary element method reflection and transmission coefficients are computed by using the boundary conditions of Maxwell's equations and in the last step the potentials at the observation points are computed by integrating over all cylindrical waves.

4.1. Boundary Element Method with surface interaction

For a nanoparticle located in the dielectric environment of a substrate or layerstructure one has to add additional reflected Green functions ($G_2^{\sigma\sigma}$, G_2^{hh}, $G_2^{h\sigma}$, $G_2^{\sigma h}$ and $G_2^{\parallel}$) to account for the fact that the perpendicular surface current $h_2^{\perp}$ and the surface charge σ_2 become coupled through additional interactions. The parallel surface current $h_2^{\parallel}$ does not couple to the perpendicular surface current and the surface charge distribution [93]. This can be seen from the boundary conditions related to the continuity of the tangential magnetic field and to the continuity of the normal electric displacement. For a flat substrate the outer surface vector always points in the same direction, say $n = (0, 0, 1)$, which decouples the equations. By replacing the Green function on the outer boundary with Green functions of the layer structure the solutions which are valid in whole space then look the following way:

$$\phi_1 = G_1\sigma_1 + \phi_1^e, \tag{4.1}$$

$$\phi_2 = G_2^{\sigma\sigma}\sigma_2 + G_2^{\sigma h}h_2^{\perp} + \phi_2^e, \tag{4.2}$$

$$A_1^{\perp} = G_1 h_1^{\perp} + A_1^{e\perp}, \tag{4.3}$$

$$A_2^{\perp} = G_2^{h\sigma}\sigma_2 + G_2^{hh}h_2^{\perp} + A_2^{e\perp}, \tag{4.4}$$

$$\mathbf{A}_1^{\parallel} = G_1\mathbf{h}_1^{\parallel} + \mathbf{A}_1^{e\parallel}, \tag{4.5}$$

$$\mathbf{A}_2^{\parallel} = G_2^{\parallel}\mathbf{h}_2^{\parallel} + \mathbf{A}_2^{e\parallel}. \tag{4.6}$$

Here we have again changed from boundary integrals to boundary elements, use a compact matrix notation, and again calculate the surface charges and currents which

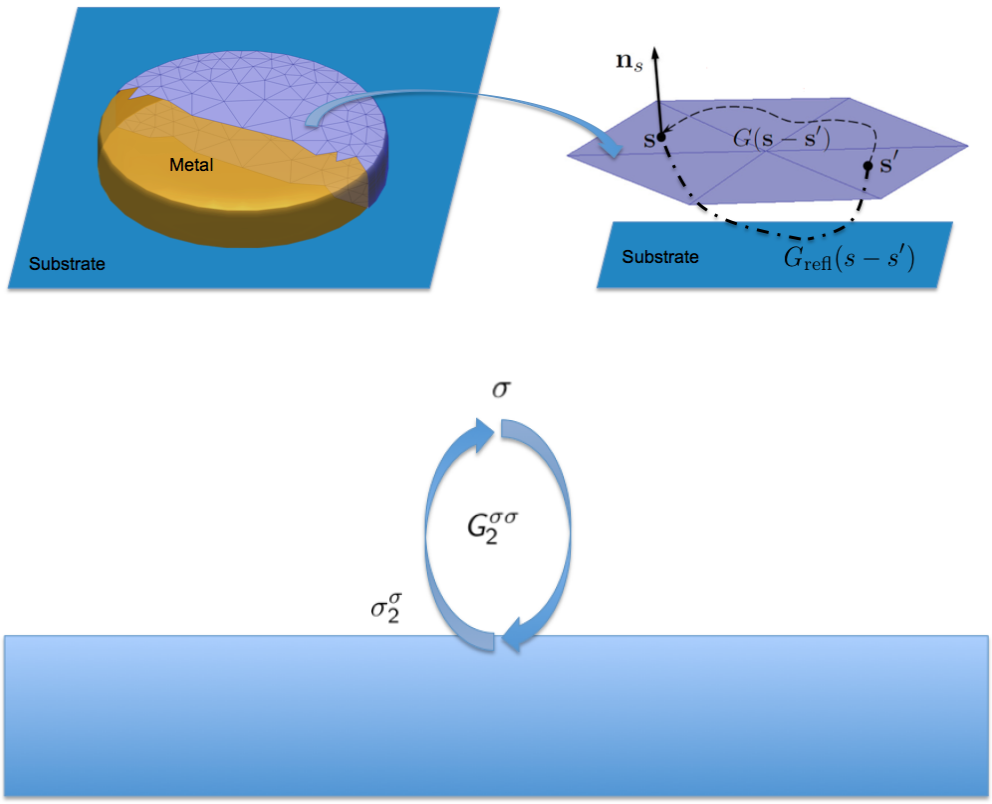

Figure 4.1.: If a particle is placed on a substrate one has to add additional reflected Green functions in the boundary element method to incoporate the substrate interactions [93]. The reflected Green functions ($G_2^{\sigma\sigma}$, G_2^{hh}, $G_2^{h\sigma}$, $G_2^{\sigma h}$ and $G_2^{\parallel}$) are obtained in a three step process [93]. First one expands the scalar and vector potential originating from the source points (locations of σ_2 and h_2 on discretized surface of the nanoparticle) in cylindrical waves. In the second step the boundary element method reflection and transmission coefficients (e.g. σ_2^{σ}) are computed by using the boundary conditions of Maxwell's equations. In the last step the potentials at the observation points (e.g. $G_2^{\sigma\sigma}$) are computed by integrating over all cylindrical waves.

were introduced because of the discountinuity at the boundary with the use of the boundary conditions of Maxwell's theory. The continuity of the tangential electric field leads to the continuity of the scalar potential

$$G_1\sigma_1 = G_2^{\sigma\sigma}\sigma_2 + G_2^{\sigma h}h_2^{\perp} + \varphi, \tag{4.7}$$

with

$$\varphi = \phi_2^e - \phi_1^e. \tag{4.8}$$

The continuity of the normal magnetic induction leads to the continuity of the vector potential

$$G_1\mathbf{h_1}^{\parallel} = G_2^{\parallel}\mathbf{h_2}^{\parallel} + \mathbf{a}^{\parallel}, \tag{4.9}$$

$$G_1 h_1^{\perp} = G_2^{hh}h_2^{\perp} + G_2^{h\sigma}\sigma_2 + a^{\perp}, \tag{4.10}$$

with

$$\mathbf{a} = \mathbf{A_2^e} - \mathbf{A_1^e}. \tag{4.11}$$

The continuity of the tangential magnetic field translates to

$$H_1\mathbf{h_1}^{\parallel} - H_2^{\parallel}\mathbf{h_2}^{\parallel} - ik\hat{\mathbf{n}}^{\parallel}(\epsilon_1 G_1\sigma_1 - \epsilon_2 G_2^{\sigma\sigma}\sigma_2 - \epsilon_2 G_2^{\sigma h}h_2^{\perp}) = \alpha^{\parallel}, \tag{4.12}$$

$$H_1 h_1^{\perp} - H_2^{hh}h_2^{\perp} - H_2^{h\sigma}\sigma_2 - ik\hat{n}^{\perp}(\epsilon_1 G_1\sigma_1 - \epsilon_2 G_2^{\sigma\sigma}\sigma_2 - \epsilon_2 G_2^{\sigma h}h_2^{\perp}) = \alpha^{\perp}, \tag{4.13}$$

and from the continuity of the normal electric displacement one obtains

$$\begin{aligned}\epsilon_1 H_1\sigma_1 - \epsilon_2 H_2^{\sigma\sigma}\sigma_2 - \epsilon_2 H_2^{\sigma h}h_2^{\perp} - ik\hat{\mathbf{n}}^{\parallel}\cdot(\epsilon_1 G_1\mathbf{h_1}^{\parallel} - \epsilon_2 G_2^{\parallel}\mathbf{h_2}^{\parallel}) - \\ ikn^{\perp}(\epsilon_1 G_1 h_1^{\perp} - \epsilon_2 G_2^{hh}h_2^{\perp} - \epsilon_2 G_2^{h\sigma}\sigma_2) = D^e.\end{aligned} \tag{4.14}$$

To obtain the boundary element method working equations one first expresses $\mathbf{h}_2^{\parallel}$ in terms of $h_2^{\perp}$ and σ_2

$$(\Sigma_1 - \Sigma_2^{\parallel})G_2^{\parallel}\mathbf{h}_2^{\parallel} = ik\hat{\mathbf{n}}^{\parallel}(\epsilon_2 - \epsilon_1)(G_2^{\sigma\sigma}\sigma_2 + G_2^{\sigma h}h_2^{\perp}) + \boldsymbol{\alpha}^{\parallel} - \Sigma_1\mathbf{a}^{\parallel} + ik\hat{\mathbf{n}}^{\parallel}\epsilon_1\varphi, \tag{4.15}$$

with

$$\Sigma = HG^{-1}. \tag{4.16}$$

Then the fourth and the last term of the equation related to the boundary condition of the electric displacement can be rewritten as

$$ik\hat{\mathbf{n}}^{\parallel} \cdot (\epsilon_1 G_1 \mathbf{h}_1^{\parallel} - \epsilon_2 G_2^{\parallel} \mathbf{h}_2^{\parallel}) = \hat{\mathbf{n}}^{\parallel} \cdot \Gamma[ik\hat{\mathbf{n}}^{\parallel}(\epsilon_1 - \epsilon_2)(G_2^{\sigma\sigma}\sigma_2 + G_2^{\sigma h} h_2^{\perp}) + \tilde{\alpha}^{\parallel}] + ik\hat{\mathbf{n}}^{\parallel} \cdot \epsilon_1 \mathbf{a}^{\parallel}, \tag{4.17}$$

$$\begin{aligned} ik\hat{n}^{\perp}[\epsilon_1(G_2^{h\sigma}\sigma_2 + G_2^{hh}h_2^{\perp} + a^{\perp}) - \epsilon_2(G_2^{h\sigma}\sigma_2 + G_2^{hh}h_2^{\perp})] = \\ ik\hat{n}^{\perp}(\epsilon_1 - \epsilon_2)(G_2^{h\sigma}\sigma_2 + G_2^{hh}h_2^{\perp}) + ik\hat{n}^{\perp}a^{\perp}, \end{aligned} \tag{4.18}$$

where

$$\Gamma = ik(\epsilon_1 - \epsilon_2)(\Sigma_1 - \Sigma_2^{\parallel})^{-1}, \tag{4.19}$$

and

$$\tilde{\alpha} = \alpha - \Sigma_1 \mathbf{a} + ik\hat{\mathbf{n}}\epsilon\varphi, \tag{4.20}$$

was used. Hence

$$\begin{aligned} \epsilon_1\Sigma_1(G_2^{\sigma\sigma}\sigma_2 + G_2^{\sigma h}h_2^{\perp} + \varphi) - \epsilon_2 H_2^{\sigma\sigma}\sigma_2 - \epsilon_2 H_2^{\sigma h}h_2^{\perp} - \\ ik\hat{\mathbf{n}}^{\parallel} \cdot \Gamma\hat{\mathbf{n}}^{\parallel}(\epsilon_1 - \epsilon_2)(G_2^{\sigma\sigma}\sigma_2 + G_2^{\sigma h}h_2^{\perp}) - ikn^{\perp}(\epsilon_1 - \epsilon_2)(G_2^{h\sigma}\sigma_2 + G_2^{hh}h_2^{\perp}) = \\ D^e + ik\hat{\mathbf{n}}^{\parallel} \cdot \epsilon_1 \mathbf{a}^{\parallel} + \hat{\mathbf{n}}^{\parallel} \cdot \Gamma\tilde{\alpha} + ik\hat{n}^{\perp}a^{\perp}. \end{aligned} \tag{4.21}$$

Similary by rewriting the perpendicular part of the boundary condition related to the tangential magnetic field we get:

$$\begin{aligned} \Sigma_1(G_2^{h\sigma}\sigma_2 + G_2^{hh}h_2^{\perp} + a^{\perp}) - H_2^{hh}h_2^{\perp} - H_2^{h\sigma}\sigma_2 - \\ ik\hat{n}^{\perp}[\epsilon_1(G_2^{\sigma\sigma}\sigma_2 + G_2^{\sigma h}h_2^{\perp} + \varphi) - \epsilon_2(G_2^{\sigma\sigma}\sigma_2 + G_2^{\sigma h}h_2^{\perp})] = \alpha^{\perp}. \end{aligned} \tag{4.22}$$

These leads to the following two

boundary element method working equations with layer structure

$$\begin{aligned}(\epsilon_1\Sigma_1 G_2^{\sigma\sigma} - \epsilon_2 H_2^{\sigma\sigma})\sigma_2 + (\epsilon_1\Sigma_1 G_2^{\sigma h} - \epsilon_2 H_2^{\sigma h} h_2^{\perp}) - \\ ik\hat{\mathbf{n}}^{\parallel}\cdot\Gamma\hat{\mathbf{n}}^{\parallel}(\epsilon_1-\epsilon_2)(G_2^{\sigma\sigma}\sigma_2 + G_2^{\sigma h}h_2^{\perp}) - ik\hat{n}(\epsilon_1-\epsilon_2)(G_2^{h\sigma}\sigma_2 + G_2^{hh}h_2^{\perp}) = \\ D^e - \epsilon_1\Sigma_1\varphi + ik\hat{\mathbf{n}}\cdot\epsilon_1\mathbf{a} + \hat{\mathbf{n}}^{\parallel}\cdot\Gamma(\alpha^{\parallel} - \Sigma_1\mathbf{a}^{\parallel} + ik\hat{\mathbf{n}}^{\parallel}\epsilon_1\varphi),\end{aligned} \tag{4.23}$$

$$\begin{aligned}(\Sigma_1 G_2^{h\sigma} - H_2^{h\sigma})\sigma_2 + (\Sigma_1 G_2^{hh} - H_2^{hh})h_2^{\perp} - \\ ikn^{\perp}(\epsilon_1-\epsilon_2)(G_2^{\sigma\sigma}\sigma_2 + G_2^{\sigma h}h_2^{\perp}) = \alpha^{\perp} - \Sigma_1 a^{\perp} + ik\hat{n}^{\perp}\epsilon_1\varphi,\end{aligned} \tag{4.24}$$

which can be solved through matrix inversion.

The reflected Green functions ($G^{\sigma\sigma}$, G^{hh}, $G^{h\sigma}$, $G^{\sigma h}$ and $G^{\parallel}$) are obtained in a three step process [93]. First one expands the scalar and vector potential originating from the source points in cylindrical waves. In this step we employ the

Sommerfeld identity [10]

$$\frac{e^{(ikr)}}{r} = i\int_0^{\infty}\frac{k_\rho}{k_z}e^{(ik_z|z|)}J_0(k_\rho\rho)dk_\rho, \tag{4.25}$$

where $J_0(k_\rho\rho)$ is the zeroth-order Bessel function (see Appendix A.7).

In the second step the boundary element method reflection and transmission coefficients are computed by using the boundary conditions of Maxwell's equations and the

plane wave Green function (see Appendix A.8)

$$g(k) = \frac{2\pi i}{k_z} e^{ik_z z}. \tag{4.26}$$

For a tranversal excitation

$$\mathbf{A}_2^e = g\mathbf{x}, \tag{4.27}$$

the parallel surface current $h_2^{\parallel}$ does not couple to the perpendicular surface current and the surface charge. The continuity of the normal magnetic induction

$$G_1 h_1 - G_2 h_2 = 2\pi i \left(\frac{h_1}{k_{1z}} - \frac{h_2}{k_{2z}} \right) = A_2^e = g, \tag{4.28}$$

and the continuity of the tangential magnetic field

$$H_1 h_1 - H_2 h_2 = 2\pi (h_1 + h_2) = -ik_{2z} g, \tag{4.29}$$

can be used to obtain the parallel surface currents through matrix inversion:

$$h_2 = \frac{k_{2z} - k_{1z}}{k_{2z} + k_{1z}} \frac{k_{2z} g}{2\pi i}, \tag{4.30}$$

$$h_1 = \frac{2k_{1z}}{k_{2z} + k_{1z}} \frac{k_{2z} g}{2\pi i}. \tag{4.31}$$

For perpendicular or surface charge excitation we use the continuity of the tangential electric field and the continuity of the normal magnetic induction which imply that

$$G_1 \sigma_1 - G_2 \sigma_2 = \varphi, \tag{4.32}$$

$$G_1 h_1 - G_2 h_2 = a, \tag{4.33}$$

have to be fulfilled. Further the continuity of the tangential magnetic field

$$2\pi(h_1 + h_2) - ik_0(G_1\epsilon_1\sigma_1 - G_2\epsilon_2\sigma_2) = \alpha, \tag{4.34}$$

and the normal electric displacement

$$2\pi(\epsilon_1\sigma_1 + \epsilon_2\sigma_2) - ik_0(G_1\epsilon_1 h_1 - G_2\epsilon_2 h_2) = D^e, \tag{4.35}$$

with

$$\alpha = a' - ik_0\epsilon_2\phi, \tag{4.36}$$

$$D^e = -\epsilon_2(ik_0 a - \phi'), \tag{4.37}$$

are used to obtain the surface currents and charges at the substrate boundary. Because of the continuity of the tangential electric field and the continuity of the normal magnetic induction the surface charges and currents on both sides can be related:

$$\sigma_1 = G_1^{-1}(G_2\sigma_2 + \varphi) = \frac{k_{1z}}{k_{2z}}\sigma_2 + G_1^{-1}\varphi, \tag{4.38}$$

$$h_1 = G_1^{-1}(G_2 h_2 + a) = \frac{k_{1z}}{k_{2z}}h_2 + G_1^{-1}a. \tag{4.39}$$

Inserting these relations into the remaining boundary conditions yields

$$2\pi\left(\epsilon_1\frac{k_{1z}}{k_{2z}} + \epsilon_2\right)\sigma_2 - ik_0\left(\epsilon_1 - \epsilon_2\right)G_2 h_2 = D^e - 2\pi\epsilon_1 G_1^{-1}\varphi + ik_0\epsilon_1 a, \tag{4.40}$$

$$2\pi\left(\frac{k_{1z}}{k_{2z}} + 1\right)h_2 - ik_0\left(\epsilon_1 - \epsilon_2\right)G_2\sigma_2 = \alpha - 2\pi G_1^{-1}a + ik_0\epsilon_1\varphi. \tag{4.41}$$

This leads to the following equations at the substrate boundary

$$\left(\epsilon_1\frac{k_{1z}}{k_{2z}} + \epsilon_2\right)\sigma_2 + \frac{k_0}{k_{2z}}(\epsilon_1 - \epsilon_2)h_2 = \frac{\tilde{D}_e}{2\pi}, \tag{4.42}$$

$$\left(\frac{k_{1z}}{k_{2z}} + 1\right)h_2 + \frac{k_0}{k_{2z}}(\epsilon_1 - \epsilon_2)\sigma_2 = \frac{\tilde{\alpha}}{2\pi}. \tag{4.43}$$

They can again be solved through matrix inversion. Therefore we first multiply both sides with k_{2z}

$$(\epsilon_1 k_{1z} + \epsilon_2 k_{2z})\sigma_2 + k_0(\epsilon_1 - \epsilon_2)h_2 = \frac{k_{2z}\tilde{D}_e}{2\pi}, \tag{4.44}$$

$$(k_{1z} + k_{2z})h_2 + k_0(\epsilon_1 - \epsilon_2)\sigma_2 = \frac{k_{2z}\tilde{\alpha}}{2\pi}, \tag{4.45}$$

and calculate the determinant

$$\Delta = (k_{1z} + k_{2z})(\epsilon_1 k_{1z} + \epsilon_2 k_{2z}) - k_0^2(\epsilon_1 - \epsilon_2)^2, \tag{4.46}$$

$$k_0^2(\epsilon_1 - \epsilon_2)^2 = (\epsilon_1 - \epsilon_2)(k_1^2 - k_2^2) = (\epsilon_1 - \epsilon_2)(k_{1z}^2 - k_{2z}^2), \tag{4.47}$$

$$\Delta = (k_{1z} + k_{2z})(\epsilon_2 k_{1z} + \epsilon_1 k_{2z}). \tag{4.48}$$

The surface charge and current on the upper side of the substrate are found as

$$\sigma_2 = \frac{k_{2z}}{2\pi\Delta}\left[(k_{1z} + k_{2z})\tilde{D}_e - (\epsilon_1 - \epsilon_2)k_0\tilde{\alpha}\right], \tag{4.49}$$

$$h_2 = \frac{k_{2z}}{2\pi\Delta}\left[-(\epsilon_1 - \epsilon_2)k_0\tilde{D}_e + (\epsilon_1 k_{1z} + \epsilon_2 k_{2z})\tilde{\alpha}\right]. \tag{4.50}$$

If no perpendicular excitation is present the excitation is described by

$$\tilde{D}_e = \left[\epsilon_2(-ik_{2z}) + \epsilon_1 k_{1z}\right] g = i(\epsilon_1 k_{1z} - \epsilon_2 k_{2z})g, \tag{4.51}$$

$$\tilde{\alpha} = \left[-ik_0\epsilon_2 + ik_0\epsilon_1\right] g = ik_0(\epsilon_1 - \epsilon_2)g, \tag{4.52}$$

which leads to

$$\sigma_2 = \frac{ik_{2z}}{2\pi\Delta} g\left[(k_{1z} + k_{2z})(\epsilon_1 k_{1z} - \epsilon_2 k_2) - (\epsilon_1 - \epsilon_2)^2 k_0^2\right], \tag{4.53}$$

$$h_2 = \frac{ik_{2z}}{2\pi\Delta} g\left[k_0(\epsilon_1 - \epsilon_2)(\epsilon_1 k_{1z} + \epsilon_2 k_{2z}) - k_0(\epsilon_1 - \epsilon_2)(\epsilon_1 k_{1z} - \epsilon_2 k_{2z})\right]. \tag{4.54}$$

This can be rewritten to

$$\sigma_2^{\sigma} = \frac{ik_{2z}}{2\pi\Delta}(k_{1z} + k_{2z})(\epsilon_2 k_{1z} + \epsilon_1 k_{2z} - 2\epsilon_2 k_{2z})g, \tag{4.55}$$

$$h_2^{\sigma} = \frac{ik_{2z}}{2\pi\Delta} 2k_0(\epsilon_1 - \epsilon_2)\epsilon_2 k_{2z} g. \tag{4.56}$$

If only a perpendicular excitation is present the excitation is described by

$$\tilde{D}_e = \left[-ik_0\epsilon_2 + ik_0\epsilon_1\right] g = ik_0(\epsilon_1 - \epsilon_2)g, \tag{4.57}$$

$$\tilde{\alpha} = \left[(-ik_{2z}) + ik_{1z}\right] g = i(k_{1z} - k_{2z})g, \tag{4.58}$$

which leads to

$$\sigma_2 = \frac{ik_{2z}}{2\pi\Delta} g \left[k_0(\epsilon_1 - \epsilon_2)(k_{1z} + k_{2z}) - k_0(\epsilon_1 - \epsilon_2)(k_{1z} - k_{2z})\right], \tag{4.59}$$

$$h_2 = \frac{ik_{2z}}{2\pi\Delta} g \left[(k_{1z} - k_{2z})(\epsilon_1 k_{1z} + \epsilon_2 k_{2z}) - k_0^2(\epsilon_1 - \epsilon_2)^2\right]. \tag{4.60}$$

This can also be rewritten to

$$\sigma_2^{h} = \frac{ik_{2z}}{2\pi\Delta} 2k_0(\epsilon_1 - \epsilon_2)k_{2z} g, \tag{4.61}$$

$$h_2^{h} = \frac{ik_{2z}}{2\pi\Delta}(k_{1z} - k_{2z})(\epsilon_2 k_{1z} - \epsilon_1 k_{2z} + 2\epsilon_2 k_{2z})g. \tag{4.62}$$

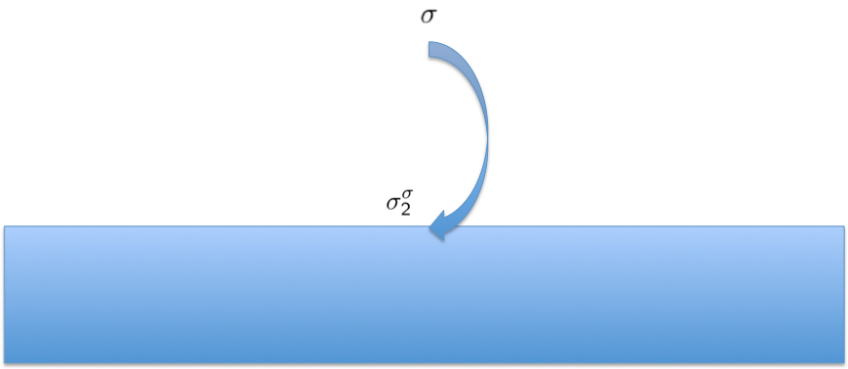

Figure 4.2.: The surface charges and surface currents on the outer side of the metallic nanoparticle lead to scalar and vector potentials acting on the substrate. The surface charges and surface currents at the substrate (e.g σ_2^σ) are obtained from the boundary conditions [93]. They describe the reflections and transmissions and are used to calculate the reflected Green functions.

To summerize we found the following

boundary element method reflection coefficients at the substrate:

$$\sigma_2^\sigma = \frac{ik_{2z}}{2\pi\Delta}(k_{1z}+k_{2z})(\epsilon_2 k_{1z}+\epsilon_1 k_{2z}-2\epsilon_2 k_{2z})g, \tag{4.63}$$

$$h_2^\sigma = \frac{ik_{2z}}{2\pi\Delta}2k_0(\epsilon_1-\epsilon_2)\epsilon_2 k_{2z}g, \tag{4.64}$$

$$\sigma_2^h = \frac{ik_{2z}}{2\pi\Delta}2k_0(\epsilon_1-\epsilon_2)k_{2z}g, \tag{4.65}$$

$$h_2^h = \frac{ik_{2z}}{2\pi\Delta}(k_{1z}-k_{2z})(\epsilon_2 k_{1z}-\epsilon_1 k_{2z}+2\epsilon_2 k_{2z})g, \tag{4.66}$$

with

$$\Delta = (k_{1z}+k_{2z})(\epsilon_2 k_{1z}+\epsilon_1 k_{2z}). \tag{4.67}$$

To generalize for the boundary element method reflection and transmission coefficients for layer structures one additionaly introduces an interlayer Green function G^μ [26] [93] and again treats parallel and perpendicular or surface charge excitation separatly. For parallel excitation we find the following boundary conditions:

$$G_0^{\mu+1}\mathbf{h}_1^{\mu+1} - G_0^{\mu}\mathbf{h}_2^{\mu} - G^{\mu}\mathbf{h}_1^{\mu} + G^{\mu+1}\mathbf{h}_2^{\mu+1} = \mathbf{A}_2^{\mu} - \mathbf{A}_1^{\mu+1}, \tag{4.68}$$

$$2\pi i(\mathbf{h}_1^{\mu+1} + \mathbf{h}_2^{\mu}) - k_z^{\mu}G^{\mu}\mathbf{h}_1^{\mu} - k_z^{\mu+1}G^{\mu+1}\mathbf{h}_2^{\mu+1} = k_z^{\mu}\mathbf{A}_2^{\mu} - k_z^{\mu+1}\mathbf{A}_1^{\mu+1}. \tag{4.69}$$

In the case of a perpendicular excitation or the excitation through a potential of a surface charge we find the following boundary conditions:

$$G_0^{\mu+1}\sigma_1^{\mu+1} - G_0^{\mu}\sigma_2^{\mu} - G^{\mu}\sigma_1^{\mu} + G^{\mu+1}\sigma_2^{\mu+1} = \phi_2^{\mu} - \phi_1^{\mu+1}, \tag{4.70}$$

$$G_0^{\mu+1}h_1^{\mu+1} - G_0^{\mu}h_2^{\mu} - G^{\mu}h_1^{\mu} + G^{\mu+1}h_2^{\mu+1} = A_2^{\mu} - A_1^{\mu+1}, \tag{4.71}$$

$$\begin{aligned} 2\pi i(\epsilon_{\mu+1}\sigma_1^{\mu+1} + \epsilon_{\mu}\sigma_2^{\mu}) + k(G_0^{\mu+1}\epsilon_{\mu+1}h_1^{\mu+1} - G_0^{\mu}\epsilon_{\mu}h_2^{\mu}) - \\ k_z^{\mu}\epsilon_{\mu}G^{\mu}\sigma_1^{\mu} - k_z^{\mu+1}\epsilon_{\mu+1}G^{\mu+1}\sigma_2^{\mu+1} - k\epsilon_{\mu}G^{\mu}h_1^{\mu} + k\epsilon_{\mu+1}G^{\mu+1}h_2^{\mu+1} = \\ k_z^{\mu}\epsilon_{\mu}\phi_2^{\mu} + k_z^{\mu+1}\epsilon_{\mu+1}\phi_1^{\mu+1} + k\epsilon_{\mu}A_2^{\mu} - k\epsilon_{\mu+1}A_1^{\mu+1}, \end{aligned} \tag{4.72}$$

$$\begin{aligned} 2\pi i(h_1^{\mu+1} + h_2^{\mu}) + k(G_0^{\mu+1}\epsilon_{\mu+1}\sigma_1^{\mu+1} - G_0^{\mu}\epsilon_{\mu}\sigma_2^{\mu}) - k_z^{\mu}\epsilon_{\mu}G^{\mu}h_1^{\mu} - \\ k_z^{\mu+1}\epsilon_{\mu+1}G^{\mu+1}h_2^{\mu+1} - k\epsilon_{\mu}G^{\mu}\sigma_1^{\mu} + k\epsilon_{\mu+1}G^{\mu+1}\sigma_2^{\mu+1} = \\ k_z^{\mu}A_2^{\mu} + k_z^{\mu+1}A_1^{\mu+1} + k\epsilon_{\mu}\phi_2^{\mu} - k\epsilon_{\mu+1}\phi_1^{\mu+1}. \end{aligned} \tag{4.73}$$

These equations can then be used to compute the reflected Green functions for layer structures.

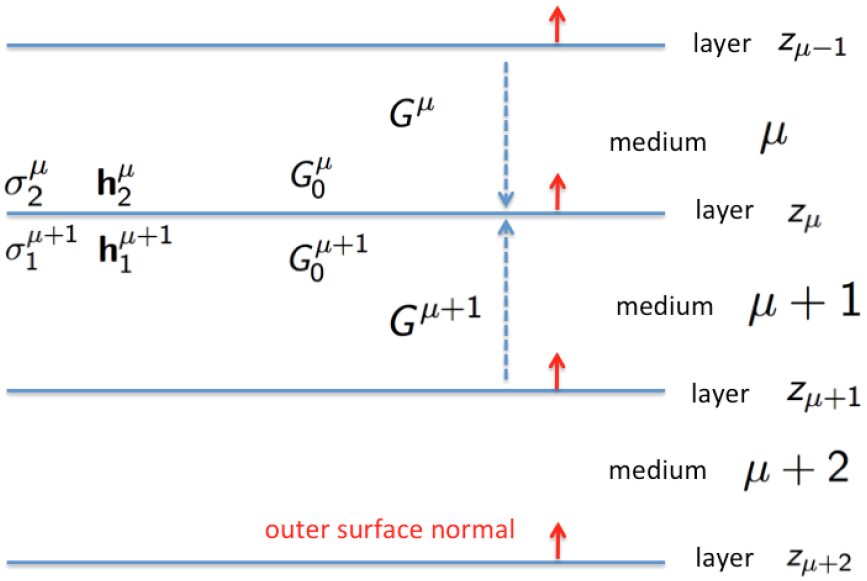

Figure 4.3.: Schematic representation of a layer structure. Here G_0^{μ} is an intralayer Green function that connects points in layer z_{μ} in medium μ and G^{μ} is an interlayer Green function that connects points between different layers (located at z_{μ} and $z_{\mu-1}$) in medium μ [93].

In the last step the potentials at the observation points are computed by integrating over all cylindrical waves [93]:

$$I = i \int_0^{\infty} \frac{k_\rho}{k_z} e^{(ik_z(z+z'))} J_0(k_\rho r) f(k_\rho, k_z) dk_\rho. \tag{4.74}$$

Here $f(k_\rho, k_z)$ are the boundary element method reflection and transmission coefficients. These Sommerfeld integrals have singularities [10] so we deflect the integration

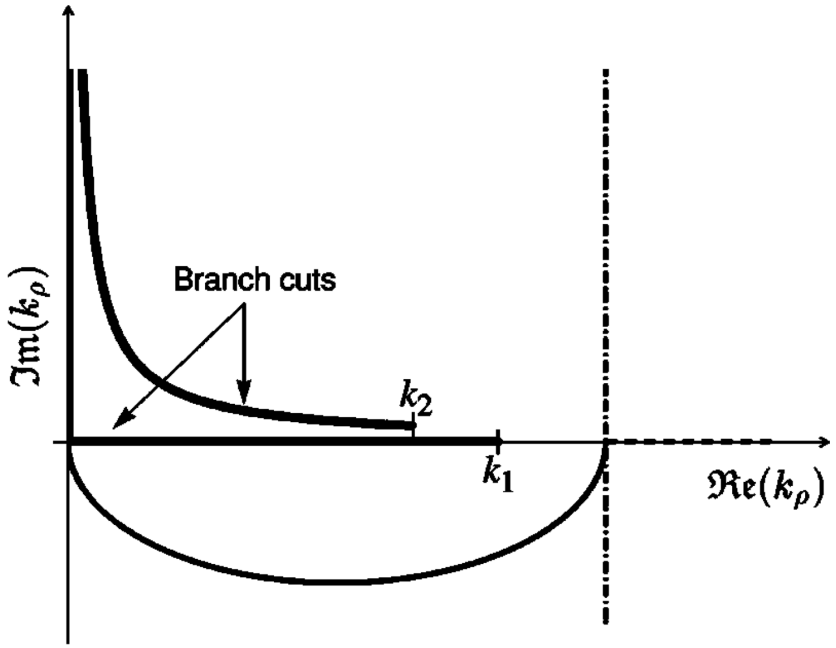

Figure 4.4.: Deflection of the integration path in the complex plane to surround the singularites [10] in an elliptical path with a major semiaxis of $k_\rho^{maj} = \frac{1}{2}(k_l^{max} + k_0)$ and a minor semiaxis of $k_\rho^{min} = 10^{-2} k_\rho^{maj}$. For small $z + z'$ values the exponential damping of the highly oscillatory integral becomes weak. In this case it is better to use Hankel functions with an other asymptotic behavior, and resume the integration along the imaginary axis (dash-dotted line) to get a better convergence of the integration. (Figure taken from [71].)

path in the complex plane to surround them in an elliptical path with a major semiaxis of $k_\rho^{maj} = \frac{1}{2}(k_l^{max} + k_0)$ and a minor semiaxis of $k_\rho^{min} = 10^{-2} k_\rho^{maj}$ and then resume the integration along the real axis using the asymptotic form of the Bessel function which is found from an asymptotic analysis from its integral respresentation [71]:

$$J_0(k_\rho \rho) \approx \sqrt{\frac{2}{\pi k_\rho \rho}} \cos\left(k_\rho \rho - \frac{\pi}{4}\right). \tag{4.75}$$

There are two types of singularities present. Branch point singularities related to the double valued behavior of the integrands and corresponding to radiation modes

and pole singularities related to the vanishing denominators of the integrands corresponding to guided modes [10]. For small $z + z'$ values the exponential damping of the highly oscillatory integral becomes weak. In this case it is better to use Hankel functions with an other asymptotic behavior and resume the integration along the imaginary axis to get a better convergence of the integration [71]:

$$J_n(k_\rho\rho) = \frac{1}{2}\left[H_n^{(1)}(k_\rho\rho) + H_n^{(2)}(k_\rho\rho)\right], \tag{4.76}$$

$$H_\alpha^{(1)}(k_\rho\rho) \approx \sqrt{\frac{2}{\pi k_\rho\rho}} e^{(i(k_\rho\rho - \frac{\alpha\pi}{2} - \frac{\pi}{4}))}, \tag{4.77}$$

$$H_\alpha^{(2)}(k_\rho\rho) \approx \sqrt{\frac{2}{\pi k_\rho\rho}} e^{(-i(k_\rho\rho - \frac{\alpha\pi}{2} - \frac{\pi}{4}))}. \tag{4.78}$$

Because the calculation of the reflected Green functions is computationally very demanding it is done in a two step process. First one sets up a suitable grid of Green function values and then in the second step performes an interpolation. For the interpolation the following functional dependence is assumed [93]:

$$G(r, z_1, z_2) = \frac{g(r, z_1, z_2)}{\tilde{r}}, \tag{4.79}$$

$$F_r(r, z_1, z_2) = -\frac{f_r(r, z_1, r_2)r}{\tilde{r}^3}, \tag{4.80}$$

$$F_z(r, z_1, z_2) = -\frac{f_z(r, z_1, z_2)\tilde{z}}{\tilde{r}^3}, \tag{4.81}$$

with

$$\tilde{r} = \sqrt{r^2 + \tilde{z}^2}, \qquad \tilde{z} = z_1 + z_2. \tag{4.82}$$

Here r is the radial distance and z_1 and z_2 are the z-values of the observation and the source point. This shape is similar to the shape of the quasistatic Green function [40] and therefore there should be only a weak spatial dependence in g, f_r and f_z.

It is also important to be careful about the singular contribution by evaluating the reflected Green functions. Therefore the boundary elements of the particle should be slightly above (or below) the substrate boundary. The surface derivative is split in two parts [93]:

$$F_z(r, z_1, z_2) = -f_0 \frac{\tilde{z}}{\tilde{r}^3} - (f_z(r, z_1, z_2) - f_0) \frac{\tilde{z}}{\tilde{r}^3}, \tag{4.83}$$

with

$$f_0 = \lim_{r,\tilde{z}\to 0} f(r, \tilde{z}). \tag{4.84}$$

The first term gives a singular contribution but the second term has a smooth r and $\tilde{z}$ dependence.

To calculate the optical cross sections we use the stationary phase approximation (see Appendix A.9) [10] to obtain the leading-order approximations for the highly oscillatory integrals:

$$I = \frac{i}{2} \int_{-\infty}^{\infty} e^{(ik_z(z+z'))} \frac{k_\rho}{k_z} H_0^{(1)}(k_\rho r) f(k_\rho, k_z) dk_\rho. \tag{4.85}$$

First we use the asymptotic form of the Hankel function

$$H_0^1(k_\rho r) e^{ik_z(z+z')} \approx \sqrt{\frac{2}{\pi k_\rho \rho}} e^{i(k_\rho \rho + k_z z - k_\rho \rho \dot{\rho}' + k_z z' - \frac{\pi}{4})}, \tag{4.86}$$

where also

$$r \approx \rho - \hat{\rho} \cdot \rho' \tag{4.87}$$

was used, and find the point of least oscillation with

$$\frac{d}{dk_\rho} \left(k_\rho \rho + \sqrt{k^2 - k_\rho^2} z \right) = 0. \tag{4.88}$$

This leads to

$$k_{\rho s} = k \frac{\rho}{r}, \tag{4.89}$$

$$k_{zs} = k\frac{z}{r}, \tag{4.90}$$

and we obtain

the stationary phase point

$$\mathbf{k}_s = k\mathbf{r}, \tag{4.91}$$

from which we can approximate our integrals as

$$I = \frac{e^{ikr}}{r} e^{-i\mathbf{k}'\cdot\mathbf{r}'} f(k\mathbf{r}). \tag{4.92}$$

By inserting the reflected Green functions in the boundary element method working equations with layer structure we can calculate the surface charges and surface currents at the boundary of the particle and by using the asymptotic forms the electromagnetic fields and the spectra can be computed. For the extinction a generalized optical theorem is used [55].

It is also possible to account for a substrate in the quasistatic approach [93]. In this case one uses an additional image Green function to describe the substrate interaction:

$$\sigma = (\epsilon_1 H_1 - \epsilon_2 H_2)^{-1}(\epsilon_1 - \epsilon_2)\frac{\partial \phi^e}{\partial n}. \tag{4.93}$$

4.2. Discrete Dipole Approximation with surface interaction

In this section we follow [52] to derive a modification of the discrete dipole approximation which includes surface interactions. In this modification the incident field is a sum of direct and reflected waves and the interaction matrix $\mathbf{A}_{jk}^{SI}$ in

$$\sum_{k=1}^{N} \mathbf{A}_{jk}^{SI} \mathbf{P}_k = \mathbf{E}_{inc,j}, \tag{4.94}$$

additionally has to include a reflection matrix R_{jk} [52,53,66,80,81]. To derive [52] [53] this reflection matrix, which describes the interactions with the image dipoles, we start with the known Sommerfeld identities

$$\frac{e^{ikr}}{4\pi r} = \frac{i}{4\pi} \int_0^\infty \frac{k_\rho}{k_z} J_0(k_\rho \rho) e^{ik_z|z|} dk_\rho, \tag{4.95}$$

$$\frac{e^{ikr}}{4\pi r} = \frac{i}{8\pi} \int_{-\infty}^\infty \frac{k_\rho}{k_z} H_0^{(1)}(k_\rho \rho) e^{ik_z|z|} dk_\rho, \tag{4.96}$$

and introduce the Fresnel coefficients (see Appendix A.2) for the planar components [10] [40]:

$$R^{TE} = \frac{\mu_r k_{2z} - k_{1z}}{\mu_r k_{2z} + k_{1z}} e^{ik_{2z} z_k}. \tag{4.97}$$

$$R^{TM} = \frac{\epsilon_r k_{2z} - k_{1z}}{\epsilon_r k_{2z} + k_{1z}} e^{ik_{2z} z_k}. \tag{4.98}$$

Here also the phase shift due to the propagation in the z direction was included. Then the reflected dipole fields become

$$\left(\frac{e^{ikr}}{4\pi r}\right)_{TE}^{I} = \frac{i}{4\pi} \int_0^\infty \frac{k_{2\rho}}{k_{2z}} J_0(k_{2\rho}\rho) \frac{\mu_r k_{2z} - k_{1z}}{\mu_r k_{2z} + k_{1z}} e^{ik_{2z}(z_j + z_k)} dk_\rho, \tag{4.99}$$

$$\left(\frac{e^{ikr}}{4\pi r}\right)_{TM}^{I} = \frac{i}{4\pi} \int_0^\infty \frac{k_{2\rho}}{k_{2z}} J_0(k_{2\rho}\rho) \frac{\epsilon_r k_{2z} - k_{1z}}{\epsilon_r k_{2z} + k_{1z}} e^{ik_{2z}(z_j + z_k)} dk_\rho, \tag{4.100}$$

Such integrals can also be written [5] [87] by using the substitutions $\gamma_1 = (\lambda^2 - k_1^2)^{1/2} \to -ik_1$ (for $\lambda \to 0$), $\gamma_2 = (\lambda^2 - k_2^2)^{1/2} \to -ik_2$ (for $\lambda \to 0$), $\epsilon_r = k_1^2/k_2^2$ and $k_\rho^2 = k - k_z^2$:

$$\left(\frac{e^{ikr}}{4\pi r}\right)^I_{TM} = \frac{1}{4\pi}\int_0^\infty \left[\frac{-1}{\gamma_2} J_0(\lambda\rho) e^{-\gamma_2(z_j+z_k)} + \frac{2k_1^2}{k_1^2\gamma_2 + k_2^2\gamma_1} J_0(\lambda\rho) e^{-\gamma_2(z_j+z_k)}\right] \lambda d\lambda, \tag{4.101}$$

which can be simplified to

$$\left(\frac{e^{ikr}}{4\pi r}\right)^I_{TM} = -\frac{e^{ikr}}{4\pi r_I} + \frac{k_1^2}{2\pi}\int_0^\infty \left[\frac{1}{k_1^2\gamma_2 + k_2^2\gamma_1} J_0(\lambda\rho) e^{-\gamma_2(z_j+z_k)}\right] \lambda d\lambda, \tag{4.102}$$

where $r_I = \sqrt{\rho^2 + (z_j + z_k)^2}$.

Now we calculate the field components with the use of the dyadic Green function (A.117) [10] in cylinder coordinates

$$\mathbf{E}_j^I = \frac{k_2^2}{\epsilon_2} \mathbf{G}_{j,k}^I \mathbf{P}_k, \tag{4.103}$$

to obtain [52] [53]

$$E_\rho^V = \frac{-P_\rho}{4\pi\epsilon_2}\left(\frac{\partial^2}{\partial\rho\partial z} k_1^2 V'_{22} + \frac{k_1^2 - k_2^2}{k_1^2 + k_2^2}\frac{\partial^2}{\partial\rho\partial z}\frac{e^{ik_2 r_I}}{r_I}\right), \tag{4.104}$$

$$E_z^V = \frac{-P_z}{4\pi\epsilon_2}\left[\left(\frac{\partial^2}{\partial z^2} + k_2^2\right) k_1^2 V'_{22} + \frac{k_1^2 - k_2^2}{k_1^2 + k_2^2}\left(\frac{\partial^2}{\partial z^2} + k_2^2\right)\frac{e^{ik_2 r_I}}{r_I}\right], \tag{4.105}$$

with

$$V'_{22} = V_{22} - \frac{2}{k_1^2 + k_2^2}\frac{e^{ik_2 r_I}}{r_I}, \qquad V_{22} = 2\int_0^\infty \frac{e^{-\gamma_2(z_j+z_k)}}{k_1^2\gamma_2 + k_2^2\gamma_1} J_0(\lambda\rho)\lambda d\lambda, \tag{4.106}$$

for a verticle dipole. Similary for a horizontal electric dipole,

$$E_\rho^H = \frac{-P_\rho}{4\pi\epsilon_2}\cos\phi\left[\frac{\partial^2}{\partial\rho^2}k_1^2V_{22}' + k_2^2U_{22}' + \frac{k_1^2-k_2^2}{k_1^2+k_2^2}\left(\frac{\partial}{\partial\rho^2}+k_2^2\right)\frac{e^{ik_2r_I}}{r_I}\right], \tag{4.107}$$

$$E_\phi^H = \frac{-P_\rho}{4\pi\epsilon_2}\sin\phi\left[\frac{\partial^2}{\partial\rho^2}k_1^2V_{22}' + k_2^2U_{22}' + \frac{k_1^2-k_2^2}{k_1^2+k_2^2}\left(\frac{\partial}{\partial\rho^2}+k_2^2\right)\frac{e^{ik_2r_I}}{r_I}\right], \tag{4.108}$$

$$E_z^H = -\cos\phi E_\rho^V, \tag{4.109}$$

with

$$U_{22}' = U_{22} - \frac{2k_2^2}{k_1^2+k_2^2}\frac{e^{ik_2r_I}}{r_I}, \qquad U_{22} = 2\int_0^\infty \frac{e^{-\gamma_2(z_j+z_k)}}{\gamma_2+\gamma_1}J_0(\lambda\rho)\lambda d\lambda. \tag{4.110}$$

For $z_j + z_k < \rho$ a faster convergence is achieved by the use of Hankel functions

$$V_{22} = \int_0^\infty \frac{e^{-\gamma_2(z_j+z_k)}}{k_1^2\gamma_2+k_2^2\gamma_1}H_0^2(\lambda\rho)\lambda d\lambda, \qquad U_{22} = \int_0^\infty \frac{e^{-\gamma_2(z_j+z_k)}}{\gamma_2+\gamma_1}H_0^2(\lambda\rho)\lambda d\lambda. \tag{4.111}$$

The exact integration paths are described in [52, 54]. Now one groups the integrals in the following set of parameters

$$I_\rho^V = \frac{\partial^2}{\partial\rho\partial z}k_1^2V_{22}, \qquad I_z^V = \left(\frac{\partial^2}{\partial z^2}+k_2^2\right)k_1^2V_{22}, \tag{4.112}$$

and

$$I_\rho^H = \left(\frac{\partial^2}{\partial\rho^2}k_2^2V_{22} + k_2^2U_{22}\right), \qquad I_\phi^H = -\left(\frac{1}{\rho}\frac{\partial}{\partial\rho}k_2^2V_{22} + k_2^2U_{22}\right), \tag{4.113}$$

and transforms to Cartesian field components:

$$E_x^{(x)} = \frac{1}{4\pi\epsilon_2}\left(\left[\left(\frac{x}{\rho}\right)^2 I_\rho^H - \left(\frac{y}{\rho}\right)^2 I_\phi^H\right] - \frac{k_1^2-k_2^2}{k_1^2+k_2^2}\frac{e^{ik_2r}}{r}\left(\frac{\partial^2}{\partial x^2}+k_2^2\right)\right)P_x, \tag{4.114}$$

$$E_y^{(x)} = \frac{1}{4\pi\epsilon_2}\left(\frac{xy}{\rho^2}\left[I_\rho^H + I_\phi^H\right] - \frac{k_1^2-k_2^2}{k_1^2+k_2^2}\frac{e^{ik_2r}}{r}\frac{\partial^2}{\partial x\partial y}\right)P_x, \tag{4.115}$$

$$E_z^{(x)} = \frac{1}{4\pi\epsilon_2}\left(\frac{x}{\rho}I_\rho^V + \frac{k_1^2-k_2^2}{k_1^2+k_2^2}\frac{e^{ik_2r}}{r}\frac{\partial^2}{\partial x\partial y}\right)P_x, \tag{4.116}$$

$$E_x^{(y)} = \frac{1}{4\pi\epsilon_2}\left(\frac{xy}{\rho^2}\left[I_\rho^H + I_\phi^H\right] - \frac{k_1^2-k_2^2}{k_1^2+k_2^2}\frac{e^{ik_2r}}{r}\frac{\partial^2}{\partial x\partial y}\right)P_y, \tag{4.117}$$

$$E_y^{(y)} = \frac{1}{4\pi\epsilon_2}\left(\left[\left(\frac{y}{\rho}\right)^2 I_\rho^H - \left(\frac{x}{\rho}\right)^2 I_\phi^H\right] - \frac{k_1^2-k_2^2}{k_1^2+k_2^2}\frac{e^{ik_2r}}{r}\left(\frac{\partial^2}{\partial x^2}+k_2^2\right)\right)P_y, \tag{4.118}$$

$$E_z^{(y)} = \frac{1}{4\pi\epsilon_2}\left(\frac{y}{\rho}I_\rho^V + \frac{k_1^2-k_2^2}{k_1^2+k_2^2}\frac{e^{ik_2r}}{r}\frac{\partial^2}{\partial y\partial z}\right)P_y, \tag{4.119}$$

$$E_x^{(z)} = \frac{1}{4\pi\epsilon_2}\left(\frac{x}{\rho}I_\rho^V + \frac{k_1^2-k_2^2}{k_1^2+k_2^2}\frac{e^{ik_2r}}{r}\frac{\partial^2}{\partial x\partial z}\right)P_z, \tag{4.120}$$

$$E_y^{(z)} = \frac{1}{4\pi\epsilon_2}\left(\frac{y}{\rho}I_\rho^V + \frac{k_1^2-k_2^2}{k_1^2+k_2^2}\frac{e^{ik_2r}}{r}\frac{\partial^2}{\partial y\partial z}\right)P_z, \tag{4.121}$$

$$E_z^{(z)} = \frac{1}{4\pi\epsilon_2}\left(I_z^V + \frac{k_1^2-k_2^2}{k_1^2+k_2^2}\frac{e^{ik_2r}}{r}\frac{\partial^2}{\partial z^2}+k_2^2\right)P_z. \tag{4.122}$$

Here $\cos\phi = x/\rho$ and $\sin\phi = y/\rho$. The interaction matrix now includes next to the standard interactions

$$\mathbf{G}_{jk} = -\frac{e^{ik_0r_{jk}}}{r_{jk}}\begin{pmatrix} \beta_{jk}+\gamma_{jk}\hat{r}_{jk,x}^2 & \gamma_{jk}\hat{r}_{jk,x}\hat{r}_{jk,y} & \gamma_{jk}\hat{r}_{jk,x}\hat{r}_{jk,z} \\ \gamma_{jk}\hat{r}_{jk,y}\hat{r}_{jk,x} & \beta_{jk}+\gamma_{jk}\hat{r}_{jk,y}^2 & \gamma_{jk}\hat{r}_{jk,y}\hat{r}_{jk,z} \\ \gamma_{jk}\hat{r}_{jk,y}\hat{r}_{jk,x} & \gamma_{jk}\hat{r}_{jk,z}\hat{r}_{jk,y} & \beta_{jk}+\gamma_{jk}\hat{r}_{jk,z}^2 \end{pmatrix}, \tag{4.123}$$

with

$$r_{jk} = [(x_j-x_k)^2 + (y_j-y_k)^2 + (z_j-z_k)^2]^{1/2}, \tag{4.124}$$

$$\hat{r}_{jkx} = \frac{r_{jkx}}{r_{jk}}, \qquad \hat{r}_{jky} = \frac{r_{jky}}{r_{jk}}, \qquad \hat{r}_{jkz} = \frac{r_{jkz}}{r_{jk}}, \tag{4.125}$$

$$\beta_{jk} = \left[\mathbf{1} - (k_0 r_{jk})^{-2} + i(k_0 r_{jk})^{-1}\right], \qquad \gamma_{jk} = -\left[\mathbf{1} - 3(k_0 r_{jk})^{-2} + 3i(k_0 r_{jk})^{-1}\right], \tag{4.126}$$

the

reflection matrix R_{jk}

$$\mathbf{R}_{jk} = -\begin{pmatrix} \hat{r}^{I2}_{jkx} I^H_\rho - \hat{r}^{I2}_{jky} I^H_\phi & \hat{r}^{I2}_{jkx}\hat{r}^{I2}_{jky}(I^H_\rho + I^H_\phi) & \hat{r}^{I2}_{jkx} I^V_\rho \\ \hat{r}^{I2}_{jkx}\hat{r}^{I2}_{jky}(I^H_\rho + i^H_\phi) & \hat{r}^{I2}_{jkx} i^H_\rho - \hat{r}^{I2}_{jky} I^H_\phi & \hat{r}^{I2}_{jky} I^V_\rho \\ -\hat{r}^{I2}_{jkx} I^V_\rho & -\hat{r}^{I2}_{jky} I^V_\rho & I^V_z \end{pmatrix} - \frac{k_1^2 - k_2^2}{k_1^2 + k_2^2} \frac{e^{(ik_0 r_{Ijk})}}{r_{Ijk}} \begin{pmatrix} -(\beta^I_{jk} + \gamma^I_{jk})\hat{r}^{I2}_{jkx} & -\gamma^I_{jk}\hat{r}^{I2}_{jkx}\hat{r}^{I2}_{jky} & \gamma^I_{jk}\hat{r}^{I2}_{jkx}\hat{r}^{I2}_{jkz} \\ -\gamma^I_{jk}\hat{r}^{I2}_{jky}\hat{r}^{I2}_{jkx} & -(\beta^I_{jk} + \gamma^I_{jk})\hat{r}^{I2}_{jky} & \gamma^I_{jk}\hat{r}^{I2}_{jky}\hat{r}^{I2}_{jkz} \\ -\gamma^I_{jk}\hat{r}^{I2}_{jkz}\hat{r}^{I2}_{jkx} & -\gamma^I_{jk}\hat{r}^{I2}_{jkz}\hat{r}^{I2}_{jky} & \beta^I_{jk} + \gamma^I_{jk})\hat{r}^{I2}_{jkz} \end{pmatrix}, \tag{4.127}$$

with

$$r^I_{jk} = [(x_j - x_k)^2 + (y_j - y_k)^2 + (z_j + z_k)^2]^{1/2}, \tag{4.128}$$

$$\hat{r}^I_{jkx} = \frac{r^I_{jkx}}{r^I_{jk}}, \qquad \hat{r}^I_{jky} = \frac{r^I_{jky}}{r^I_{jk}}, \qquad \hat{r}^I_{jkz} = \frac{r^I_{jkz}}{r^I_{jk}}, \tag{4.129}$$

$$\beta^I_{jk} = \left[\mathbf{1} - (k_0 r^I_{jk})^{-2} + i(k_0 r^I_{jk})^{-1}\right], \qquad \gamma^I_{jk} = -\left[\mathbf{1} - 3(k_0 r^I_{jk})^{-2} + 3i(k_0 r^I_{jk})^{-1}\right]. \tag{4.130}$$

With this modifications discrete dipole approximation simulations which include substrate effects are possible. However, because of the volume discretization the computational cost of discrete dipole approximation simulations is very high compared

to boundary element method simulations where only a boundary discretization is necessary.

5. Results

5.1. Implementation

MNPBEM Toolbox

The MNPBEM Toolbox is a Matlab toolbox for the simulation of electromagnetic properties of metallic nanoparticles which was developed by Ulrich Hohenester and Andreas Trügler [35]. It uses a boundary element approach developed by F. J. Garcia de Abajo and A. Howie [26]. The MNPBEM Toolbox has been implemented with Matlab classes and includes help pages and demo files. There also exists a version for electron energy loss spectroscopy simulations [31]. With this version it is also possible to perform a tomography of particle plasmon fields [36, 37]. Features included in the toolbox are plane wave and dipole excitations and solution schemes based on the full Maxwell equations and on the quasistatic approximation. A MNPBEM simulation usually includes the following steps [35]: First, one has to set up the dielectric environment. (Implemented are constant dielectric functions, Drude dielectric functions and tabulated dielectric functions.) The next step is to create the particle geometry, define how the particle is embedded in the dielectric environment and decide the excitation scheme. Then the boundary element working equations are solved for every wavelength and one obtains the surface charges (and currents) at the particle boundaries from which the electromagnetic properties of the metallic nanoparticles can be computed.

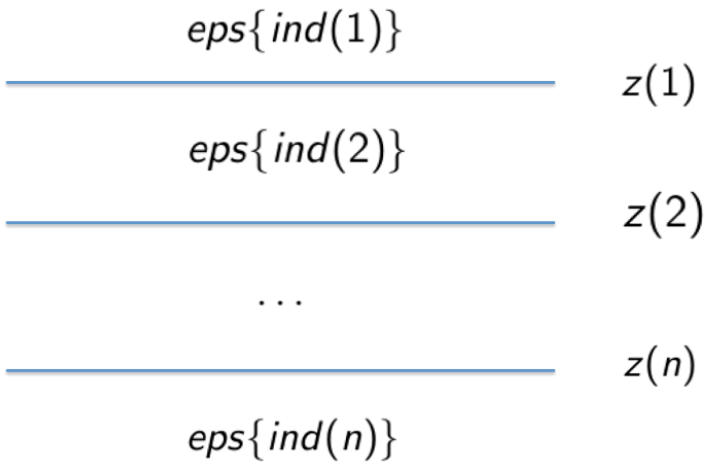

Figure 5.1.: Schematic representation of a layer structure. For the simulation of particles situated on a substrate or embedded in a layer structure, one additionaly needs to define the dielectric functions of the layer structure, the arrangement of the different materials and the positions of the interfaces [93].

Layer structure

For particles situated on a substrate or embedded in a layer, one additonaly needs to set up a layer structure (see Fig. 5.1). Therefore one has to define the dielectric functions of the layer structure, the arrangement of the different materials and the positions of the interfaces. In addition one can change properties related to the evaluation of the reflected Green functions as well. The following properties can be modified [93]:

- ztol: Minimal distance for which boundary elements belong to the layer structure or not. (default value 0.02)
- rmin: Minimum radial distance for the calculation of the reflected Green functions. (default value 0.01)

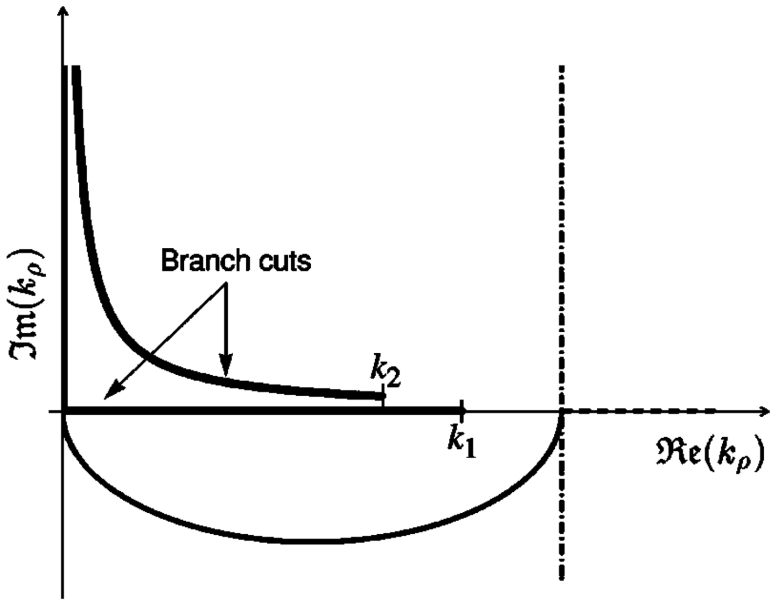

Figure 5.2.: Deflection of the integration path in the complex plane to surround the singularites [10] in an elliptical path. The parameters rmin, zmin, ratio and semi define the integration path which is used for the evaluation of the reflected Green functions. For zmin >= r / ratio the integration path along the real axis is used. For zmin < r / ratio the integration path along the imaginary axis is used. The parameter semi defines the semicircle for the first part of the complex plane integration and op allows to change parameters of the ODE integration. . (Figure taken from [71].)

- zmin: Minimum distance to layer for the calculation of the reflected Green functions. (default value 0.01)
- semi: Ratio of semicircle for the complex plane integration. (default value $k_\rho^{min} : k_\rho^{maj} = 0.1$)
- ratio: Determines whether the Bessel or Hankel function integration path is used. (default value $z : r = 2$)
- op: Tolerance, step size and other options for ODE integration

These parameters are important for the following reasons. Because of the presence of a singularity contribution the boundary elements of a particle must have a certain distance to the interface. For distances smaller ztol it is assumed that the boundary element belongs to the interface. The parameters rmin, zmin, ratio and semi define the integration path which is used for the evaluation of the reflected Green functions. For zmin >= r / ratio the integration path along the real axis is used. For zmin < r / ratio the integration path along the imaginary axis is used. The parameter semi defines the semicircle for the first part of the complex plane integration and op allows to change parameters of the ODE integration.

Reflected Green functions

The calculation of the reflected Green functions is computationally very demanding. Therefore it is done in a two step process. First one sets up a suitable grid (see Fig. 5.3) of Green function values and then in the second step performs an interpolation. The reflected Green functions depend on the radial distance between the source point and the observation point and on their z-values. For the functional dependence a shape similar to the quasistatic Green function is asumed (as shown in 4.79-4.81). The definition of the grid can be done manually or automatically in the MNPBEM toolbox [93]. The following properties can be modified:

- scale: Factor to enlarge the grid size. (default value 1.05)
- range: Set 'full' for the grid to start directly from the interface.
- nr: Number of r-values of the grid.(default value 30)
- nz: Number of z-values of the grid. (default value 30)
- rmod: Determines whether logarithmic or linear spacing for r-table is used.
- zmod: Determines whether logarithmic or linear spacing for z-table is used.

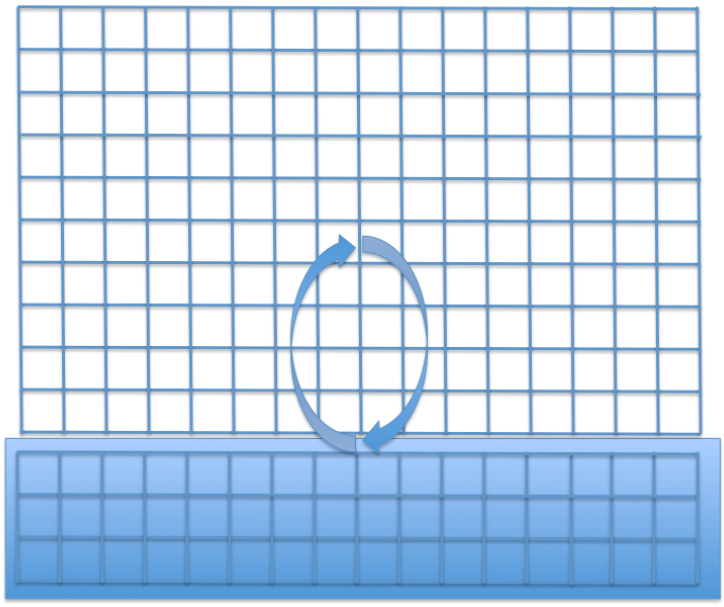

Figure 5.3.: Schematic representation of a grid used for the calculation of the reflected Green functions. Because the evaluation of these Green functions is computationally very demanding it is done in a two step process. First one sets up a suitable grid of Green function values and then in the second step performes an interpolation [93].

Program outline for a MNPBEM simulation for a nanoparticle situated on a substrate or embedded in a layer structure

A typical program for the simulation of the electromagnetic properties of a metallic nanoparticle situated on a substrate or embedded in a layer structure includes the following steps [35, 93]:

- Definition of dielectric environment:
  Defining the material parameters of the particle, the layer structure and the dielectric background. The MNPBEM Toolbox includes constant dielectric functions, Drude dielectric functions and tabulated dielectric functions.

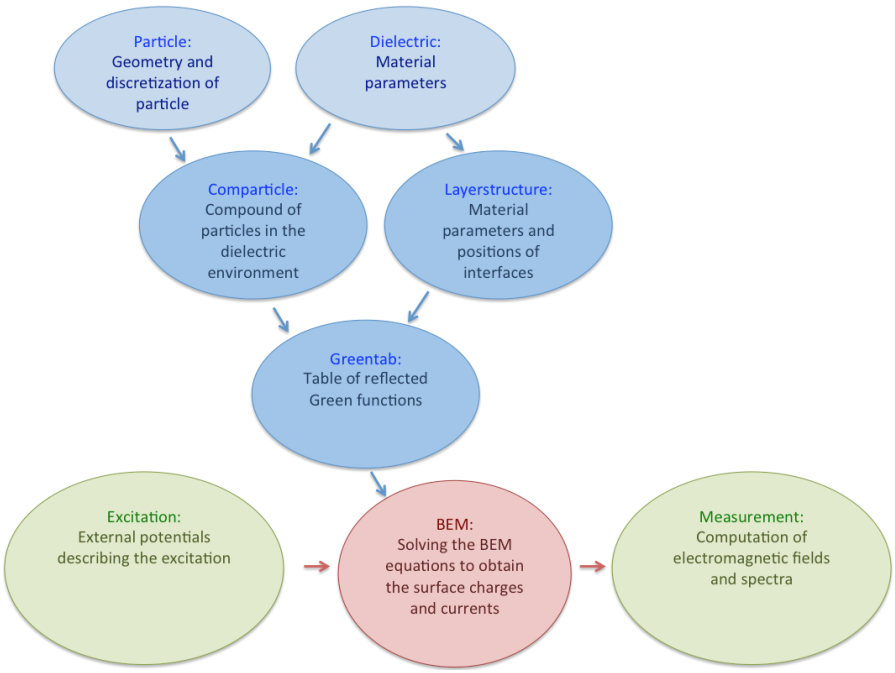

Figure 5.4.: Flow chart of a BEM simulation with layerstructure: First one defines material parameters and sets up the particle geometry. Next one defines a comparticle object which defines the dielectric environment and a layerstructure. Then a table of reflected Green functions is computed. For a given excitation the BEM solver then calculates surface charges (and surface currents) which can be used for the calculation of the spectra and the electromagnetic fields [93].

- Initialization of the particle:
  Setting up the particle geometry and the discretization of its boundary. The MNPBEM Toolbox includes basic geometries (sphere, rod, cube and torus) as well as a polygon class which uses the Mesh2d toolbox.

- Defining the dielectric properties of the particle:
  Defining the material parameters of the particle.

- Initialization of the layer structure:
  Setting up the positions of the boundary interfaces and the material properties

of the layer structure.

- Grid for reflected Green functions:
  Defining the grid for the calculation of the reflected Green functions. This can be done manually or automatically.
- Definition of the excitation:
  One can choose between a plane wave excitation and the excitation through the fields of an oscillating dipole.
- Setting up the BEM solver:
  The MNPBEM Toolbox includes BEM solver built on the full Maxwell equations as well as on the quasistatic approximation.
- Spectra and Electromagnetic fields:
  Computation of the spectra and electromagentic fields.

In the next section we present simulation results done with the MNPBEM Toolbox. We start with a comparison between the simulation method using the full Maxwell equations to the one using the quasistatic approximation. Then we compare the boundary element method implementation to the discrete dipole approximation simulation with surface interaction. After that we show electric field maps for a sphere above a substrate and study the substrate effect for a disk approaching a substrate. We also present the field enhancement for two gold spheres embedded in a layer structure and compare scattering cross sections for particles with different geometries and different surface discretizations.

5.2. Results

Comparison with quasistatic simulations

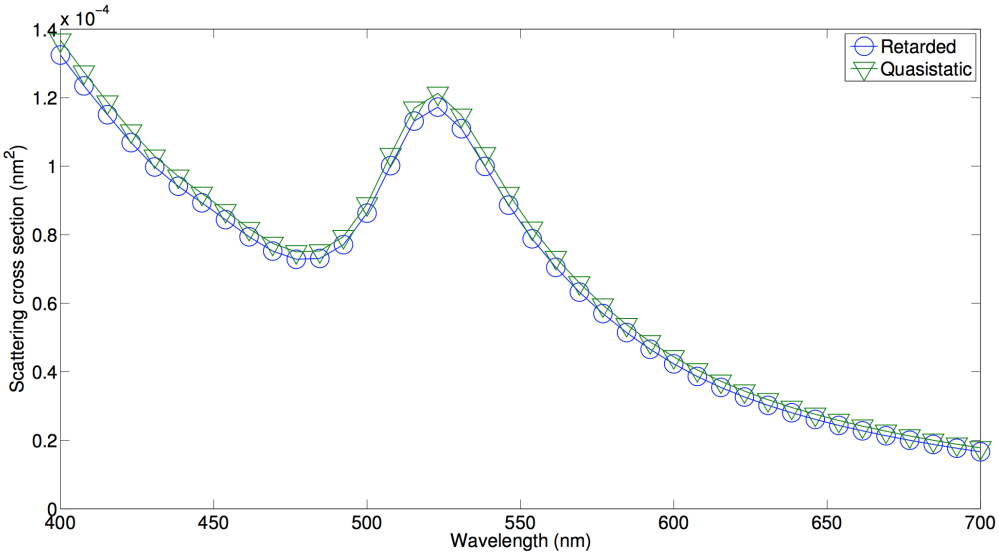

Figure 5.5.: Comparison of scattering cross sections of a gold sphere with a diameter of 5 nm located 0.5 nm away from a glass substrate with a refractive index of 1.5 which is illuminated by a plane wave from above obtained by quasistatic and retarded boundary element method simulations. A surface discretization with 256 boundary elements was used.

In Fig. 5.5 we present simulated scattering spectra of a 5 nm gold sphere located 0.5 nm above a glass substrate with a refractive index of 1.5 which is illuminated by a plane wave from above. We compare quasistatic and retarded boundary element method simulation results. In both cases a surface discretization with 256 boundary elements was used.

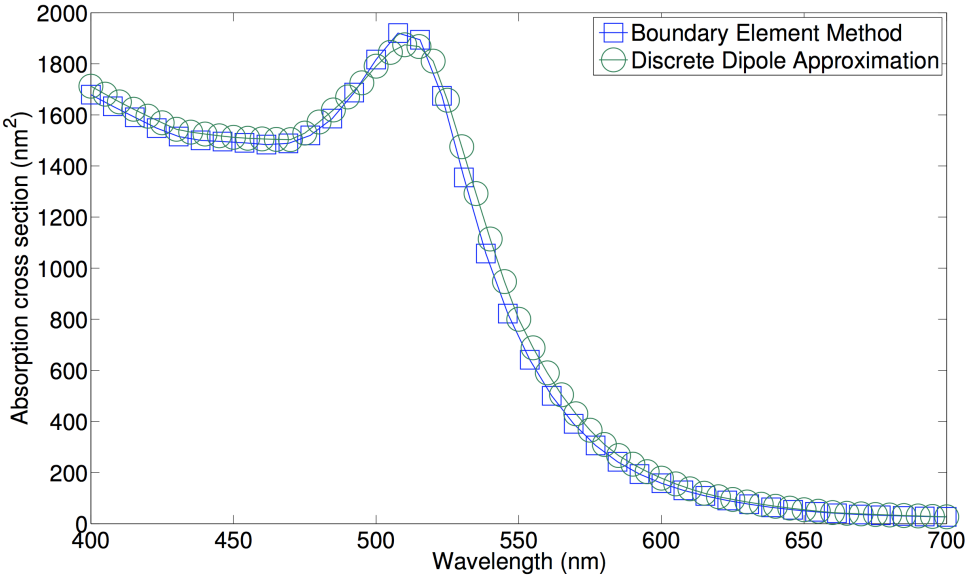

Figure 5.6.: Comparison of absorption cross sections of a gold sphere with a diameter of 50 nm located 1 nm away from a glass substrate with a refractive index of 1.52 which is illuminated by a plane wave from above obtained by the boundary element method and the discrete dipole approximation. For the boundary element method simulation a surface discretization with 1246 boundary elements was used. For the discrete dipole approximation simulation a discretization with 1472 point dipoles was used. For larger particles the boundary element simulations are faster because only the boundary and not the whole volume needs to be discretized.

Comparison with discrete dipole approximation simulations

In Fig. 5.6 we also compare the boundary element method to the discrete dipole approximation method. The considered system consists of a 50 nm gold sphere located 1 nm away from a glass substrate with a refractive index of 1.52 which is illuminated from above. Again a good agreement throughout the whole wavelength regime is achieved. In [52, 53] the discrete dipole approximation simulations with surface interaction were also compared to finite difference time domain simulations.

Electric field and radiation pattern of gold sphere near substrate

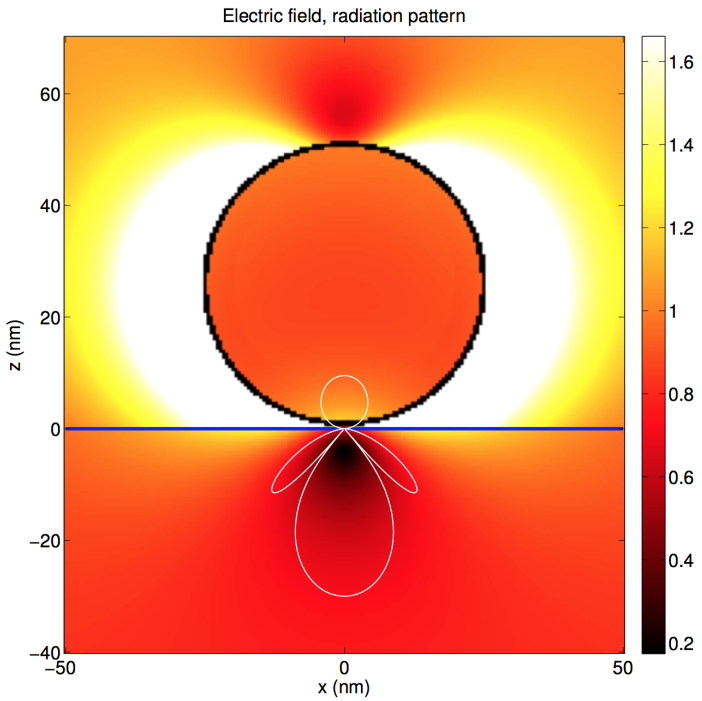

Figure 5.7.: Electric field, radiation pattern of a gold sphere with a diameter of 50 nm located 1 nm away from a glass substrate with a refractive index of 1.52 which is illuminated by a plane wave from above obtained by the boundary element method.

With the known surface charges and currents it is also possible to calculate the electric field and the radiation pattern of a considered system. Fig. 5.7 shows the influence of the substrate with a refractive index of 1.52 to the electric field distribution of a gold sphere with a diameter of 50 nm. The sphere is located 1 nm away from the substrate and illuminated by a plane wave from above.

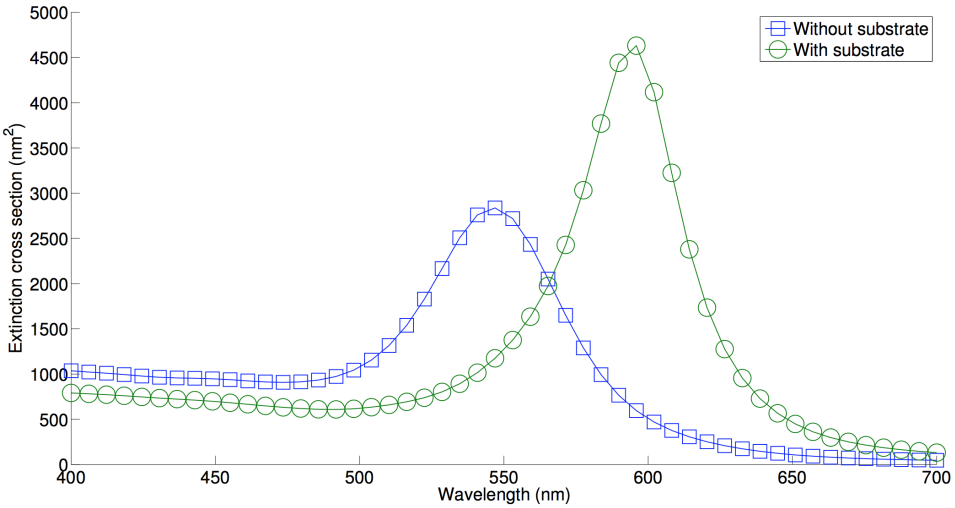

Figure 5.8.: Comparison of extinction cross sections of a gold disk with a diameter of 40 nm and a height of 10 nm located in free space and on a substrate with a refractive index of 1.5 which is illuminated by a plane wave from above obtained by the boundary element method. For the boundary element method simulation a surface discretization of 2264 boundary elements was used. The presence of the substrate leads to a redshift and an increase in the amplitude of the extinction spectra.

Disk above substrate

In Fig. 5.8 we study the effect of a presence of substrate with a refractive index of 1.5 on the extinction spectra of gold disk with a diameter of 40 nm and a height of 10 nm. Therefore we compare the resulting extinction spectra to a simulation where the disk is located in free space. The presence of the substrate leads to a redshift and an increase in the amplitude of the extinction spectra.

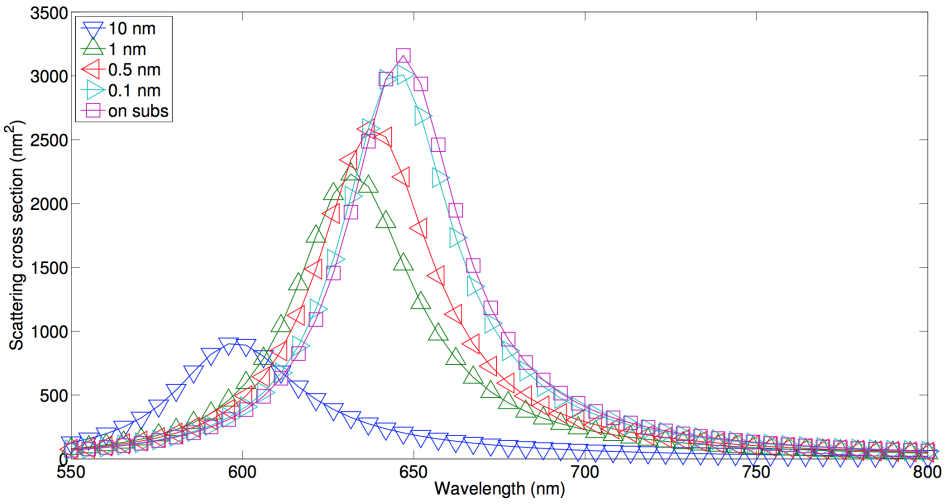

Figure 5.9.: Comparison of scattering cross sections of a gold disk with a diameter of 60 nm and a height of 10 nm approaching a substrate with a refractive index of 1.5 and which is illuminated by a plane wave with an incidence angle of 40° obtained by the boundary element method. The numbers in the legend indicate the distance in nm to the substrate. With decreasing distance a redshift of the resonance is observed. For the boundary element method simulations a surface discretization of 1430 boundary elements was used.

Disk approaching substrate

Fig. 5.9 also shows the change of the scattering cross section of a gold disk with a diameter of 60 nm and a height of 10 nm approaching a substrate with a refractive index of 1.5 and which is illuminated by a plane wave with an incidence angle of 40° obtained by the boundary element method. The numbers in the legend indicate the distance in nm to the substrate. With decreasing distance again a redshift of the resonance is observed.

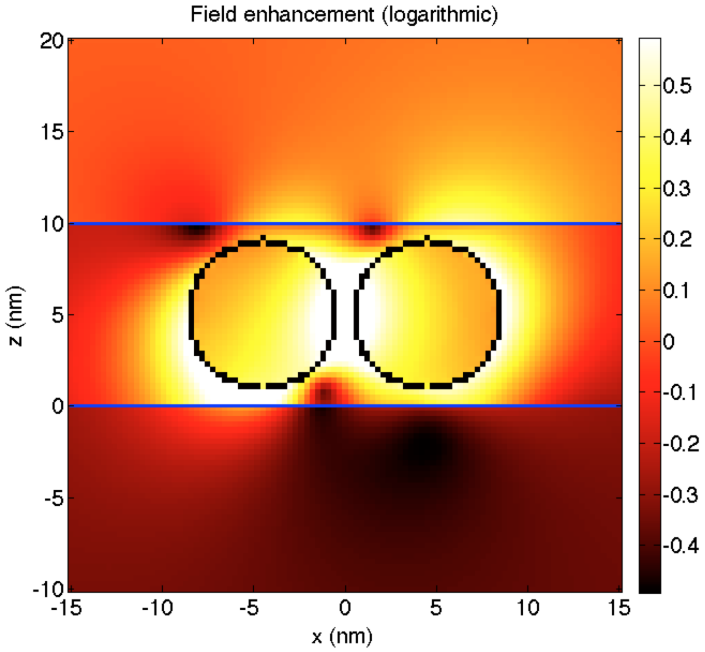

Figure 5.10.: Electric field of two gold spheres with a diameter of 8 nm and a gap of 1 nm between them embedded inside a layer with a refractive index of 1.5811 on top of a substrate with refractive index of 3.1625 illuminated by a plane wave with an incidence angle of 40° obtained by the boundary element method. For the boundary element method simulation a surface discretization of 144 boundary elements per sphere was used.

Gold spheres embedded in layer structure

Fig. 5.10 shows the electric fields of two gold spheres with a diameter of 8 nm and a gap of 1 nm between them embedded inside a layer with a refractive index of 1.5811 on top of a substrate with refractive index of 3.1625 illuminated by a plane wave with an incidence angle of 40° obtained by the boundary element method.

Convergence of the scattering cross section of a gold sphere situated on a glass substrate

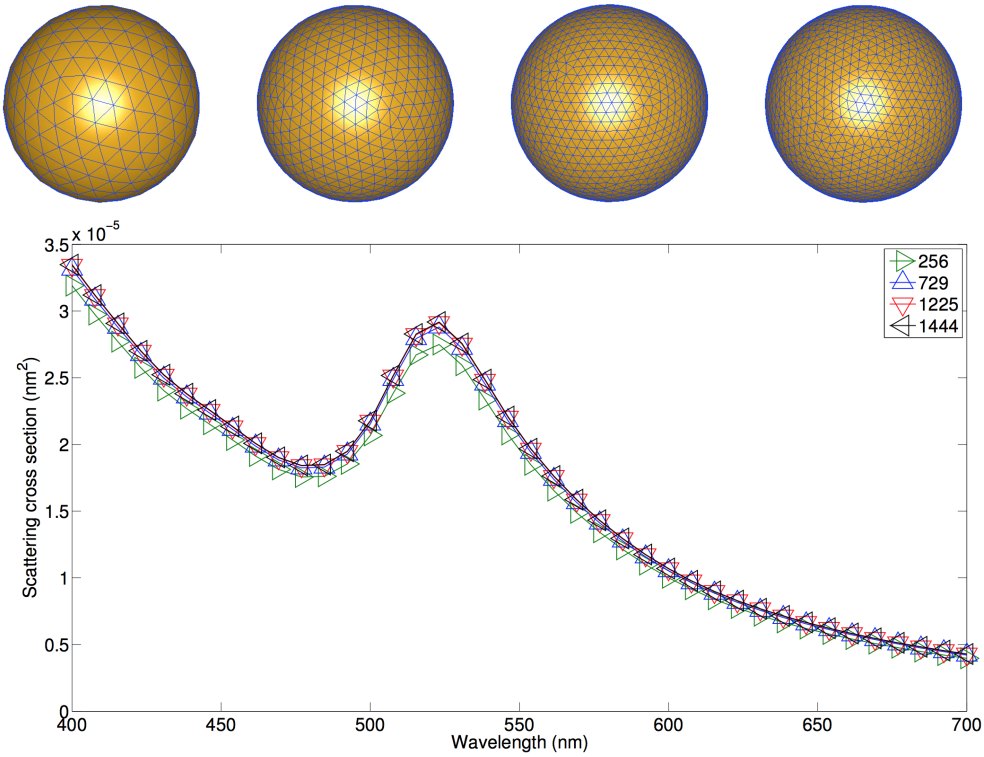

Figure 5.11.: Comparison of scattering cross sections of a gold sphere with a diameter of 4 nm located 1 nm away from a substrate with a refractive index of 1.5 which is illuminated by a plane wave from above obtained by the boundary element method. The numbers in the legend indicate the number of surface elements used for the discretization of the sphere and are also shown in the upper panel.

To find converged results a certain number of boundary elements are necessary. Fig. 5.11 shows scattering cross sections of a gold sphere with a diameter of 4 nm which is located 1 nm away from a substrate with a refractive index of 1.5 which is illuminated by a plane wave from above calculated with different surface discretizations. Increasing the number of boundary elements above 1225 boundary elements leads to

no further change of the scattering cross section.

Convergence of the scattering cross section of a gold triangle situated on different substrates

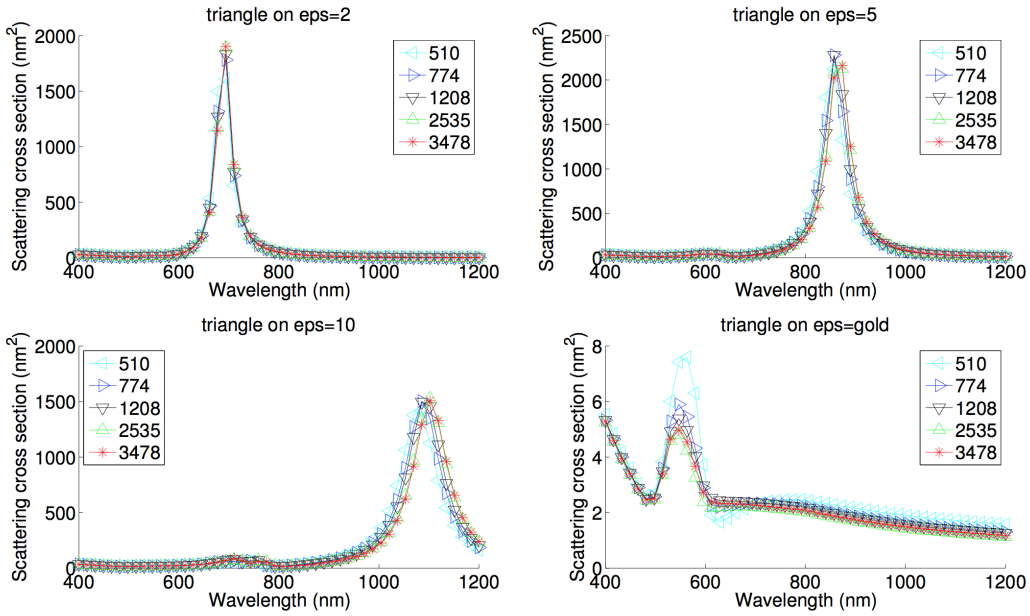

Figure 5.12.: Comparisions of scattering cross sections of a triangle with a length of 60 nm and a height of 10 nm situated on substrates with different permittivities (eps=2, 5, 10 and gold) which is illuminated by a plane wave from above with an angle of $\pi/4$ obtained by the boundary element method. The numbers in the legend indicate the number of surface elements used.

In Fig. 5.12 scattering cross sections of a triangle with a length of 60 nm and a height of 10 nm situated on substrates with different permittivities (eps=2, 5, 10 and gold) which is illuminated by a plane wave from above with an angle of $\pi/4$ obtained by the boundary element method are shown. The numbers in the legend indicate the number of surface elements used.

Convergence of the scattering cross section of a gold cube situated on different substrates

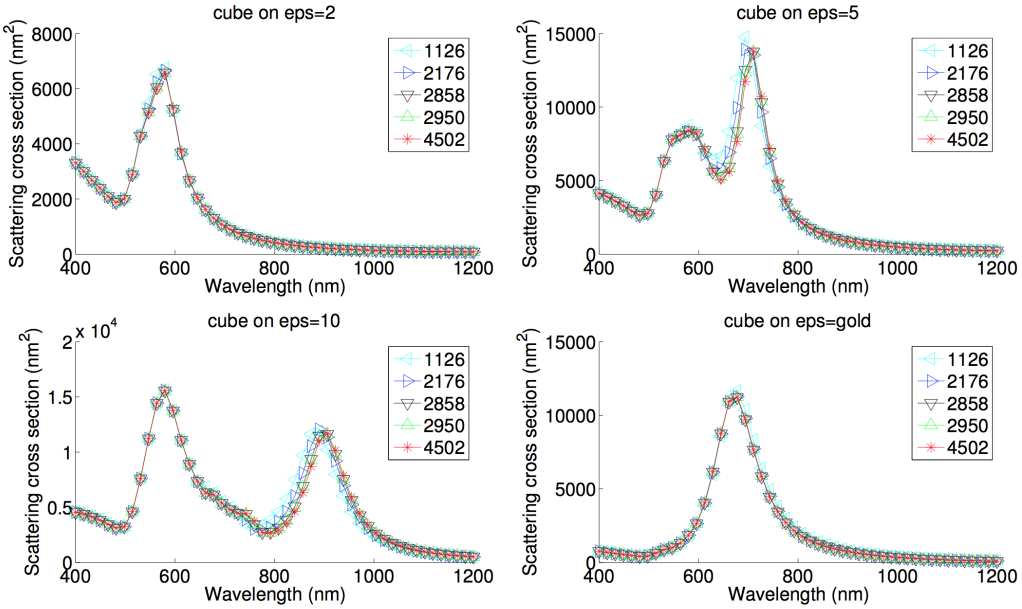

Figure 5.13.: Comparisions of scattering cross sections of a cube with a length of 60 nm situated on substrates with different permittivities (eps=2, 5, 10 and gold) which is illuminated by a plane wave from above with an angle of $\pi/4$ obtained by the boundary element method. The numbers in the legend indicate the number of surface elements used.

In Fig. 5.13 scattering cross sections of a cube with a length of 60 nm and a height of 60 nm situated on substrates with different permittivities (eps=2, 5, 10 and gold) which is illuminated by a plane wave from above with an angle of $\pi/4$ obtained by the boundary element method are shown. The numbers in the legend indicate the number of surface elements used.

Convergence of the scattering cross section of a gold disk situated on different substrates

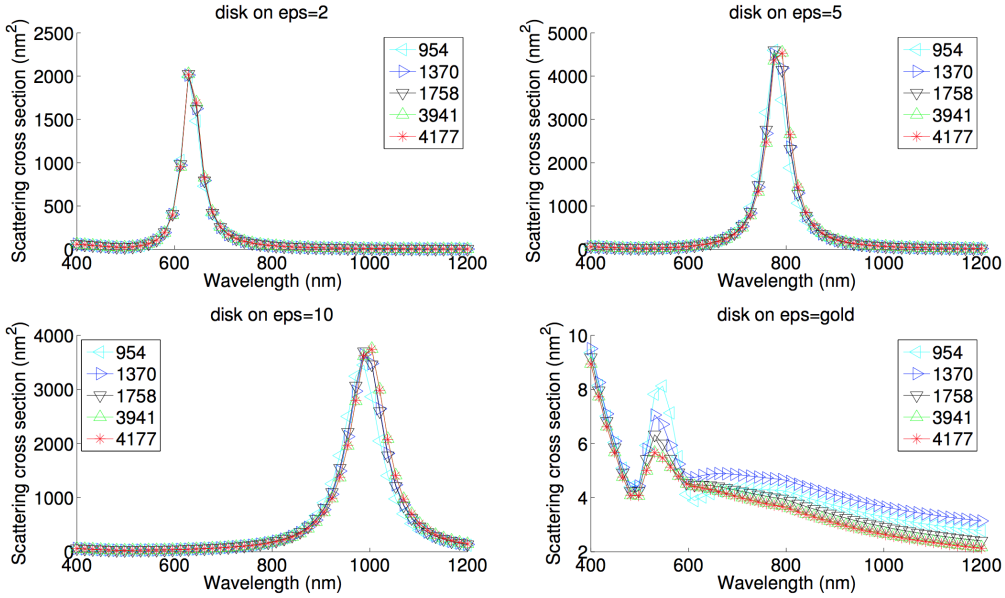

Figure 5.14.: Comparisions of scattering cross sections of a disk with a diameter of 60 nm and a height of 10 nm situated on substrates with different permittivities (eps=2, 5, 10 and gold) which is illuminated by a plane wave from above with an angle of $\pi/4$ obtained by the boundary element method. The numbers in the legend indicate the number of surface elements used.

In Fig. 5.14 scattering cross sections of a disk with a diameter of 60 nm and a height of 10 nm situated on substrates with different permittivities (eps=2, 5, 10 and gold) which is illuminated by a plane wave from above with an angle of $\pi/4$ obtained by the boundary element method are shown. The numbers in the legend indicate the number of surface elements used. (We also made simulations with 5762 boundary elements to be sure that the simulations with 4177 boundary elements really show converged results.) For higher permittivities a higher number of surface elements are necessary to obtain converged results.

6. Conclusion and Outlook

6.1. Conclusion and Outlook

In this thesis we have discussed simulation methods for the optical properties of plasmonic nanoparticles. First we presented simulation methods for particles in free space and thereafter modifications for particles situated on substrates where shown. The main part was the modification of the boundary element method approach and the calculation of the reflected Green functions where a certain path in the complex plane was used. By setting up a suitable grid and using an interpolation for the reflected Green functions a speedup of the simulations is achieved. With this modification boundary element method simulations of optical properties of plasmonic nanoparticles situated on substrates and embedded in layer structures become feasible. We also made simulations with a different number of boundary elements to study the convergence of the simulation approach. However, because the convergence also depends on the permittivities of the substrate and the dielectric background and on the particle geometry no easy argument about the sufficient number of boundary elements needed to obtain converged results can be given. In the end one can only increase the surface discretization until no further change in the spectrum is observed. For reducing the computation time one can also try to find faster integration routines for the Sommerfeld integrals.

A. Appendix

A.1. Boundary conditions

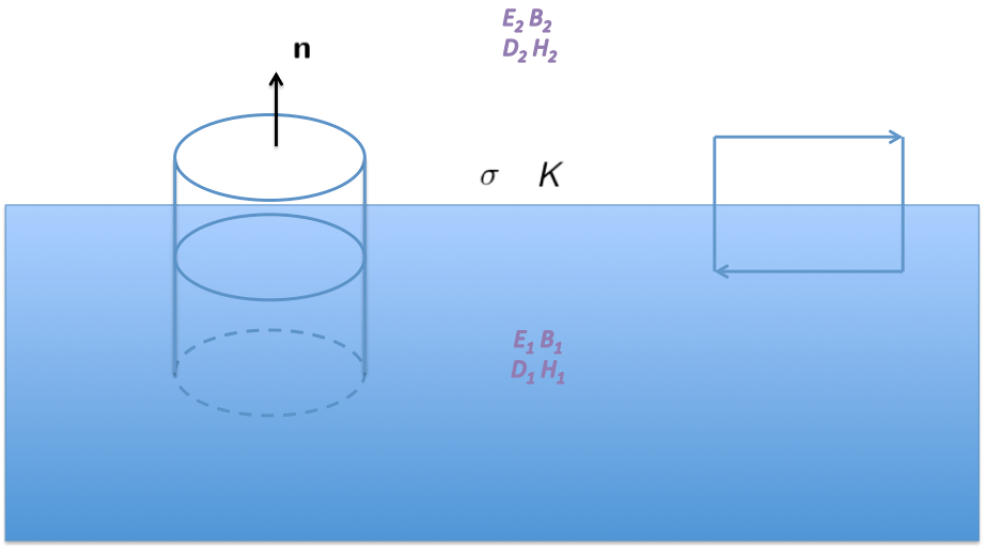

Figure A.1.: The boundary conditons are found by applying the integral forms of the Maxwell equations to an infinitesimal small cylinder and an infinitesimal small contour.

The boundary conditons can be obtained by using the theorems of Gauss and Stoke [40] [42] and transforming the Maxwell equations to their

integral forms

$$\int_{\partial V} \mathbf{D}(\mathbf{r},t)\cdot\mathbf{n}_s da = \int_V \rho(\mathbf{r},t)dV, \tag{A.1}$$

$$\int_{\partial V} \mathbf{B}(\mathbf{r},t)\cdot\mathbf{n}_s da = 0, \tag{A.2}$$

$$\int_{\partial S} \mathbf{E}(\mathbf{r},t)\cdot d\mathbf{s} = -\int_S \frac{\partial}{\partial t}\mathbf{B}(\mathbf{r},t)\cdot\mathbf{n}_s da, \tag{A.3}$$

$$\int_{\partial S} \mathbf{H}(\mathbf{r},t)\cdot d\mathbf{s} = \int_S [\mathbf{j}(\mathbf{r},t) + \frac{\partial}{\partial t}\mathbf{D}(\mathbf{r},t)]\cdot\mathbf{n}_s da, \tag{A.4}$$

where da denotes a surface element, n_s the normal unit vector to the surface, ds a line element, ∂V the surface of the volume V, and ∂S the border of the surface S,

and then applying them to an infinitesimal small cylinder and an infintesimal small contour. In the limit of an infinitesimal cylinder the side surfaces don't contribute to the integrals and the only possible charge is an idealized surface charge σ . The first two Maxwell's equations lead to

the boundary conditions for the normal field components

$$\mathbf{n}\cdot(\mathbf{D}_i - \mathbf{D}_j) = \sigma, \tag{A.5}$$

$$\mathbf{n}\cdot(\mathbf{B}_i - \mathbf{B}_j) = 0. \tag{A.6}$$

By using an infinitesimal small contour the short arms don't contribute to the integrals and the only possible current is an idealized surface current density K. The

other Maxwell's equations lead to

the boundary conditions for the tangential field components

$$\mathbf{n} \times (\mathbf{E}_i - \mathbf{E}_j) = \mathbf{0}, \tag{A.7}$$

$$\mathbf{n} \times (\mathbf{H}_i - \mathbf{H}_j) = \mathbf{K}. \tag{A.8}$$

A.2. Fresnel coefficients

The Fresnel coefficients describe the reflection and transmission of a planar wave at a planar boundary. The boundary conditions at a planar boundary are derived from the scalar wave equations of a source-free medium which the transverse electric and transverse magentic modes have to obey [10]:

$$\left[\mu\frac{d}{dz}\frac{1}{\mu}\frac{d}{dz}+\omega^2\mu\epsilon-k_x^2\right]e_y=0, \tag{A.9}$$

$$\left[\epsilon\frac{d}{dz}\frac{1}{\epsilon}\frac{d}{dz}+\omega^2\mu\epsilon-k_x^2\right]h_y=0. \tag{A.10}$$

The derivative terms must be finite which leads to [10]

$$e_{1y}=e_{2y}, \qquad \mu_1^{-1}\frac{d}{dz}e_{1y}=\mu_2^{-1}\frac{d}{dz}e_{2y}, \tag{A.11}$$

$$h_{1y}=h_{2y}, \qquad \epsilon_1^{-1}\frac{d}{dz}h_{1y}=\epsilon_2^{-1}\frac{d}{dz}h_{2y}. \tag{A.12}$$

To find the Fresnel coefficients we consider now a transverse electric wave [10]

$$E_y=e_y(z)e^{ik_x x}, \tag{A.13}$$

at an one dimensional inhomogeneity. At one side we have the incident and reflected wave

$$e_{1y}(z)=e_0e^{-ik_{1z}z}+R^{TE}e_0e^{ik_{1z}z}, \tag{A.14}$$

and on the other side only a transmitted wave

$$e_{2y}(z)=T^{TE}e_0e^{-ik_{2z}z}. \tag{A.15}$$

Here R^{TE} and T^{TE} are the ratios of the amplitudes of the reflected and the transmitted waves to the amplitude of the incident wave. By using the boundary conditions

we get

$$1 + R^{TE} = T^{TE}, \tag{A.16}$$

$$\frac{k_{1z}}{\mu_1}\left(1 - R^{TE}\right) = \frac{k_{2z}}{\mu_2} T^{TE}, \tag{A.17}$$

from which we can solve for the

Fresnel reflection and transmission coefficients for transverse electric fields

$$R^{TE} = \frac{\mu_2 k_{1z} - \mu_1 k_{2z}}{\mu_2 k_{1z} + \mu_1 k_{2z}}, \tag{A.18}$$

$$T^{TE} = \frac{2\mu_2 k_{1z}}{\mu_2 k_{1z} + \mu_1 k_{2z}}. \tag{A.19}$$

In a similar way the

Fresnel reflection and transmission coefficients for transverse magnetic fields

$$R^{TM} = \frac{\epsilon_2 k_{1z} - \epsilon_1 k_{2z}}{\epsilon_2 k_{1z} + \epsilon_1 k_{2z}}, \tag{A.20}$$

$$T^{TM} = \frac{2\epsilon_2 k_{1z}}{\epsilon_2 k_{1z} + \epsilon_1 k_{2z}}, \tag{A.21}$$

are found.

A.3. Optical properties of metals

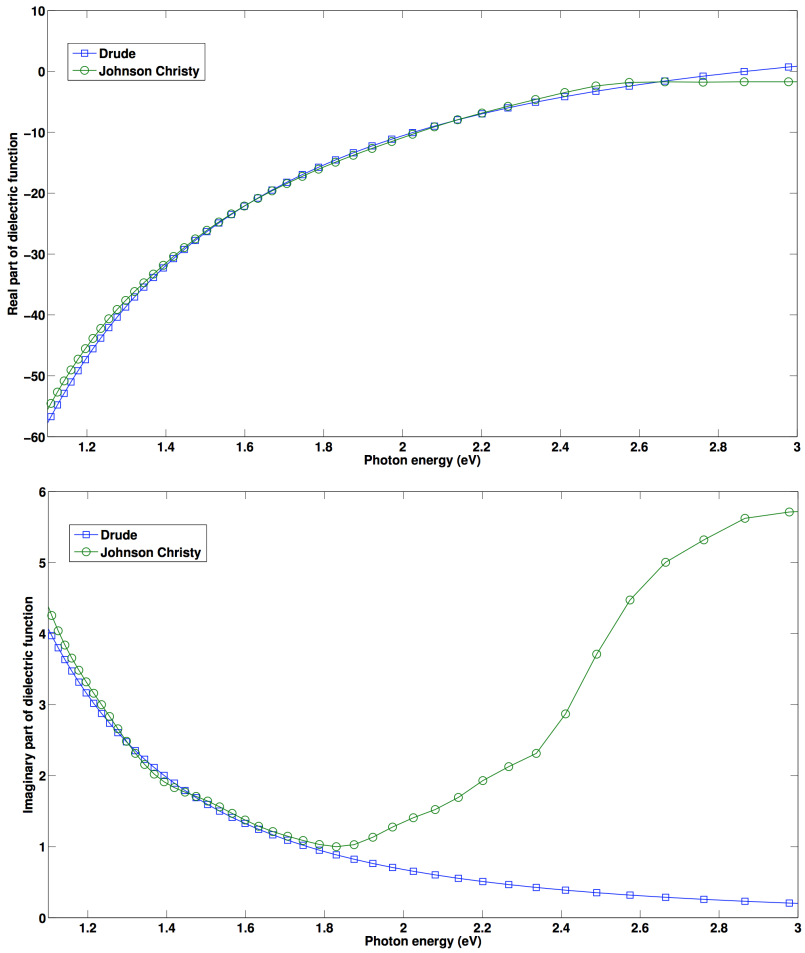

Figure A.2.: The drude model describes the optical response of metals only good for photon energies below the threshold of interband transitions [86] [15].

One simple model for a dielectric function of a metal is the plasma model where a gas of free electrons moves against a fixed background of positive ions [69] [57] [92]. To derive [57] the dielectric function of a free electron gas we start with the equation

of motion for an electron under the influence of an external electromagnetic field

$$m\ddot{\mathbf{x}} + m\gamma\dot{\mathbf{x}} = -e\mathbf{E}. \tag{A.22}$$

Here $\gamma = 1/\tau$ is the characteristic collision frequency with τ the relaxation time of the free electron gas. For a harmonic time dependent driving field with frequency ω

$$\mathbf{E}(t) = \mathbf{E}_0 e^{-i\omega t}, \tag{A.23}$$

we get:

$$\mathbf{x}(t) = \frac{e}{m(\omega^2 + i\omega\gamma)}\mathbf{E}(t). \tag{A.24}$$

The displaced electrons lead to a macroscopic polarization which describes the density of induced electric dipole moments in the material

$$\mathbf{P} = -ne\mathbf{x}, \tag{A.25}$$

$$\mathbf{P} = -\frac{ne^2}{m(\omega^2 + i\omega\gamma)}\mathbf{E}. \tag{A.26}$$

The sum of $\epsilon_0\mathbf{E}$ and the macroscopic polarization is called electric displacement

$$\mathbf{D} = \epsilon_0\mathbf{E} + \mathbf{P}, \tag{A.27}$$

$$\mathbf{D} = \epsilon_0\left(1 - \frac{\omega_p^2}{\omega^2 + i\omega\gamma}\right)\mathbf{E}. \tag{A.28}$$

with

$$\omega_p^2 = \frac{ne^2}{\epsilon_0 m}, \tag{A.29}$$

the square of the plasma frequency.

Hence the complex dielectric function of the free electron gas has the following form

$$\epsilon(\omega) = 1 - \frac{\omega_p^2}{\omega^2 + i\omega\gamma}. \tag{A.30}$$

Its real and imaginary parts are

$$\epsilon'(\omega) = 1 - \frac{\omega_p^2\tau^2}{1 + \omega^2\tau^2}, \tag{A.31}$$

$$\epsilon''(\omega) = \frac{\omega_p^2\tau}{\omega(1 + \omega^2\tau^2)}. \tag{A.32}$$

In the derivation of the model we neglected the magnetic field because its effect is negligible [86] and assumed a spatially uniform electric field. It describes the optical response of metals only good for photon energies below the threshold of interband transitions. The physical meaning of ω_p can be seen by looking at the collective longitudinal oscillations of the conduction electrons against the fixed positive background [57]. A uniform displacement by a distance u generates a charge density

$$\sigma = \pm neu, \tag{A.33}$$

which leads to an electric field

$$E = \frac{neu}{\epsilon_0}. \tag{A.34}$$

The displaced electrons thus experience a restoring force which leads to

$$nm\ddot{u} = -neE = -\frac{n^2e^2u}{\epsilon_0}, \tag{A.35}$$

$$\ddot{u} + \omega_p^2 u = 0. \tag{A.36}$$

The plasma frequency thus is the natural frequency of a free oscillation of the electron gas and the quanta of these oscillations are denoted as plasmons [57]. A better

description [40] [57] of the optical properties of gold and silver at visible frequencies can be found by adding the interband transitions with the classical picture of a bound electron with resonance frequency ω_0

$$m\ddot{\mathbf{x}} + m\gamma\dot{\mathbf{x}} + m\omega_0^2\mathbf{x} = -e\mathbf{E}. \tag{A.37}$$

Using the same ansatz as before we find:

$$\epsilon_{Interband}(\omega) = 1 + \frac{\tilde{\omega}_p^2}{(\omega_0^2 - \omega) - i\gamma\omega}. \tag{A.38}$$

Its real and imaginary parts are

$$\epsilon'_{Interband}(\omega) = 1 + \frac{\tilde{\omega}_p^2(\omega_0^2 - \omega^2)}{(\omega_0^2 - \omega^2)^2 + \gamma^2\omega^2}, \tag{A.39}$$

$$\epsilon''_{Interband}(\omega) = \frac{\gamma\tilde{\omega}_p^2\omega}{(\omega_0^2 - \omega^2)^2 + \gamma^2\omega^2}. \tag{A.40}$$

To compare to real materials one also has to introduce an offset to account for the higher energy interband transitions present [41] [40]. In a real material one has a

sum of Lorentz oscillators

$$\frac{\epsilon(\omega)}{\epsilon_0} = 1 + \frac{Ne^2}{\epsilon_0 m}\sum_j f_i(\omega_j^2 - \omega^2 - i\omega\gamma_j)^{-1}. \tag{A.41}$$

Here f_j are the oscillator strengths, ω_j the binding frequencies and γ_j the damping constants which have to be obtained form a microscopic theory [40]. One important

postulate in physics is causality [40] which states that cause always has to precede its effect. This also has to be true for a frequency dependent dielectric function which relates the electric displacement and the electric field [10]

$$\mathbf{D}(\omega) = \epsilon(\omega)\mathbf{E}(\omega). \tag{A.42}$$

Hence

$$\mathbf{D}(t) = \int_{-\infty}^{t} \epsilon(t-\tau)\mathbf{E}(\tau)d\tau, \tag{A.43}$$

with

$$\epsilon(t) = \frac{1}{2\pi}\int_{-\infty}^{\infty} d\omega e^{-i\omega t}\epsilon(\omega). \tag{A.44}$$

With $\epsilon(\omega) = [\epsilon(\omega) - \epsilon(\infty)] + \epsilon(\infty)$ we find

$$\epsilon(t) = \frac{1}{2\pi}\int_{-\infty}^{\infty} d\omega e^{-i\omega t}[\epsilon(\omega) - \epsilon(\infty)] + \delta(t)\epsilon(\infty). \tag{A.45}$$

Because of causality the real-valued function $\epsilon(t) = 0$ for $t < 0$ and the integrand must be analytic in the upper half of the complex plane. By using the

Cauchy integral formula [29, 50]

$$f(a) = \frac{1}{2\pi i}\oint_{\gamma} \frac{f(z)}{z-a}da, \tag{A.46}$$

which states that a complex differentiable function f defined on a disk is fully determined by its values on the boundary γ,

we find:

$$\epsilon(\omega) - \epsilon(\infty) = \frac{1}{2\pi i}\int_{C-C_\infty} d\omega' \frac{\epsilon(\omega') - \epsilon(\infty)}{\omega' - \omega}, \tag{A.47}$$

Because $\epsilon(\omega) - \epsilon(\infty) \to 0$ if $\omega \to \infty$ this leads to

$$\epsilon(\omega) - \epsilon(\infty) = \frac{1}{2\pi i}\int_{C} d\omega' \frac{\epsilon(\omega') - \epsilon(\infty)}{\omega' - \omega}, \tag{A.48}$$

which can alternativly be written as a principal value integral:

$$\epsilon(\omega) - \epsilon(\infty) = \frac{1}{\pi i} P.V. \int_{-\infty}^{\infty} d\omega' \frac{\epsilon(\omega') - \epsilon(\infty)}{\omega' - \omega}. \tag{A.49}$$

For the the real and imaginary parts of the dielectric function we find the

Krames Kronig relations [10] [40]

$$\epsilon'(\omega) - \epsilon(\infty) = \frac{1}{\pi} P.V. \int_{-\infty}^{\infty} d\omega' \frac{\epsilon''(\omega')}{\omega' - \omega}, \tag{A.50}$$

$$\epsilon''(\omega) = -\frac{1}{\pi} P.V. \int_{-\infty}^{\infty} d\omega' \frac{\epsilon'(\omega') - \epsilon(\infty)}{\omega' - \omega}. \tag{A.51}$$

A.4. Laplace equation in spherical and cylindrical coordinates

The Laplace equation for the potential in spherical coordinates [40]

$$\frac{1}{r}\frac{\partial^2}{\partial r^2}(r\Phi) + \frac{1}{r^2\sin\theta}\frac{\partial}{\partial\theta}(\sin\theta\frac{\partial\Phi}{\partial\theta}) + \frac{1}{r^2\sin^2\theta}\frac{\partial^2\Phi}{\partial\phi^2} = 0, \tag{A.52}$$

can be separated [40] into three equations with a product ansatz

$$\Phi = \frac{U(r)}{r}P(\theta)Q(\phi), \tag{A.53}$$

which yields

$$PQ\frac{d^2U}{dr^2} + \frac{UQ}{r^2\sin\theta}\frac{d}{d\theta}(\sin\theta\frac{dP}{d\theta}) + \frac{UP}{r^2\sin^2\theta}\frac{d^2Q}{d\phi^2} = 0. \tag{A.54}$$

Multiplying with

$$r^2\sin^2\theta/UPQ \tag{A.55}$$

leads to

$$r^2\sin^2\theta\left[\frac{1}{U}\frac{d^2U}{dr^2} + \frac{1}{r^2\sin\theta P}\frac{d}{d\theta}\left(\sin\theta\frac{dP}{d\theta}\right)\right] + \frac{1}{Q}\frac{d^2Q}{d\phi^2} = 0. \tag{A.56}$$

Hence we find three separate equations for $Q(\phi)$, $P(\theta)$ and $U(r)$:

$$\frac{1}{Q}\frac{d^2Q}{d\phi^2} = -m^2, \tag{A.57}$$

$$\frac{d^2U}{dr^2} - \frac{l(l+1)}{r^2}U = 0, \tag{A.58}$$

$$\frac{1}{\sin\theta}\frac{d}{d\theta}\left(\sin\theta\frac{dP}{d\theta}\right) + \left[l(l+1) - \frac{m^2}{\sin^2\theta}\right]P = 0. \tag{A.59}$$

Here $(-m^2)$ and $l(l+1)$ are real constants. The solutions are given by

$$Q = e^{\pm im\phi}, \tag{A.60}$$

$$U = Ar^{l+1} + Br^{-l}, \tag{A.61}$$

and

$$P_l(x) = \frac{1}{2^l l!}\frac{d^l}{dx^l}(x^2-1)^l, \tag{A.62}$$

with $x = \cos\theta$. For a problem with azimuthal symmetry

$$m = 0. \tag{A.63}$$

Hence

$$\Phi(r,\theta) = \sum_{l=0}^{\infty}[A_l r^l + B_l r^{-(l+1)}]P_l(\cos\theta). \tag{A.64}$$

The

Laplace equation in cylindrical coordinates [40]

$$\frac{\partial^2\Phi}{\partial\rho^2} + \frac{1}{\rho}\frac{\partial\Phi}{\partial\rho} + \frac{1}{\rho^2}\frac{\partial^2\Phi}{\partial\phi^2} + \frac{\partial^2\Phi}{\partial z^2} = 0, \tag{A.65}$$

can be separated [40] into three ordinary differential equations:

$$\Phi(\rho,\phi,z) = R(\rho)Q(\phi)Z(z), \tag{A.66}$$

$$\frac{d^2Z}{dz^2} - k^2Z = 0, \tag{A.67}$$

$$\frac{d^2Q}{d\phi^2} + \nu^2Q = 0, \tag{A.68}$$

$$\frac{d^2R}{d\rho^2} + \frac{1}{\rho}\frac{dR}{d\rho} + \left(k^2 - \frac{\nu^2}{\rho^2}\right) R = 0. \tag{A.69}$$

The solutions of the first two equations are

$$Z(z) = e^{\pm kz}, \tag{A.70}$$

and

$$Q(\Phi) = e^{\pm i\nu\phi}. \tag{A.71}$$

To find the solution of the last equation

$$\frac{d^2R}{dx^2} + \frac{1}{x}\frac{dR}{dx} + \left(k^2 - \frac{\nu^2}{x^2}\right) R = 0, \tag{A.72}$$

a power series ansatz is used [40]

$$R(x) = x^\alpha \sum_{j=0}^{\infty} a_j x^j. \tag{A.73}$$

We find

$$\alpha = \pm\nu, \tag{A.74}$$

and

$$a_{2j} = -\frac{1}{4j(j+\alpha)} a_{2j-2} \quad \text{for } j = 1, 2, 3, \ldots. \tag{A.75}$$

Hence

$$a_{2j} = \frac{(-1)^j \Gamma(\alpha+1)}{2^{2j} j! \Gamma(j+\alpha+1)} a_0. \tag{A.76}$$

With

$$a_0 = [2^\alpha \Gamma(\alpha+1)]^{-1}, \tag{A.77}$$

where

$$\Gamma(s) = \int_0^\infty e^{-t} t^{s-1} dt, \tag{A.78}$$

the two solutions are the

Bessel functions of the first kind [40]

$$J_\nu(x) = \left(\frac{x}{2}\right)^\nu \sum_0^\infty \frac{(-1)^j}{j!\Gamma(j+\nu+1)} \left(\frac{x}{2}\right)^{2j}, \tag{A.79}$$

$$J_{-\nu}(x) = \left(\frac{x}{2}\right)^{-\nu} \sum_0^\infty \frac{(-1)^j}{j!\Gamma(j-\nu+1)} \left(\frac{x}{2}\right)^{2j}. \tag{A.80}$$

Because

$$J_{-m}(x) = (-1)^m J_m(x), \tag{A.81}$$

for integers [29] the pair of solutions gets replaced by $J_\nu(x)$ and $N_\nu(x)$ where N_ν is called the

Neumann function [40]

$$N_\nu(x) = \frac{J_\nu(x)\cos\nu\pi - J_{-\nu}(x)}{\sin\nu\pi}. \tag{A.82}$$

With this Neumann function it is possible to construct the Bessel-functions of the third kind, the so called

Hankel functions [40]

$$H_\nu^{(1)}(x) = J_\nu(x) + iN_\nu(x), \tag{A.83}$$

$$H_\nu^{(2)}(x) = J_\nu(x) - iN_\nu(x). \tag{A.84}$$

A.5. Sommerfeld integrals

The Sommerfeld identity is found [10] from the scalar wave equation of a point source

$$\left[\frac{\partial^2}{\partial x^2}+\frac{\partial^2}{\partial y^2}+\frac{\partial^2}{\partial z^2}+k_0^2\right]\phi(x,y,z)=-\delta(x)\delta(y)\delta(z), \tag{A.85}$$

with the following solution

$$\phi(r)=\frac{e^{ik_0 r}}{4\pi r}. \tag{A.86}$$

By using its Fourier representation

$$\phi(x,y,z)=\frac{1}{(2\pi)^3}\iiint_{-\infty}^{\infty}dk_x dk_y dk_z\tilde{\phi}(k_x k_y k_z)e^{ik_x x+ik_y y+ik_z z}, \tag{A.87}$$

and also the Fourier transform of the delta function, we get

$$\begin{aligned}\iiint_{-\infty}^{\infty}dk_x dk_y dk_z\left[k_0^2-k_x^2-k_y^2-k_z^2\right]\tilde{\phi}(k_x k_y k_z)e^{ik_x x+ik_y y+ik_z z}=\\ -\iiint_{\infty}^{\infty}dk_x dk_y dk_z e^{ik_x x+ik_y y+ik_z z}.\end{aligned} \tag{A.88}$$

In this way we can identify

$$\tilde{\phi}(k_x k_y k_z)=\frac{-1}{k_0^2-k_x^2-k_y^2-k_z^2}, \tag{A.89}$$

and find

$$\phi(x,y,z)=\frac{-1}{(2\pi)^3}\iint_{-\infty}^{\infty}d\mathbf{k}\frac{e^{ik_x x+ik_y y+ik_z z}}{k_0^2-k_x^2-k_y^2-k_z^2}. \tag{A.90}$$

This integrand has poles at

$$k_z=\pm(k_0^2-k_x^2-k_y^2)^{1/2}. \tag{A.91}$$

By introducing a small loss and using Cauchy's theorem (The integrand vanishes for $\Im m(k_z)\to\infty$) we get

$$\phi(x,y,z)=\frac{i}{2(2\pi)^2}\iint_{-\infty}^{\infty}dk_x dk_y\frac{e^{ik_x x+ik_y y+ik'_z z}}{k'_z}, \tag{A.92}$$

with $k_z' = (k_0^2 - k_x^2 - k_y^2)^{1/2}$ for $z > 0$. Similary for $z < 0$ which leads to

$$\phi(x, y, z) = \frac{i}{2(2\pi)^2} \iint_{-\infty}^{\infty} dk_x dk_y \frac{e^{ik_x x + ik_y y + ik_z'|z|}}{k_z'}, \tag{A.93}$$

and we find the

Weyl identity [10]

$$\frac{e^{ik_0 r}}{r} = \frac{i}{2\pi} \iint_{-\infty}^{\infty} dk_x dk_y \frac{e^{ik_x x + ik_y y + ik_z'|z|}}{k_z}, \tag{A.94}$$

which can be seen as an integral summation of plane waves propagating in all directions, including evanescent waves. By using

$$\mathbf{k}_\rho = \hat{x} k_\rho \cos\alpha + \hat{y} k_\rho \sin\alpha, \tag{A.95}$$

$$\rho = \hat{x}\rho\cos\phi + \hat{y}\rho\sin\phi, \tag{A.96}$$

$$dk_x dk_y = k_\rho dk_\rho d\alpha, \tag{A.97}$$

we find

$$k_x x + k_y y = \mathbf{k}_\rho \cdot \rho = k_\rho \cos(\alpha - \phi), \tag{A.98}$$

$$\frac{e^{ik_0 r}}{r} = \frac{i}{2\pi} \int_0^{\infty} k_\rho dk_\rho \int_0^{2\pi} d k_\alpha \frac{e^{ik_\rho \rho \cos(\alpha-\phi) + ik_z|z|}}{k_z}, \tag{A.99}$$

where

$$k_z = \sqrt{k_0^2 - k_x^2 - k_y^2}. \tag{A.100}$$

Then using the integral identity for Bessel functions

$$J_0(k_\rho \rho) = \frac{1}{2\pi} \int_0^{2\pi} d\alpha e^{ik_\rho \rho \cos(\alpha - \phi)}, \tag{A.101}$$

we finally find the

Sommerfeld identity [10]:

$$\frac{e^{ik_0 r}}{r} = i \int_0^\infty dk_\rho \frac{k_\rho}{k_z} J_0(k_\rho \rho) e^{ik_z z}. \tag{A.102}$$

Its physical interpretation is that a spherical wave can be expanded as an integral summation of cylindrical waves in ρ direction, times a plane wave in z direction over all wave numbers k_ρ. It is also possible to obtain a variation using Hankel functions [10]

$$J_0(k_\rho \rho) = 1/2 \left[H_0^{(1)}(k_\rho \rho) + H_0^{(2)}(k_\rho \rho) \right], \tag{A.103}$$

$$\frac{e^{ik_0 r}}{r} = \frac{i}{2} \int_{-\infty}^\infty dk_\rho \frac{k_\rho}{k_z} H_0^{(1)}(k_\rho \rho) e^{ik_z z}. \tag{A.104}$$

A.6. Free space Green functions

The expression of the free space Green functions depends on the space dimension. One finds [10, 91]

$$G(r) = \frac{e^{ik|\mathbf{r}|}}{|\mathbf{r}|}, \tag{A.105}$$

for three space dimensions

$$G(\rho) = \pi i H_0^1(k|\rho|), \tag{A.106}$$

for two space dimensions, and

$$G(x) = \frac{2\pi i e^{ik|x|}}{k}, \tag{A.107}$$

for one space dimension. The solution of the vector wave equation is given by the dyadic Green function:

$$\mathbf{G} = \left[\mathbb{I} + \frac{1}{k^2}\nabla\nabla\right] G(r). \tag{A.108}$$

A.7. Stationary phase approximation

The method of stationary phase [7, 10] can be used to derive a leading-order approximation of an integral which is highly oscillatory. If the following integral

$$I = \int_{-\infty}^{\infty} dt f(t) g(\lambda, t), \tag{A.109}$$

cannot be integrated in closed form and

$$g(\lambda, t) \sim e^{i\lambda h(t)}, \qquad \lambda \to \infty, \tag{A.110}$$

is rapidly oscillating then by finding a stationary point [10]

$$h'(t_0) = 0, \tag{A.111}$$

at $t = t_0$ where the integrand is least oscillating one can approximate it as

$$I \sim f(t_0) \int_{-\infty}^{\infty} dt g(\lambda, t), \tag{A.112}$$

for $\lambda \to \infty$.

Acknowledgements

First of all, I would like to express my deepest gratitude to my advisor **Ulrich Hohenester** for all his support, guidance and understanding throughout my study and research.

I would also like to thank **Andreas Trügler** and **Robert Schütky** and all my other friends and colleagues at Karl-Franzens-University Graz for their support and encouragement which made my stay and studies in Graz more enjoyable.

Finally, I would like to thank my parents **Heidemarie Waxenegger** and **Günther Waxenegger** and my brother **Günther Waxenegger** for their love and ongoing support during the last years.

Bibliography

[1] J. Aizpurua, T. Taubner, F. J. Garcia de Abajo, M. Brehm, and R. Hillenbrand. Substrate-enhanced infrared near-field spectroscopy. *Optics Express*, 2008.

[2] H. Atwater. The promise of plasmonics. *Sci Am.*, 2007.

[3] H. A. Atwater and A. Polman. Plasmonics for improved photovoltaic devices. *Nature Materials*, 2000.

[4] F. Aussenegg and H. Ditlbacher. Plasmonen als Lichttransporter: Nanooptik. *Physik in unserer Zeit*, 2006.

[5] A. Banos. *Dipole radiation in the presence of a conducting halfspace*. Pergamon Press, 1966.

[6] C. F. Bohren and D. R. Huffman. *Absorption and Scattering of Light by Small Particles*. Wiley, 1998.

[7] M. Born and E. Wolf. *Principles of Optics*. Pergamon Press, 1980.

[8] L. V. Brown, X. Yang, K. Zhao, B. Y. Zheng, P. Nordlander, and N. J. Halas. Fan-Shaped Gold Nanoantennas above Reflective Substrates for Surface-Enhanced Infrared Absorption (SEIRA). *Nano Lett.*, 2015.

[9] W. Cai and T. Yu. Fast Calculations of Dyadic Green's Functions for Electromagnetic Scattering in a Multilayered Medium. *J. Comp. Phys.*, 2000.

[10] W. C. Chew. *Waves and Fields in Inhomogenous Media*. IEEE Press, 1999.

[11] R. Courant. Variational methods for the solution of problems of equilibrium and vibrations. *Bulletin of the American Mathematical Society*, 1943.

[12] B. T. Draine. The discrete-dipole approximation and its application to interstellar graphite grains. *Astrophysical Journal*, 1988.

[13] B. T. Draine and P. J. Flatau. Discrete-dipole approximation for scattering calculations. *J. Opt. Soc. Am*, 1994.

[14] B. T. Draine and J. Goodman. Beyond Clausius-Mossotti - Wave propagation on a polarizable point lattice and the discrete dipole approximation. *Astrophysical Journal*, 1992.

[15] P. Drude. Zur Elektronentheorie der Metalle. *Annalen der Physik*, 1900.

[16] S. Ebihara and W. C. Chew. Calculation of Sommerfeld integrals for modeling vertical dipole array antenna for borehole radar. *IEICE Trams. Electron*, 2003.

[17] R. Esteban, A. Borisov, P. Nordlander, and J. Aizpurua. Bridging quantum and classical plasmonics with a quantum-corrected model. *Nature Comm.*, 2012.

[18] X. Fan, W. Zheng, and D. Singh. Light scattering and surface plasmons on small spherical particles. *Light: Science and Applications*, 2014.

[19] U. Fano. The Theory of Anomalous Diffraction Gratings and of Quasi-Stationary Waves on Metallic Surfaces (Sommerfeld's Waves). *J. Opt. Soc. Am.*, 1941.

[20] Z. H. Firouzeh, G. A. E. Vandenbosch, R. Moini, S. H. H. Sadeghi, and R. Faraji-Dana. Efficient evaluation of green's functions for lossy half-space problems. *Pro. In Elect. Research.*, 2010.

[21] R. Fuchs and S. H. Liu. Sum rule for the polarizability of small particles. *Phys. Rev. B*, 1976.

[22] B. Gallinet and O. J. F. Butlet, J. Martin. Numerical methods for nano photonics: standard problems and future challenges. *Laser Photonics Rev.*, 2015.

[23] R. Gans. Über die Form ultramikroskopischer Goldteilchen. *Annalen der Physik*, 1912.

[24] F. J. Garcia de Abajo. Optical excitations in electron microscopy. *Rev. Modern Phys.*, 2010.

[25] F. J. Garcia de Abajo and A. Howie. Relativistic Electron Energy Loss and Electron-Induced Photon Emission in Inhomogeneous Dielectrics. *Phys. Rev. B*, 1998.

[26] F. J. Garcia de Abajo and A. Howie. Retarded field calculation of electron energy loss in inhomogeneous dielectrics. *Phys. Rev. B*, 2002.

[27] P. Gay-Balmaz and O. J. F. Martin. Electromagnetic scattering of high permittivity particles on a substrate. *Applied Optics*, 2000.

[28] D. J. Griffith. *Introduction to Electrodynamics*. Addison-Wesley, 2012.

[29] S. Hassani. *Mathematical Physics*. Springer, 2002.

[30] A. Hohenau, J. Krenn, S. G. Garcia-Vidal, F. J. amd Rodrigo, L. Martin-Moreno, J. Beermann, and S. Bozhevolnyi. Comparison of finite-difference time-domain simulations and experiments on the optical properties of gold nanoparticle arrays on gold film. *J. Opt. A: Pure Appl. Opt.*, 2007.

[31] U. Hohenester. Simulating electron energy loss spectroscopy with the MNPBEM toolbox. *Comp. Phys. Commun*, 2014.

[32] U. Hohenester. Quantum corrected model for plasmonic nanoparticles: A boundary element method implementation. *Phys. Rev. B*, 2015.

[33] U. Hohenester and J. Krenn. Surface plasmon resonances of single and coupled metallic nanoparticles: A boundary integral method approach. *Phys. Rev. B*, 2005.

[34] U. Hohenester and A. Trügler. Interaction of single molecules with metallic nanoparticles. *IEEE Journal of Selected Topics in Quantum Electronics*, 2008.

[35] U. Hohenester and A. Trügler. MNPBEM - A Matlab toolbox for the simulation of plasmonic nanoparticles. *Comp. Phys. Commun*, 2012.

[36] A. Hörl, A. Trügler, and U. Hohenester. Tomography of particle plasmon fields from electron energy loss spectroscopy. *Phys. Rev. Lett.*, 2013.

[37] A. Hörl, A. Trügler, and U. Hohenester. Full three-dimensional reconstruction of the dyadic Green tensor from electron energy loss spectroscopy of plasmonic nanoparticles. *CS Photonics 2*, 2015.

[38] A. Hrennikoff. Solution of problems of elasticity by the framework method. *Journal of applied mechanics*, 1941.

[39] T. Hutter, F. M. Huang, S. R. Elliott, and S. Mahajan. Near-Field Plasmonics of an Individual Dielectric Nanoparticle above a Metallic Substrate. *J. Phys. Chem. C*, 2013.

[40] J. D. Jackson. *Classical Electrodynamics*. John Wiley Sons, Inc., 1998.

[41] P. B. Johnson and R. W. Christy. Optical Constants of the Noble Metalls. *Phys. Rev. B*, 1972.

[42] O. D. Kellogg. *Foundations of Potential Theory*. Dover Publications, 2010.

[43] A. M. Kern and O. J. F. Martin. Surface integral formulation for 3D simulations of plasmonic and high permittivity nanostructures. *J. opt. Soc. Am.*, 2009.

[44] N. G. Khlebtsov. T-matrix method in plasmonics: An overview. *J. Quant. Spec. and Radiat. Trans.*, 2013.

[45] D. Knebl, A. Hörl, A. Trügler, J. Kern, J. Krenn, P. Puschnig, and U. Hohenester. Gap plasmonics of silver nanocube dimers. *Phys. Rev. B*, 2015.

[46] B. Knoll and F. Keilmann. Enhanced dielectric constrast in scattering-type scanning near-field optical microscopy. *Opt. Commun.*, 2000.

[47] U. Kreibig and M. Vollmer. *Optical Properties of Metal Clusters*. Springer, 1995.

[48] E. Kretschmann and H. Raether. Radiative Decay of Non Radiative Surface Plasmons Excited by Light. *Z. Naturforschung 23a*, 1968.

[49] M. Kuisma, A. Sakko, T. P. Rossi, A. H. Larsen, J. Enkovaara, L. Lehtovaara, and T. T. Rantala. Localized surface plasmon resonance in silver nanoparticles: Atomistic first-principles time-dependent density-functional theory calculations. *Phys. Rev. B*, 2015.

[50] C. B. Lang and N. Pucker. *Mathematische Methoden in der Physik*. Springer, 2005.

[51] L. Lin, R. J. Blaikie, and R. J. Reeves. Surface-Plasmon-Enhanced Optical Transmission through Planar Metal Films. *Progress In Electromagnetics Research Symposium*, 2005.

[52] V. Loke and M. Mengüc. Surface waves and atomic force microscope probe-particle near-field coupling: discrete dipole approximation with surface interaction. *J. Opt. Soc. Am. A*, 2010.

[53] V. Loke, M. Mengüc, and T. A. Nieminen. Discrete-dipole approximation with surface interaction: Computational toolbox for MATLAB. *Journal of Quantitative Spectroscopy and Radiative Transfer*, 2011.

[54] R. J. Lytle and D. L. Lager. Numerical Evaluation of Sommerfeld integrals. *Tech. Rep. UCRL-51688*, 1974.

[55] D. R. Lytle II, P. S. Carney, J. C. Schotland, and E. Wolf. Generalized optical theorem for reflection, transmission, and extinction of power for electromagnetic fields. *Phys. Rev. E*, 2005.

[56] S. A. Maier. Plasmonics: Engineering of highly confined electromagnetic modes. *Converence paper. ECIO 2007*, 2007.

[57] S. A. Maier. *Plasmonics: Fundamentals and Applications*. Springer, 2007.

[58] O. J. F. Martin, A. Dereux, and C. Girard. Iterative scheme for computing exactly the total field propagating in dielectric structures of arbitrary shape. *J. Opt. Soc. Am.*, 1994.

[59] O. J. F. Martin and P. N. P. Electromagnetic scattering in polarizable backgrounds. *Phys. Rev. E*, 1998.

[60] I. D. Mayergoyz. *Plasmon Resonances in Nanoparticles (World Scientific Series in Nanoscience and Nanotechnology)*. World Scientific Publishing Company, 2013.

[61] K. A. Michalski. On the efficient evaluation of integrals arising in the sommerfeld halfspace problem. *IEE Proceedings H - Microwaves, Antennas and Propagation*, 1985.

[62] K. A. Michalski and J. R. Mosig. The Sommerfeld half-space problem revisited: from radio frequencies and Zenneck waves to visible light and Fano mode. *Journal of Electromagnetic Waves and Applications*, 2016.

[63] G. Mie. Beiträge zur Optik trüber Medien, speziell kolloidaler Metalllösungen. *Annalen der Physik*, 1902.

[64] J. R. Mosig and A. A. Melcon. Green's Functions in Lossy Layered Media: Integration Along the Imaginary Axis and Asymptotic Behavior. *IEEE Transactions on Antennas and Propagation*, 2003.

[65] V. Myroshnychenko, J. Rodriguez-Fernandez, I. Pastoriza-Santos, A. E. Funston, C. Novo, P. Mulvaney, L. M. Liz-Marzan, and F. J. Garcia de Abajo. Modelling the optical response of gold nanoparticles. *Chem. Soc. Rev.*, 2008.

[66] B. M. Nebeker, R. Schmehl, G. W. Starr, and E. D. Hirleman. Prediction of light scattering characteristics of particles and structures on surfaces by the coupled-dipole method. *Proceedings of SPIE*, 1996.

[67] C. Noguez. Surface Plasmons on Metal Nanoparticles: The Influence of Shape and Physical Environment. *J. Phys. Chem. C*, 2007.

[68] L. Novotny. The History of Near-field Optics. 2007.

[69] L. Novotny and B. Hecht. *Principles of Nano-Optics*. Cambridge University Press, 2006.

[70] E. Ozbay. Plasmonics: Merging Photonics and Electronics at Nanoscale Dimensions. *Science*, 2006.

[71] M. Paulus, P. Gay-Balmaz, and O. J. F. Martin. Accurate and efficient computation of the Green's tensor for stratified media. *Phys. Rev. E.*, 2000.

[72] M. Pelton and G. W. Bryant. *Introduction to Metal-Nanoparticle Plasmonics*. Wiley, 2013.

[73] A. Pinchuk, A. Hilger, G. von Plessen, and U. Kreibig. Substrate effect on the optical response of silver nano particles. *Nanotechnology*, 2004.

[74] E. M. Purcell and C. R. Pennypacker. Scattering and Absorption of Light by Nonspherical Dielectric Grains. *Astrophysical Journal*, 1973.

[75] Q. Qiao, C.-X. Shan, J. Zheng, B.-H. Li, Z.-Z. Zhang, L.-G. Zhang, and D.-Z. Shen. Localized surface plasmon enhanced light-emitting devices. *J. Mater. Chem.*, 2012.

[76] H. Raether. *Surface Plasmons on Smooth and Rough Surfaces and on Gratings*. Springer, 1988.

[77] J. N. Reddy. *An Introduction to the Finite Element Method*. McGraw-Hill, 2006.

[78] R. H. Ritchie. Plasma Losses by Fast Electrons in Thin Films. *Phys. Rev.*, 1957.

[79] R. H. Ritchie, E. T. Arakawa, J. J. Cowan, and R. N. Hamm. Surface-Plasmon Resonance Effect in Grating Diffraction. *Phys. Rev.*, 1968.

[80] R. Schmehl, E. D. Hirleman, and S. Wittig. The Coupled-Dipole Method for Light Scattering from Particles on Plane Surfaces. *Conference Paper*, 1996.

[81] R. Schmehl, B. M. Nebeker, and E. D. Hirleman. Discrete-dipole approximation for scattering by features on surfaces by means of a two-dimensional fast Fourier transform technique. *J. of Opt. Soc. Am A*, 1997.

[82] K. Schraml, M. Spiegl, M. Kammerlochner, G. Brachner, J. Bartl, T. Campbell, J. J. Finley, and M. Kaniber. Optical properties and interparticle coupling of plasmonic bowtie nanoantennas on a semiconducting substrate. *Phys. Rev. B*, 2014.

[83] T. V. Shahbazyam and M. I. Stockman. *Plasmonics: Theory and Applications*. Challenges and Advances in Computational Chemistry and Physics, 2014.

[84] A. Sommerfeld. Über die Fortpflanzung elektrodynamischer Wellen längs eines Drahtes. *Annalen der Physik und Chemie*, 1899.

[85] K. Stannigel, M. König, J. Niegemann, and K. Bosch. Discontinuous Galerkin time-domain computations of metallic nanostructures. *Optical Society of America*, 2009.

[86] A. Trügler. *Optical Properties of Metallic Nanoparticles: Basic Principles and Simulation*. Springer, 2016.

[87] J. K. E. Tunaley. A Summary of EM Theory for Dipole Fields near a Conducting Half-Space. *LRDC*, 2012.

[88] M. Valamanesh, Y. Borensztein, C. Langlois, and E. Lacaze. Substrate Effect on the Plasmon Resonance of Supported Flat Silver Nanoparticles. *J. Phys. Chem. C*, 2011.

[89] H. C. van de Hulst. *Light Scattering by Small Particles*. Dover Publications, 1981.

[90] A. J. Ward and J. B. Pendry. A program for calculating photonic band structures, Green's functions and transmission/reflection coefficients using a non-orthogonal FDTD method. *Computer Physics Communications*, 2000.

[91] K. Watanabe. *Integral Transform Techniques for Green's Function*. Springer, 2014.

[92] J. Waxenegger. Imaging excitons in carbon nanotubes using plasmonic nanoparticles, 2010.

[93] J. Waxenegger, A. Trügler, and U. Hohenester. Plasmonics simulations with the MNPBEM toolbox: Consideration of substrates and layer structures. *Comp. Phys. Commun*, 2015.

[94] R. W. Wood. On a remarkable case of uneven distribution of light in a diffraction grating spectrum. *Proc. Phys. Soc.*, 1902.

[95] L. C. Wrobel . *The Boundary Element Method*. Wiley, 2002.

[96] Y. Wu and P. Nordlander. Finite-Difference Time-Domain Modeling of the Optical Properties of Nanoparticles near Dielectric Substrates. *J. Phys, Chem. C*, 2010.

[97] H.-Y. Xie, M. Chen, Y.-C. Chang, and R. S. Moirangthem. Efficient simulation for Light Scattering from Plasmonic Core-Shell Nanospheres on a Substrate for Biosensing. *Plasmonics*, 2015.

[98] Z. L. Yang, Q. H. Li, F. X. Ruan, Z. P. Li, B. Ren, h. X. Xu, and Z. Q. Tian. FDTD for plasmonics: Applications in enhanced Raman spectroscopy. *Chin. Sci. Bull.*, 2010.

[99] W. Yanpeng and P. Nordlander. Finite-Difference Time-Domain Modeling of the Optical Properties of Nanoparticles near Dielectric Substrates . *Phys. Chem. C*, 2010.

[100] K. S. Yee. Numerical solution of initial boundary value problems involving Maxwell's equations in isotropic media. *IEEE Transactions on Antennas and Propagation*, 1966.

[101] J. Zenneck. Über die Fortpflanzung ebener elektromagnetischer Wellen längs einer ebenen Leiterfläche und ihre Beziehung zur drahtlosen Telegraphie. *Annalen der Physik*, 1907.

[102] P. Zhang, J. Feist, A. Rubio, P. Garcia-Gonzales, and F. J. Garcia-Vidal. Ab initio nanoplasmonics: The impact of atomic structure. *Phys. Rev. B*, 2014.

[103] S. Zhang, K. Bao, N. J. Halas, H. Xu, and P. Nordlander. Substrate-Induced Fano Resonances of a Plasmonic Nanocube: A Route to Increased-Sensitivity Localized Surface Plasmon Resonance Sensors Revealed. *Nano Lett.*, 2011.

[104] R. Zsigmondy and H. Siedentopf. Über Sichtbarmachung und Größenbestimmung ultramikoskopischer Teilchen, mit besonderer Anwendung auf Goldrubingläser. *Annalen der Physik*, 1903.